The Effects of Quantum Dot Surface Chemistry on Fluorescence and Additive Manufacturing Applications

By

Talitha Marie VanWie

Dissertation

Submitted to the Faculty of the

Graduate School of Vanderbilt University

in partial fulfillment of the requirements

for the degree of

DOCTOR OF PHILOSOPHY

in

Chemistry

December 14, 2019

Nashville, Tennessee

Approved:

Sandra J. Rosenthal, Ph. D.

Timothy P. Hanusa, Ph. D.

Lauren E. Buchanan, Ph. D.

Douglas E. Adams, Ph. D.

Copyright © 2019 by Talitha Marie VanWie
All Rights Reserved

Dedicated

to

David, my wonderful and supportive husband

ACKNOWLEDGEMENTS

There are many people I would like to thank for their help and support through my years of graduate school. First, I would like to thank my advisor, Dr. Sandra J. Rosenthal, and everything she has done for me. You gave me the opportunity to work in your lab and grow as a scientist. The freedom and independence you provide to pursue results has given me the knowledge of responsibility and problem solving.

I must thank my committee members, past and present: Dr. Timothy Hanusa, Dr. Lauren Buchannan, Dr. Douglas Adams, and Dr. Eva Harth. Your guidance and questions, and feedback during my exams and committee meetings have been invaluable to my research.

Dr. James McBride, so much thanks needs to go your way. You were always available if I had questions about my research, and how to start answering those questions myself. Your advice, input, and editing on my articles has taught me so much about writing that I will use for years to come. I also would like to thank you for your time and effort you spent at the electron microscope, obtaining images of my difficult samples.

I would like to thank Dr. Sharon Weiss for the use of her lab and integrating sphere; Dr. Dmitry Koktysh, for training on instrumentation in the VINSE facilities; Mr. Andrzej Balinski, for your help in using the Chemistry instrumentation lab; Mr. David Koester, Mr. Garrett Thone, and Mr. Rich Teising, for your help with fabrication of materials and instrumentation training at LaSIR and the engineering lab.

Dr. Noah Orfield, thank you for mentoring me during my rotation in the Rosenthal lab and teaching me how to successfully produce the ultrasmall CdSe quantum dots. Also, thank you for not laughing too hard at me the time I smacked my face on the hood sash. You made it a joy

to join the lab and were a fun desk mate. To both you and Dan Sprague, thanks for the fun times playing softball, going to trivia, and talking baseball. I would also like to thank Nathanial Freymeyer for his time spent editing my writing and having people assume every time we are talking it is about baseball. To the rest of the Rosenthal lab, Louie, Oleg, Cara, Sophie, and Ian, you have made the lab a great environment to work in, due to your unique personalities. I have made many life-long friends.

To my collaborator and friend, Dr. Cole Brubaker, thank you for sharing a lot of good times, as well as the bad. When research didn't work, I'm glad I had you at my side to come up with new crazy ideas. Even though you are not a chemist, I am not an engineer, and our projects wouldn't have moved forward without the both of us. Thanks for introducing me to the wonders of a 3D-printer and all the capabilities it has.

I want to acknowledge Vanderbilt University and the Office of Naval Research under the Multidisciplinary University Research Initiative on "Sound and Electromagnetic Interacting Waves" (Grant No. N00014-10-1-0958) for financial support during my tenure as a graduate student. Without said funding none of this would have been possible.

To my family, especially my parents Mary and Allan Frecker, thank you for supporting me as I followed my dreams. You always taught me that I can accomplish what I strive for. I will always be grateful for your love and support. To my siblings and in-laws – Vincent, Kaiti, Veronica, Joe, Dale, Taylor, and Ben, I don't know how many days would have been bleaker if it wasn't for our fun conversations and pictures sent. I know if I ever need a laugh to brighten my day, I can go to you. To my niece, Adelaide, and nephews, Jasper, Teddy, and Atticus, watching you grow up and learn is such a joy. Your curiosity is inspirational.

To my best friend Jordan, I can never express how much your friendship has helped me through my graduate career. You were always available for a laugh, a cry, or a good rant. I always looked forward to the times you could come visit and we could enjoy the country music of Music City.

Finally, David, my husband, you are the most amazing, supportive, and strongest man I know. I will be forever grateful to have you with me. Thank you for your love and support through these years, uprooting your life to follow me down to Nashville. There will never be enough words to express how much you mean to me. I love you.

TABLE OF CONTENTS

Page

DEDICATION iii

ACKNOWLEDGEMENTS iv

LIST OF TABLES vi

LIST OF FIGURES vii

Chapter

I. Introduction 1

1.1 Today's Energy Problem 1
1.2 Quantum Dots 9
1.3 Scope of this work 13

II. Experimental 15

2.1 Introduction 15
2.2 Quantum Dot Synthesis 15
2.2.1 Ultrasmall CdSe Synthesis 15
2.2.2 Graded Alloy CdSSe Synthesis 17
2.3 Quantum Dot Ligand Exchange 18
2.3.1 CdSe Formic Acid Ligand Exchange 19
2.3.2 CdSe Citric Acid Ligand Exchange 19
2.4 Quantum Dot Encapsulation 20
2.4.1 Encapsulation with BP-PFCB 20
2.4.2 Encapsulation with Epoxy 21
2.4.3 Encapsulation with Polylactic Acid 22
2.5 Encapsulated Quantum Dots Characterization 23
2.5.1 Compression Testing 23
2.5.2 Tensile Testing 24
2.5.3 Thin Film Optical Characterization 26
2.5.4 Transmission Electron Microscopy 27
2.5.5 Thermal Characterization 27
2.5.6 Mechanical Testing 28

III. Formic and Citric Acid Capped Quantum Dots 29

3.1 Introduction 29
3.2 Results and Discussion 32

3.2.1 Quantum Yield Effects 32
3.2.2 Spectroscopy Analysis 41
3.2.3 BP-PFCB Films 45
3.3 Conclusions 49

IV. In Situ Material State Monitoring Using Embedded CdSe Quantum Dots 52

4.1 Introduction 52
4.2 Results and Discussion 54
4.2.1 Cylindrical and Thin Disc Epoxy Loading Studies 54
4.2.2 Surface Coated Epoxy Loading Studies 61
4.3 Conclusions 68

V. Incorporation of CdSSe Quantum Dots for 3D Printing and Additive Manufacturing Applications 70

5.1 Introduction 70
5.2 Results and Discussion 73
5.2.1 Thin Film Characterization 73
5.2.2 Thermal Property Characterization of Quantum Dots in Polylactic Acid 82
5.2.3 Mechanical Property Analysis of Quantum Dots Embedded in Polylactic Acid Dogbones 87
5.2.4 3D Printed Quantum Dot Light Devices 91
5.3 Conclusions 93

VI. Conclusion and Future Outlook 95

6.1 Overall Conclusions 95
6.2 Future Directions 97

Appendix

A. Quantum Yield Calculations 99

B. CIE Coordinates and Calculations 101

REFERENCES 103

LIST OF TABLES

Table Page

3.1 Quantum Dot Infrared Spectroscopy Peaks Assignments 43

5.1 Lifetime Analysis of 3D-Printed PLA/CdSSe Quantum Dot Thin Films.....81

5.2 Differential Scanning Calorimetry Results of 3D-Printed PLA/CdSSe Quantum Dot Samples 85

5.3 Mechanical Properties of 3D-Printed PLA/CdSSe Quantum Dot Tensile Test Specimens 89

LIST OF FIGURES

Figure Page

1.1 Types of Lighting Throughout History....5

1.2 Color Characteristics: Luminous Efficiency Function, CIE, and CRI....7

1.3 Optical Characteristics of Traditional Sized Quantum Dots....11

1.4 Optical Characteristics of Ultrasmall CdSe Quantum Dots....13

2.1 Setup for Quantum Dot Synthesis....16

2.2 Epoxy/CdSe Compression Samples....21

2.3 Epoxy/CdSe Surface Coated Tensile Samples....22

2.4 PLA Nanofunctionalized Filament Fabrication....23

2.5 Compressive Testing Setup....24

2.6 Tensile Testing Setup....25

2.7 Thin Film Sample Holders....26

2.8 ASTM D638 Type V Tensile Test Specimen Diagram....28

3.1 Optical Characteristics of Ultrasmall CdSe Quantum Dots....30

3.2 Optical Characteristics of Formic Acid Treated CdSe Quantum Dots....33

3.3 Optical Characteristics of Citric Acid Treated CdSe Quantum Dots....34

3.4 TEM and STEM of Ultrasmall CdSe and Citric Acid Treated CdSe Quantum Dots....36

3.5 Emission Mechanism for CdSe and Citric Acid Treated CdSe Quantum Dots....39

3.6 Comparison of Formic Acid Treated and Citric Acid Treated CdSe Quantum Dots in Solution After 25 Days....40

3.7 Citric Acid Treated CdSe Quantum Dot Photoluminescence Spectra After 21 Days....41

3.8 Formic Acid Treated CdSe Quantum Dot Infrared Spectra....42

3.9 Citric Acid Treated CdSe Quantum Dot Infrared Spectra 43

3.10 CdSe Quantum Dot ^{1}H NMR Spectrum 44

3.11 Citric Acid Treated CdSe Quantum Dot ^{1}H NMR Spectrum 45

3.12 Optical Characteristics of BP-PFCB/CdSe-FA Quantum Dot Films 46

3.13 Intensity Versus Percent Weight Loading of BP-PFCB/CdSe-FA Quantum Dot Films 47

3.14 Fluorescence Microscopy of BP-PFCB/CdSe-FA Quantum Dot Films 49

4.1 Proposed Approach for Damage Detection Using CdSe Quantum Dots 53

4.2 Epoxy/CdSe Quantum Dot Cylinders 54

4.3 Schematic Illustration of Integrating Sphere System 55

4.4 Photoluminescence Response of Loaded Epoxy/CdSe Quantum Dot Cylinders 56

4.5 Unloaded Versus Loaded Epoxy/CdSe Cylinders 56

4.6 Schematic Representation of Laser Excitation of the Epoxy/CdSe Quantum Dot Cylinders 57

4.7 Photoluminescence Response of Loaded Epoxy/CdSe Quantum Dot Thin Discs 59

4.8 Integral Emission Curve for Epoxy/CdSe Quantum Dot Thin Disc Samples 60

4.9 Epoxy/CdSe Surface Coated Tensile Samples 61

4.10 Photoluminescence Response of Loaded Epoxy/CdSe Surface Coated Aluminum Tensile Samples 62

4.11 Integral Emission Curve for Epoxy/CdSe Quantum Dot Surface Coated Aluminum Tensile Samples 63

4.12 Photoluminescence Response of Loaded Epoxy/CdSe Surface Coated Fiberglass Tensile Samples 64

4.13 Integral Emission Curve for Epoxy/CdSe Quantum Dot Surface Coated Fiberglass Tensile Samples 65

4.14 Temporal Photoluminescence Response of Epoxy/CdSe Quantum Dot Surface Coated Aluminum Tensile Samples 67

4.15 Temporal Photoluminescence Response of Epoxy/CdSe Quantum Dot Surface Coated Fiberglass Tensile Samples.....67

5.1 TEM of PLA/CdSSe Quantum Dot 3D-Printed Films 74

5.2 Optical Characteristics of PLA/CdSSe Quantum Dot 3D-Printed Thin Films.....77

5.3 FWHM Analysis of Photoluminescence Spectra for PLA/CdSSe 3D-Printed Thin Films.....79

5.4 Lifetime Analysis of PLA/CdSSe Quantum Dot 3D-Printed Thin Films.....80

5.5 Thermogravimetric Analysis Response of PLA/CdSSe Quantum Dot 3D-Pinted Thin Films.....82

5.6 Differential Scanning Calorimetry Curves for PLA/CdSSe Quantum Dot 3D-Pinted Thin Films 84

5.7 PLA/CdSSe Quantum Dot 3D-Printed ASTM D638 Type V Tensile Dogbone Specimens 87

5.8 Tensile Load Response of PLA/CdSSe Quantum Dot 3D-Printed Dogbone Specimens.....88

5.9 PLA/CdSSe Quantum Dot 3D-Printed Light Devices.....93

B.1 Color Matching Functions.....101

CHAPTER I

INTRODUCTION

1.1 Today's Energy Problem

For centuries, energy in some form has been at the center of human lives. Humans have always needed energy for light, heat, manufacturing, and transportation. These requirements for energy have been key to many events in the political, economic, and environmental history of the entire world. Many civilizations and cultures have risen and fallen over the availability and development of energy resources, making energy an enduring and global currency. Carbon-based resources have been at the core of energy sources since the beginning of time, with humans creating fire by burning wood. As wood became scarce in certain areas of Europe, there was an increase in mining coal, a more energy dense source. This need for a new energy source led to the development of the steam engine and spurred the Industrial Revolution. The necessity for the next energy transition is evident as current energy sources are unsustainable.

Fossil fuels have dominated the United States' energy production and consumption for over 100 years, with the mix changing over time. Petroleum, natural gas, and coal account for 80% of the United States' energy production in 2018.[1] Worry of the possibility of fossil fuels running out can be traced back as far as 1860.[2] The exact availability of these resources is uncertain, not just the physical quantities, but also the conditions under which they can be extracted.[3,4] Instability in the Persian Gulf, Venezuela, and Nigeria, areas where oil is prominent, make this resource availability fragile. Natural gas has been known to be difficult to transport

and is prone to shortages.[5] The United States, which holds about one-fourth of the world's known coal reserves, reportedly had 27% of electricity produced from coal in 2018.[1,6]

Although coal is the least expensive fossil fuel commodity for its energy content, its use is projected to decrease over the next 25 years, due to competing energy sources and the fact that burning coal is a major source of carbon dioxide (CO_2) emissions. In 2018, CO_2 levels exceeded 407 ppm for the first time in recorded history.[7] If fossil fuels continue to be burnt at the current rate, CO_2 levels are projected to rise to 1500 ppm. In 2019, the U.S. Environmental Protection Agency (EPA) issued the Affordable Clean Energy Rule (ACE), which establishes emissions guidelines for states to limit CO_2 at coal-fired power plants.[8] It is estimated that ACE would reduce CO_2 emissions from coal-fired power plants by 11 million short tons by 2030. Even with the projected decline in emissions from coal-fired power plants, focus is shifting to electricity generation coming from natural gas and renewables. Without this shift, we could see many political, economic, social, and ethical consequences due to a global environmental change.

With increases in population in developing economies, the global electricity demand has increased by 3% a year since 2000, reaching 22,200 terawatt-hours (TWh) in 2017.[9] Since 2000, the demand for electricity has increased at more than two and a half times the rate of population growth. This increase in demand is due to policies implemented in Southeast Asia and India, such as investment in electricity production, networks and storage of $750 billion, as of 2017, making electricity more available to more people. With the rapid demand and development of electricity in countries such as India, there was a global investment in electricity production, networks and storage of $750 billion, as of 2017. Historically, coal has been the largest source of electricity, with large centralized power plants that transmit power over long distances to demand centers. With significant progress in research in the areas of harvesting renewable energy

sources, such as wind, water, and solar, the nature of electricity supply is being redefined. From 2000 to 2017, the market for wind power projects increased nine-fold, while the solar photovoltaic market increased aggressively. Worldwide, solar PV and wind now deliver 6% of electricity generation, as compared to only 0.2% in 2000. With affordable solar and wind power options, consumers can take a more active role in meeting their own energy needs, including providing affordable access to electricity for the nearly 1 billion people without it in under-developed countries.

In advanced economies, such as the United States, a plateau or a decrease in electricity demand has been observed in recent years.[1,9] A number of factors have led to this slow in growth in electricity demand, with the pivotal reason being energy efficiency. In 2017, it was reported that energy efficiency methods that were adopted by 2000 have saved approximately 1,800 TWh, which is about 20% of the overall electricity use. In 2018, the International Energy Agency (IEA) published the *World Energy Outlook*, in which they produced an Efficient World Scenario that quantified the "implications for global energy use of pursuing all economically viable opportunities to improve energy efficiency".[9] One of the major impacts on energy consumption in end-use sectors proposed with this report is in lighting.

Before 400,000 BC, the only source of light humans had was the sun during the day, and to a lesser extent, the moon at night. It wasn't until Homo erectus discovered fire, probably from a bolt of lightning striking a tree, that man first used an "artificial" light source.[10,11] This was the first instance of burning fuels for light, which would last up through the mid-1800's, with burning animal fat, oil, gas, and kerosene (Figure 1.1). Although tallow candles were primitive devices, they were very costly during their use in the 14th through 18th centuries, around $1300 per barrel of oil equivalent, making them unavailable for most people.[12] It wasn't until the early

1800s, with the introduction of town gas, which was produced from coal, that lighting was cheaper and more available to the common man. This higher availability of light was due to gas lamps being twice as efficient as tallow candles, which only produced 13 lumens. In 1802, the first light bulb was created by passing a current through a platinum strip, creating the first carbon arc lamp.[10,13] The lamps were not practical for commercial development because they burned too brightly, consumed a large amount of current, and quickly drained the battery. It wasn't until the late 1800s that the incandescent bulb was created. As with the previous forms of lighting, the light produced was a by-product of heat generation. This was the main reason for the low efficiency of these early light sources. After the 1930s, the efficiency of the incandescent bulb changed very little, with an efficiency of only ~5%.[14] Lighting efficiency was dramatically increased in the 1990s with the improvements of the compact fluorescent light (CFL), being five-times more efficient than the incandescent bulb. Although the early CFL was more efficient, many consumers veered away from these bulbs due to their high cost, bulky size, and inconsistent performance.[13] Although CFLs were the most efficient and longest lasting bulb of the time (8,000 hours vs 1,000 hours for incandescent bulbs), many people were still hesitant to use them because of the mercury content and the complications that arise with their disposal. The use of CFLs increased after the passing of the Energy Independence and Security Act of 2007, which banned the sale and manufacture of energy-inefficient common household incandescent bulbs.[15] By 2001, approximately 22% of electricity consumption in the United States went to producing light, which was about 8% of the total energy usage, costing the United States consumer approximately $50 billion per year.[16,17] To reduce the cost of electricity and diminish the 130 million tons of carbon that was emitted to produce this electricity, an even more efficient light source needed to be discovered.

Figure 1.1 Types of lighting throughout history. It wasn't until solid state lighting (LEDs) that light was no longer a by-product of a reaction, which resulted in low efficiencies. From left to right the light sources are: (top row) the sun, fire, a candle, oil lamp, gas lamp, (bottom row) incandescent bulb, fluorescent bulb, halogen bulb, compact fluorescent lamp (CFL), and light emitting diodes (LEDs).

Solid state light (SSL), specifically light emitting diodes (LEDs) are the revolutionary light source the electric lighting market needs to save energy and improve lighting quality, performance and service. In 1962, the first visible spectrum LED was invented, emitting red light, with pale yellow and green to follow.[13] LEDs use a semiconductor to directly convert electricity into light. These devices are small in area and emit light in a specific direction, decreasing the need for diffuser and reflectors, which can trap light. Although improvements to the colored devices continued into the 1990s, it wasn't until the development of the first bright blue LED in 1993 that the possibility of producing a bright white light LED was realized.[18] The United States Department of Energy (DOE) established the Next Generation Lighting Initiative

in 2005 as part of the Energy Policy Act to help accelerate the development of white-light markets by allocating $350 million in funding between 2007 and 2013.[19] Because of the direct conversion of electricity to light in SSL devices, if a 50% efficient technology existed, it could reduce energy consumption in the United States by about 620 billion kWh per year. This higher efficiency trend has been seen between 2001 and 2015, with the average system efficacy of installed lighting increasing from 36 lm/W to 51 lm/W.[14] By 2050, it is expected that the purchased electricity for light will be 51% lower than in 2018.[1]

Although LEDs are more efficient and longer lasting than incandescent bulbs and CFLs, they are often inadequate when it comes to light quality.[20,21] Currently, commercial white-light emitting LEDs are fabricated via two methods. The first method used the bright blue LED discovered in 1993 coupled with a phosphor. White light is produced when the phosphor absorbs a portion of the higher energy light and emits a balancing color. Even though this is a single, compact, white-light source, the phosphors required are composed of rare earth elements, and the devices have a low color quality and a halo effect due to scattering within the phosphor. The second method consists of mixing monochromatic LEDs in suitable proportions. With this method it is difficult to mix the lights and maintain the color stability over the life of the device as different color LEDs operate at different conditions, causing one or more to degrade before others. As of 2017, commercial phosphor converted white LEDs have reached about 160 lm/W for warm white and 180 lm/W for cool white devices. These correspond to electrical-optical power conversion efficiencies of approximately 50%.[22] While these devices have reached the goal laid out by the DOE roadmap, they still lack in color quality.

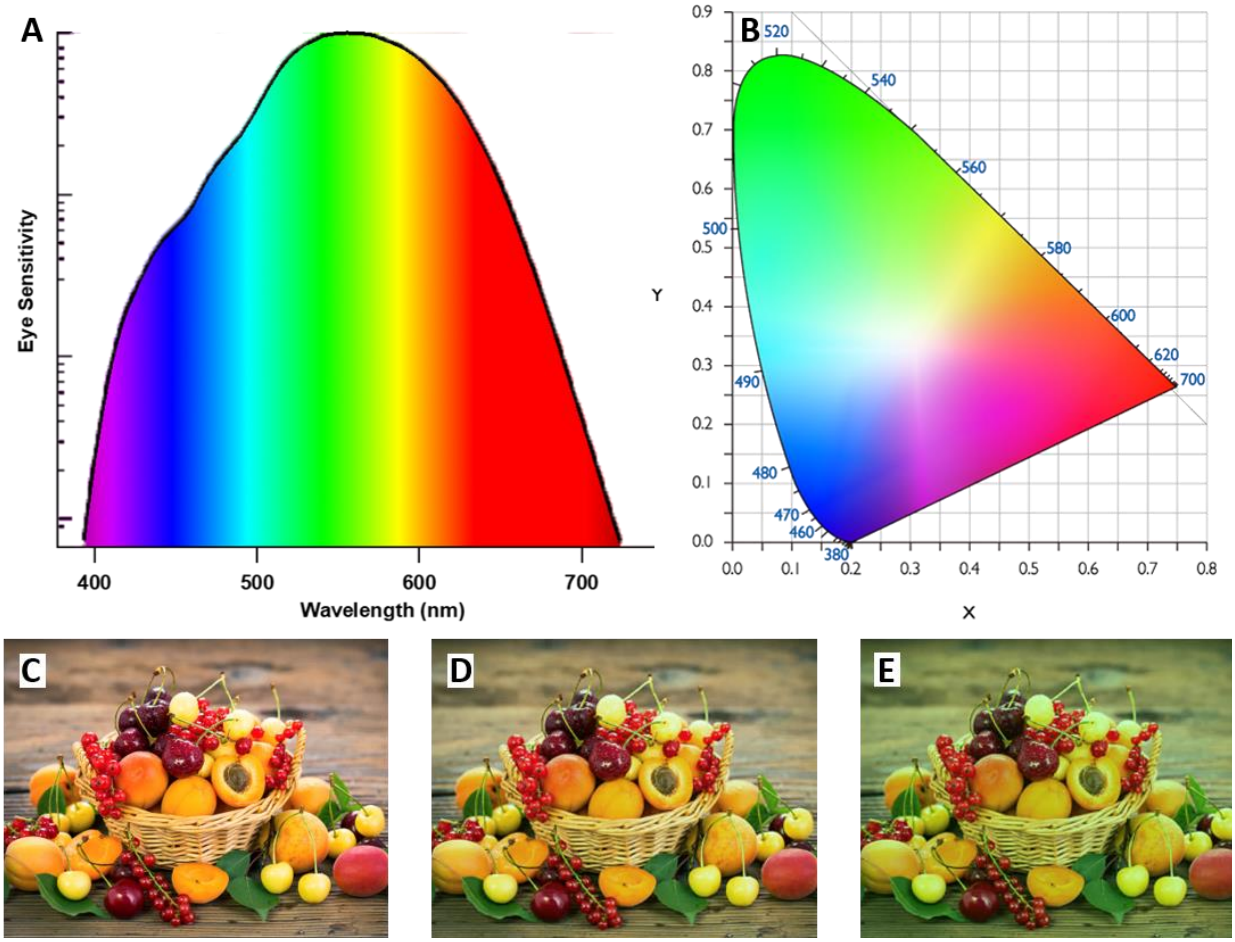

Figure 1.2 A) Sharpe, Stockman, Jagla, and Jägle luminous efficiency function for the human eye's sensitivity. B) The 1931 CIE chromaticity plot with pure white at (0.333, 0.333). C) Photograph of fruit taken under lighting with a CRI value of >90, D) 80, and E) 60. (Images from C-E) Selected-Lights)

The human eye is particularly selective when it comes to differentiating colors; it is estimated that humans can distinguish up to 10 million colors. The eye is sensitive to visible light (400-700 nm) on the electromagnetic spectrum, with a distinct peak at 555 nm.[16,23,24] When the eye perceives white light, it is a balanced combination of wavelengths over the visible region. A standard measure of how the eye will interpret the color of a light source has been established by the International Lighting Commission (Commission Internationale de l'Eclariage) and been in practice for nearly a century with minor changes.[25] Since the human eye has three cone photoreceptors, light can be precisely matched in appearance with the combination of three different colored lights called primaries. These tristimulus values can be converted to *x* and *y* values and graphed on the plot shown in Figure 1.3. Pure white light is represented with the CIE coordinates of (0.333, 0.333). The chromaticity diagram offers a method to comparing the colors of different sources, but for a white light source, the sun is the evident illuminant to compare to, as it is a blackbody radiator.

For a blackbody radiator, the emission spectrum is a function of its temperature, so white light can be characterized by finding the temperature of the blackbody radiator whose color is closest to the white light source. This temperature is called the correlated color temperature (CCT), where the sun is close to 6000 K and a high CCT is associated with a cool white shade. It is more desirable to have a warmer white shade (between 3000 K and 4500 K) for indoor lighting to avoid the disrupting effects cool white light has on the human biological clock. In general lighting, an optimal white light source would allow us to perceive the real colors of objects as accurately as possible. The most commonly used color rendition metric is the color rendering index (CRI), which was introduced by CIE in 1971, and assumes that the reference white light, which is a blackbody radiator, renders the colors of objects perfectly. To successfully

render the real colors of objects, a light source should have a CRI greater than 90. A full discussion of how to calculate CIE coordinates of a light source is contained within Appendix A.

The DOE declared that for general illumination, LEDs must have a luminous efficiency of at least 200 lm/W, white CIE coordinates (0.333, 0.333), and a CRI greater than 80.[16] As previously mentioned, current commercial LEDs have reached 180 lm/W. The multi-LED devices and the phosphor converted LEDs described earlier still suffer in color rendering. The multi-LED devices, which are based on narrow emitters, do not provide a broad enough white light for colors to be perceived as real. While it is still important to improve upon current technologies, new materials must be researched to find the solution to a high efficiency, quality white light.

In addition to producing more energy efficient light sources to cut down on the cost of energy and the amount of CO_2 emissions created while generating electricity, energy infrastructure needs to undergo increased investment to ensure long-term sustainability and capacity. Currently in the United States, electricity delivery depends on a complex and aging system of power generation, transmission, and distribution. It is estimated that $177 billion in investments is needed by 2025 to facilitate upgrade costs and replace older infrastructure with new renewable energy facilities. The development of new structural health monitoring (SHM) technologies could facilitate engineers to design the next generation of structure which are able to identify, communicate, and automatically repair damage.

1.2 Quantum Dots

The application of nanotechnology was in use centuries before the field was formally defined, with the study of colloids and gold sols. Nanomaterials (from the Greek word “nanos,” meaning dwarf) have at least one dimension measuring in the range of 1-100 nm. Nanomaterials

bridge the gap between molecular and bulk levels, resulting in unique properties.[26] Semiconductor nanomaterials, in particular, demonstrate distinctive optical and electronic when below the bulk size.[27] Bulk semiconductors have continuous energy bands with a composition-dependent band gap energy (E_g), which is the minimum energy required to excite an electron from the valence energy band in the vacant conduction energy band. The excitation of an electron leaves a positively charged hole in the valence band. The positively charged hole and the negatively charged electron are in the lowest energy state when they are in an electrostatically bound pair called an exciton. Since the hole has a larger effective mass than the electron and the opposite charge, the exciton will exist in a semi-stable state where the electron orbits around the hole at a specific radius, which is known as the Bohr exciton diameter.[28] If the size of a semiconductor nanocrystal is smaller than the size of the exciton, the electron-hole pair becomes confined in space, increasing their energy. When a semiconducting nanoparticle reaches this quantum confinement regime the particles are referred as quantum dots.[29] At this point, discrete electronic states arise from the continuum of levels in the valence and conduction bands, and the optical and electronic properties are dependent on the quantum dot size. L.E. Brus developed a model for this behavior with his solution to the Schrödinger equation, demonstrating that as the size of the quantum dot increases, the absorption energy decreases.[27–30]

Cadmium selenide (CdSe) quantum dots are one of the most studied materials of quantum dots.[31–33] CdSe has a Bohr exciton diameter of 11.2 nm and the bulk band gap is 1.75 eV, so nanocrystals less than about 10 nm will exhibit strong quantum confinement.[30,34,35] The energy required to excite an electron to from the valence band to the conduction band increases as the quantum dot diameter decreases from 10 nm, due to the band gap being inversely proportional to the diameter. The energy of a photon is also inversely proportional to the

wavelength of a photon, so as the diameter of the quantum dots is decreased, the energy required to excite an electron into the conduction band will increase, or blue-shift. Since the bulk band gap of CdSe is 1.75 eV, which corresponds to a wavelength of 710 nm, the wavelength to excite smaller quantum dots will fall in the visible range. So, by controlling the size of CdSe quantum dots, the light that the quantum dots can absorb and monochromatically emit can be tuned.

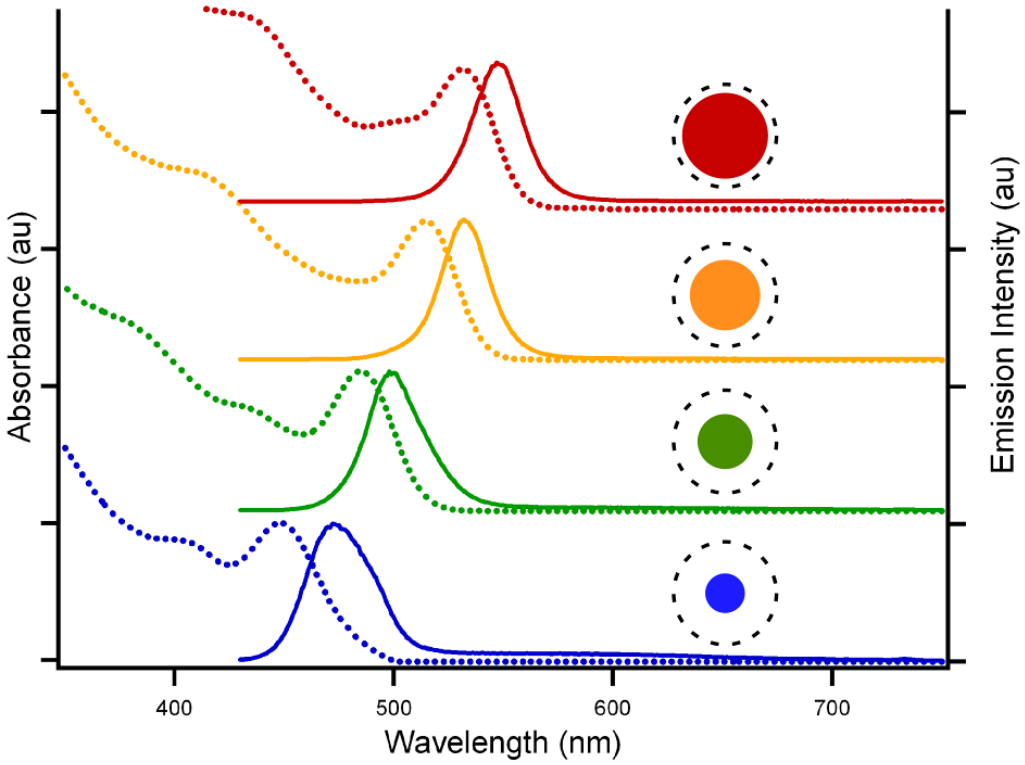

Figure 1.3 The absorption spectra (dotted lines) and emission spectra (solid lines) of various sizes of quantum dots. The images of the quantum dots beside the spectra show how the emission color changes with the size of the quantum dot. As the size gets smaller, the emission blue-shifts. The black dashed line surrounding the quantum dot represents the bulk Bohr exciton diameter.

The power to tune a single material's optical properties by size, with the additional advantages of solution processability, have led to many commercial applications of colloidal quantum dots, such as fluorescent biological probes[36,37], photovoltaics[38,39], and LEDs.[40,41] As with other solid state lighting, the first quantum dot LEDs were monochromatic.[42] Mixing of multiple sizes of quantum dots for white LEDs has also been accomplished, but these suffer from the same color quality drawbacks of multiple-colored LEDs, as well as causing a loss of energy as a consequence of reabsorption of the differing sizes.[43,44] The discovery of ultrasmall CdSe quantum dots by Bowers *et al.* in 2005 provided a single-component white-light emitter, that exhibited a broad emission spanning from 420 nm to 710 nm.[45,46] To use the white-light emission, these quantum dots have been incorporated into electroluminescent devices and as frequency downconverters.[47,48] Even though the electroluminescent devices emit pure white light (CIE coordinates of (0.35, 0.31)) and a high CRI of 93, the luminous efficiency is limited to only 1 lm/W, a result of the synthesized fluorescence quantum yield only averaging 6%. Commonly, to increase the fluorescence efficiency of quantum dots, a shell of a wider band gap material, such as CdS or ZnS is applied.[49,50] For the ultrasmall CdSe a shell eliminates the broad emission by passivating the surface trap sites. In an attempt to enhance the quantum yield of the of white light emission, Rosson *et al.* discovered that a simple post-synthesis treatment with formic acid. This treatment increased the quantum yield to an average of 30%, but with the disadvantage of being unstable due to the dissociation of the formic acid from the surface of the quantum dot, leaving bare Cd to become oxidized. With an alternate approach to brighten the quantum yield without eliminating the trap states, as well as maintaining the stability of the ultrasmall CdSe, high quality white and efficient LEDs can be produced.

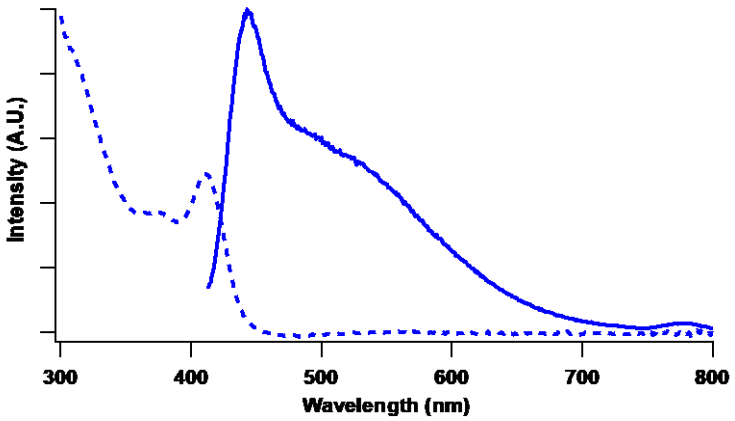

Figure 1.4 Ultrasmall, white light emitting CdSe quantum dot absorption (dashed line) and emission spectra (solid line).

1.3 Scope of This Work

This dissertation provides information on how white light and monochromatic emissive quantum dots are synthesized and incorporated into polymers for various applications. Initially described is the synthesis of nanocrystals, including ultrasmall CdSe and graded-alloy CdSSe quantum dots. This is followed by a description of the post-synthetic treatment of formic acid and citric acid. Next, encapsulation of quantum dots into various polymers are detailed. The final experimental section depicts the characterization of the polymer encapsulated quantum dot samples.

The chapters that follow provide results and conclusions from the three main projects which I worked on during my time at Vanderbilt University. The first (Chapter 3) is the formic and citric acid post-synthesis treatments of the ultrasmall CdSe quantum dots. Then, in situ material state monitoring using embedded ultrasmall CdSe quantum dots and the results are presented (Chapter 4). This is followed by the incorporation of graded-alloy CdSSe quantum dots in 3D printed materials and the analysis of the characterization is provided (Chapter 5).

Finally, a chapter is presented that illustrates the current outlook for the enhancement of quantum dot efficiency and the incorporation of the quantum dots for additive manufacturing. The appendix provides some technical information on color characteristics, and quantum yield calculations.

CHAPTER II

EXPERIMENTAL

2.1 Introduction

In this chapter is described the details on the experimental work done during my time at Vanderbilt University. In section 2.2 the synthesis of quantum dots is described in the following order: 2.2.1 ultrasmall CdSe, 2.2.2 graded-alloy CdSSe. The post-synthesis ligand treatment on ultrasmall CdSe quantum dots is described in section 2.3.1 formic acid and 2.3.2 citric acid.

The encapsulation of and characterization of quantum dots is explained in section 2.4 in four parts. Section 2.4.1 involves the encapsulation with BP-PFCB, section 2.4.2 with epoxy, and section 2.4.3 with polylactic acid. Section 2.4.4 illustrates the characterization techniques and setups used for the analysis of the encapsulated quantum dots.

2.2 Quantum Dot Synthesis

Below is described the synthetic route used for the fabrication of ultrasmall CdSe and graded-alloy CdSSe quantum dots. For each quantum dot batch synthesized, the ration of reactants as well as type of solvent used could be tuned for specific purposes.

2.2.1 Ultrasmall CdSe Synthesis

In order to produce a broad white emission using a single component emitter, ultrasmall CdSe quantum dots are required. The ultrasmall CdSe synthesis that follows was slightly modified from the reactions used by Bowers, *et al.* and Schreuder, *et al.*[45,46,51]

To synthesize the Cd precursor, 1 mmol of Cd (II) oxide and 2 mmol of dodecylphosphonic acid were dissolved in 6 g trioctylphosphine oxide (TOPO), 4 g hexadecylamine (HDA) as high boiling point solvents in a 100 mL, 3-neck, round bottom flask (Figure 2.1). Argon is purged through the flask, while it is heated to 150 °C. At this point, the purge needle was removed, and the temperature increased to 330 °C. At this temperature, the CdO and DDPA react to form a Cd-phosphonate complex, which is indicated by the solution changing from a reddish-brown color to clear and colorless.

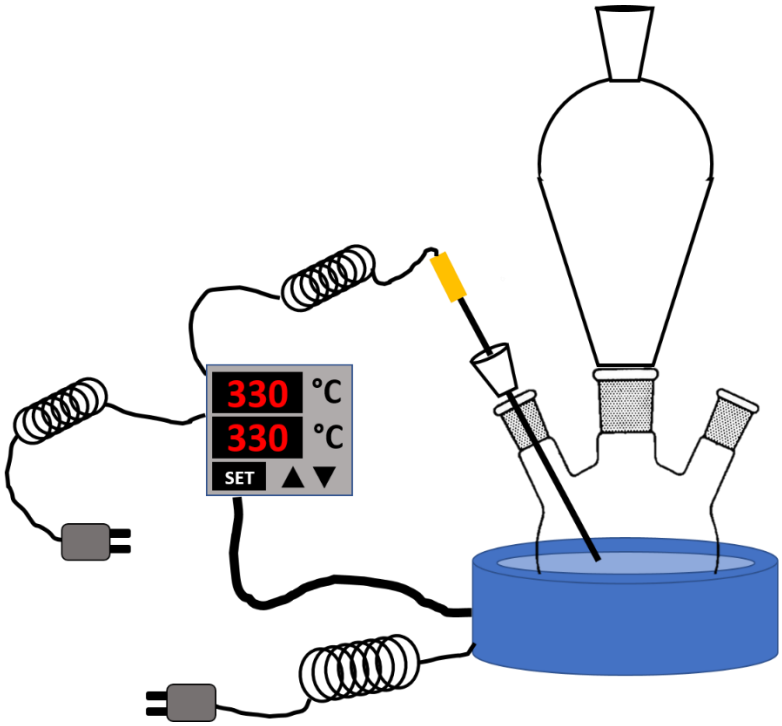

Figure 2.1 Setup for the synthesis of CdSe and CdSSe quantum dots. The reaction mixture is added to the 3-neck, round bottom flask with a stir bar. The flask is placed in a heating mantle, which is powered by pre-set external temperature controller connected to a thermocouple temperature probe. The temperature probe is inserted into one of the necks of the flask, while the other two necks have a self-washing bump trap and a rubber septum. To stabilize the setup, multiple clamps are attached to the fume hood frame. Argon is connected to the bump trap via a 24/40 gas adapter, and a 12-gauge needle is punctured through the septum to be used as an outlet during the purge phase of the synthesis.

A 0.2 M solution of selenium in tri-*n*-butyl phosphine (TBP) was prepared, and 4 mL were swiftly injected into the reaction flask at 330 °C. A second syringe filled with butanol was quickly injected, as soon as a pale yellow color was indicated, at about ~5 seconds after the Se:TBP injection. This cools the reaction to ~180 °C, while compressed air is used to continue cooling the reaction down to 100 °C.

The reaction flask's contents were emptied into four Nalgene centrifuge tubes (50 mL), then filled with methanol, and centrifuged for 5 minutes at 7500 rpm., forming a pellet. After decanting the liquid, the dried pellets were resuspended in a small amount of toluene, to be further purified via gel permeation chromatography. The column was prepared as described by Shen, *et al*.[52] The stationary phase of the column was prepared by swelling poly(styrene-co-divinylbenzene) (200-400 mesh particle size, 2% cross-linked) in toluene for 30 minutes, before pouring into a glass column as shown in Figure 2.2. The quantum dots in solution are then allowed to run through the column and collected in a vial.

In order to confirm a successful synthesis of the ultrasmall CdSe quantum dots (diameter < 2.0 nm), absorption spectra were collected on a Varian Cary 50 Bio ultraviolet-visible (UV-VIS) spectrophotometer with accompanying software. The band-edge absorption peak for these quantum dots should be at less than 420 nm. The emission of the ultrasmall CdSe quantum dots was recorded using a ISS PC1 photon counting spectrofluorometer with Vinci version 1.6.SP5 software. A broad-band emission should be observed for the ultrasmall quantum dots.

2.2.2 CdSSe Graded-alloy Quantum Dot Synthesis

For various applications, including the fabrication of LEDs and biological labeling, photoluminescent quantum yields higher than 10% are required. A typical method of

accomplishing this is by shelling traditional sized CdSe quantum dots with a wider band gap material, such as CdS. Although a shell can confine charge carriers to the core, the abrupt boundary between the core and shell can cause strain due to lattice mismatch, which can induce new trap states. A graded shell will provide surface passivation, while avoiding the strain between the core and shell. The synthesis for CdSSe quantum dots has been slightly modified from that from Keene, *et al.* to scale up.[53]

The synthesis for graded-alloy CdSSe quantum dots was carried out in a setup similar to that of the ultrasmall CdSe quantum dots, with the exception of a 250 mL round bottom flask instead of the 100 mL round bottom flask. The Cd precursor is prepared by mixing 4 mmol CdO and 16 mmol oleic acid (OA) in 80 mL ODE in the 250 mL flask and heated to 300 °C under argon purging, until the solution is clear and colorless. The selenium and sulfur precursor are prepared by dissolving the elemental powders in TBP to make two 2 M solutions. 0.84 mL of the 2 M S:TBP solution, 0.36 mL of the 2 M Se:TBP solution, and 2 mL of octadecene (ODE) are mixed and injected swiftly into the reaction flask. The temperature is then lowered to 260 °C, and the reaction is stirred for 2 hours. The solution is then cooled with compressed air and separated into 8 Nalgene centrifuge tubes. The tubes are filled with a 3:2 (by volume) mixture of butanol:ethanol, and centrifuged at 7500 rpm for 15 minutes. The pellet is resuspended in toluene and further purified in a column of poly)styrene-co-divinylbenzene).

2.3 Quantum Dot Ligand Exchange

With the quantum yield of the as synthesized, ultrasmall CdSe quantum dots being on average only 6%, a method was needed to increase the fluorescence intensity. This was accomplished by Rosson, *et al.* by performing a post-synthesis ligand exchange with carboxylic

acids, specifically formic acid. The following ligand exchanges are performed with a method similar to that described by Rosson, *et al.*[54]

2.3.1 CdSe Formic Acid (CdSe-FA) Ligand Exchange

A 5-50 mL solution of ultrasmall CdSe quantum dots with a concentration typically between 50 and 300 μM in toluene was added into an 11 dram vial with a stir bar and placed in an aluminum heating block on a hot plate with a temperature probe. Formic acid was added to the quantum dot solution in a 30,000 molar excess via syringe injection to the vial at the same time heating was started. The solution was heated from room temperature to 60 °C, and immediately removed from heat and cooled with compressed air back to room temperature. The solution was transferred to micro-centrifuge tubes and centrifuged at 2500 rpm for 10 minutes to remove the excess formic acid from the treated quantum dots. The supernatant was then gently transferred to a vial to decrease the amount of formic acid being dissociated from the surface of the quantum dots.

2.3.2 CdSe Citric Acid (CdSe-CA) Ligand Exchange

The ultrasmall CdSe quantum dots are treated with citric acid in a similar way to the formic acid treated CdSe quantum dots.[55] A 5-40 mL solution of 50 to 300 μM CdSe quantum dots in toluene is added to a vial with a stir bar and placed in an aluminum heating block with a temperature probe. Citric acid is then added to the vial in a 2,500 molar excess and the vial is heated from room temperature to 60 °C. As soon as the temperature reaches 60 °C, the vial is immediately removed from heat and cooled with compressed air to room temperature. As citric acid is a solid, the quantum dot solution is decanted from the excess citric acid and poured into micro-centrifuge tubes. The solution is centrifuged at 2500 rpm for 5 minutes and the supernatant poured into a vial.

2.4 Quantum Dot Encapsulation

With the discovery of white-light emitting quantum dots, an apparent application to be examined was solid-state lighting. This was accomplished by Schreuder, *et al.* in two methods.[47,56] The first of which involved using the broad photoluminescence of the ultrasmall CdSe quantum dots in an encapsulating polymer. The encapsulation provides protection against heating and photo-oxidation as well as a mechanically stable environment. An optimal polymer would have no intrinsic emission and prevent the quantum dots from aggregating. One such polymer discovered was biphenylperfluorocyclobutyl (BP-PFCB), which provided the most stable environment for the ultrasmall CdSe quantum dots, maintaining the pure white CIE coordiantes (0.324, and 0.322) and a high color rendering index (93), but only a 1 lm/W, due to the average fluorescence intensity being only 6%. With the increased intensity of the formic acid treated CdSe quantum dots, the possibility of a brighter device was feasible.

2.4.1 *Encapsulation with BP-PFCB*

Films of BP-PFCB were prepared by suspending the polymer in a 20% w/w ratio in mesitylene. CdSe-FA quantum dots in toluene are mixed in various ratios in the solvated BP-PFCB and drop cast into the bottom of a glass vial. The film is then degassed for 15 minutes in a glove box's small antechamber at 30 in. Hg vacuum. The films are then placed in an oven under ambient atmosphere to be cured at 60 °C for ~20 hours. The cured films are removed from the glass vials through gentle sonication in deionize water and lifting with a X-acto blade.

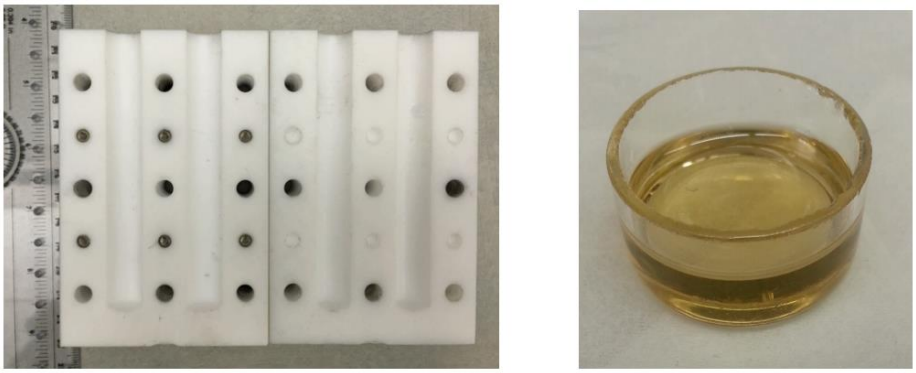

Figure 2.2 Cylindrical sample molds made from a Teflon block and held together by aluminum plates and bolts (left). Thin disc samples are fabricated in the bottom of a glass vial (right). Dimensions of the cylinder samples are 12.7 mm x 25.4 mm and the thin disc are 25.4 mm x 2.45 mm (diameter x height).

2.4.2 Encapsulation with Epoxy

Samples of ultrasmall CdSe quantum dots encapsulated in epoxy were prepared by thoroughly mixing equal parts by weight of 6100-1A resin and 6100-1B hardener from Aptek Labs.[57,58] Various ration of ultrasmall CdSe quantum dots in chloroform were then added to the mixture and further mixed and de-gassed in a sonicating bath. The mixture is then poured into either the bottom of a glass vial, into a custom-made cylindrical mold (Figure 2.2)[57], or onto aluminum and fiberglass tensile samples (Figure 2.3).[58] The glass molds were coated in a white lithium paste serving as a mold release to help remove samples after curing. The samples were cured in an oven at 80 °C.

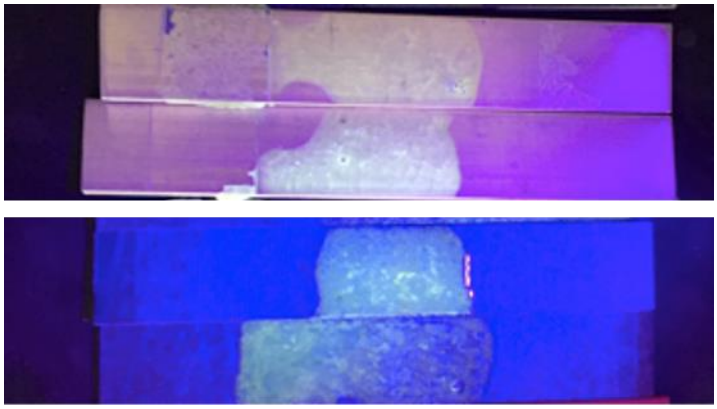

Figure 2.3 Aluminum tensile samples (top) with dimensions of 6” x 1” x 0.125”. The epoxy/CdSe film thickness is 0.015”. Fiberglass tensile samples (bottom) with dimensions of 5.6” x 1” x 0.13”. The epoxy/CdSe film thickness is 0.02”.

2.4.3 Encapsulation with Polylactic Acid

Polylactic acid (PLA) nanofunctionalized filament was fabricated by first dissolving PLA pellets in dichloromethane while stirring, typically 2.5 mL/1 g (Figure 2.4). CdSSe quantum dots in toluene were then added to the mixture in various ratios.[59] The PLA/CdSSe quantum dot mixture was then further stirred to ensure the quantum dots were evenly dispersed in the PLA matrix. The resulting PLA/CdSSe mixture was dried overnight to remove excess solvent and the remaining hard plastic was shredded to acquire small pellets. A Filabot EX2 single screw material extrusion system was heated to 180 °C, and the shredded composite was dispensed from the hopper into the screw compartment. As the filament is extruded from the nozzle, it is cooled in a water bath before being spooled. The resulting functionalized filament is approximately 2.85 mm in diameter and is ready for printing.

Figure 2.4 Polylactic acid (PLA) nanofunctionalized filament fabrication. Quantum dots in solution are dispersed in PLA dissolved in dichloromethane. The mixture is dried overnight, and the remaining hard plastic is shredded to acquire small pellets. The shredded composite is extruded into a filament ready for 3D-printing.

An Ultimaker 3+ extended dual nozzle fused deposition modeling (FDM) type 3D printer was used to fabricate thin film and dogbone samples. The filament was extruded through a 0.4 mm print nozzle heated to 215 °C and deposited onto a heated build plate set to 60 °C. All samples were printed with a 1 mm print layer height and 100% material infill.

2.5 Encapsulated Quantum Dot Sample Characterization

Many experiments and material characterizations are performed to reveal the overall effects of encapsulating quantum dots into various polymers.

2.5.1 Compression Testing

Cylinder and thin disc samples were first observed using a Zeiss fluorescence microscope to obtain a baseline, undamaged image of the epoxy/CdSe samples. Baseline emission data was

then collected using a Labsphere SLMS-LED-1050 integrating light sphere system, fiber coupled to a CDS 600 CCD-based spectrophotometer and accompanying software. Samples were excited using a 10 mW, 405 nm laser. A filter with a cutoff wavelength of 410 nm was used to minimize contamination from the laser excitation source in the recorded emission data. After microscopy and emission data had been recorded, samples were loaded in compression at 250 lb increments, up to a maximum load of 1250 lbs (Figure 2.5).

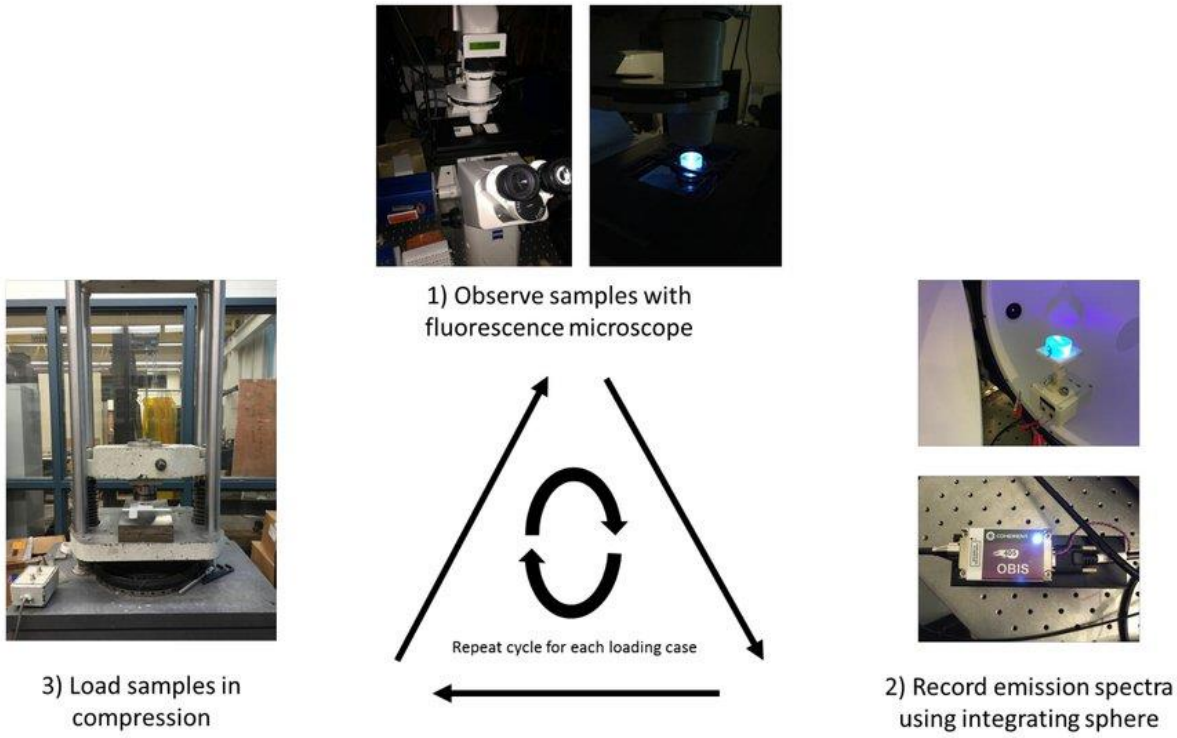

Figure 2.5 Compressive testing setup.

2.5.2 Tensile Testing

Emission data for the epoxy/CdSe coated tensile samples were recorded in situ under the application of external loads. Samples were excited with a 20 mW laser excitation source with

the emission data being recorded with a CDS 600 CCD-base spectrophotometer and 410 nm cutoff filter. Testing was performed in a dark room to minimize the presence of external light sources. A background emission scan was performed prior to each test to account for ambient light present in the testing room, including the emission given off by the computers being used for data collection. The background scan was automatically subtracted from each recorded scan by the OceanView spectroscopy software.

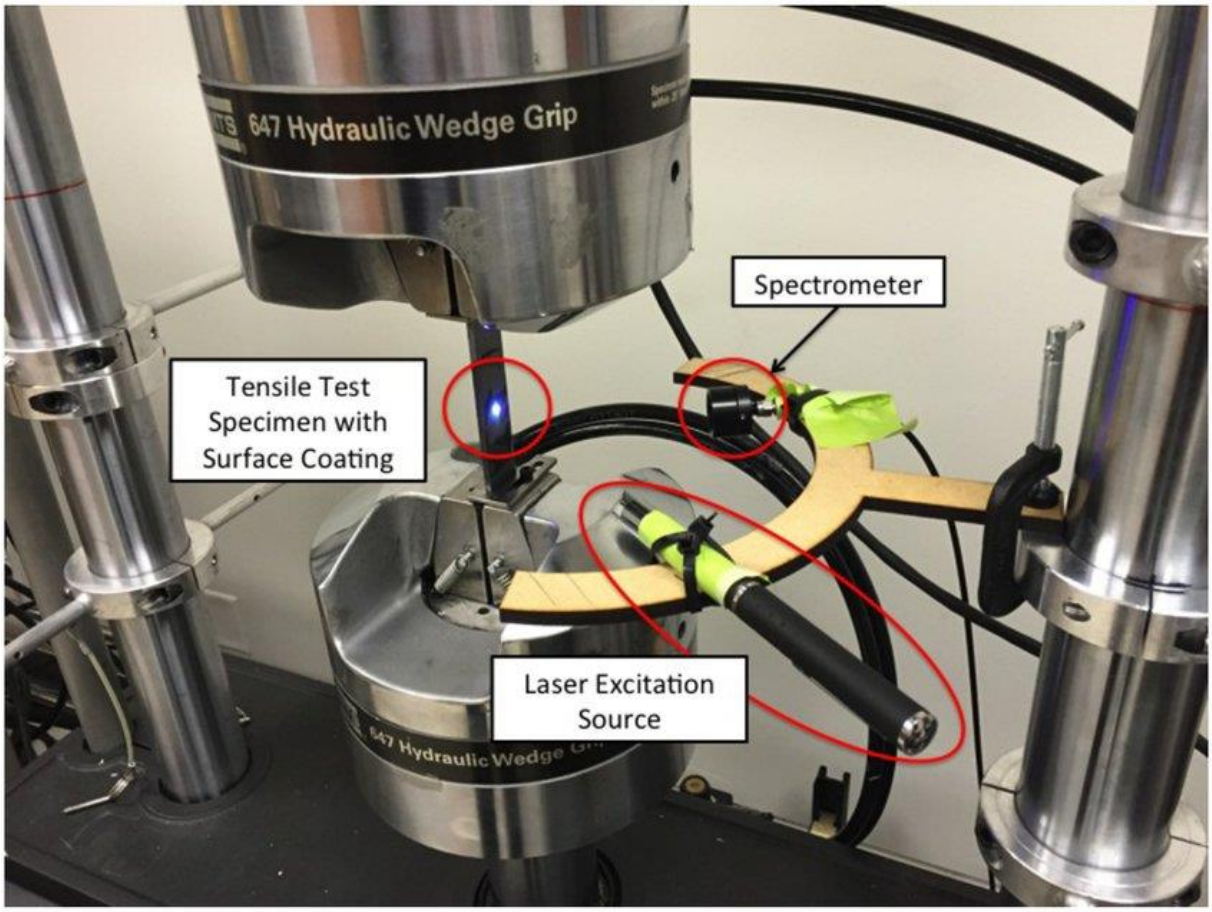

Figure 2.6 Tensile testing setup

2.5.3 Thin Film Optical Characterization

Absorbance measurements for BP-PFCB/CdSe-FA films and the 3D printed PLA/CdSSe films were recorded in the visible range from 400-800 nm using a Cary 60 UV-VIS spectrophotometer and accompanying software with a scan rate of 4800 nm/min. For the 3D printed films, a total of nine scans, recorded at three distinct locations from three individual films, were analyzed and averaged.

Photoluminescence measurements were recorded using a PTI spectrofluorometer with an excitation of 350 nm for the BP-PFCB/CdSe films and 500 nm for the PLA/CdSSe films. Custom stands were used to support the films to ensure uniform orientation and positioning between individual scans (Figure 2.7). For the 3D printed, PLA/CdSSe films, averages and standard deviations were recorded from three samples for each concentration of quantum dots in PLA.

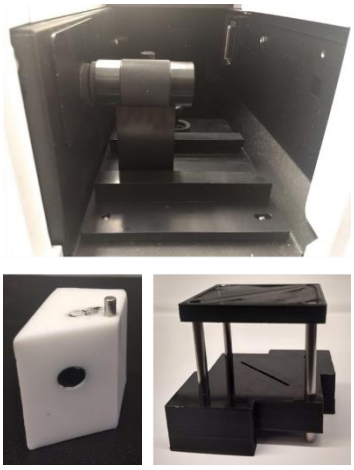

Figure 2.7 A) Image of the film holder in the Cary 60 UV/VIS spectrophotometer. B) Image of the BP-PFCB/CdSe film PL testing setup. C) Image of the 3D printed film testing setup.

2.5.4 Transmission Electron Microscopy

Transmission and scanning transmission electron microscopy (TEM/STEM) images for ultrasmall CdSe, CdSe-CA, and CdSSe quantum dots in solution and 3D printed PLA/CdSSe films were recorded using a FEI Tecnai Osiris 200 kV electron microscope. For the quantum dot solution samples, the solution was dropcast onto an ultrathin carbon-coated copper grid (Ted Pella, Inc.) and wicking away excess solvent. The CdSe and CdSe-CA quantum dot samples were further baked at 145 °C overnight. PLA/CdSSe samples were microtomed to obtain thin slices, approximately 75 nm in thickness, which were then supported onto a nickel grid prior to imaging. PLA/CdSSe samples were imaged using STEM with low beam current setting (spot size of 11, low extraction mode) to reduce beam damage to the PLA. Microscopy images and corresponding quantum dot sizes were analyzed using ImageJ software.

2.5.5 Thermal Characterization

Differential scanning calorimetry (DSC) testing was performed on the 3D printed PLA/CdSSe samples using a TA Instruments Q 2000 under nitrogen purge (50 mL/min). Samples were equilibrated at -25 °C and heated to 225 °C at a rate of 25 °C/min, where the temperature was held isothermally for 5 minutes before being cooled back to -25 °C. A total of three scans were run for each sample, and corresponding thermal data were recorded from the final scan. Averages and standard deviations were calculated from three samples for each weight percent of PLA/CdSSe examined.

Thermogravimetric analysis was performed on the 3D printed PLA/CdSSe samples using a TGA 1000 under nitrogen purge (100 mL/min). Samples were heated from 25 °C to 500 °C, and the corresponding residual weight loss was monitored for each weight percent of PLA/CdSSe examined.

2.5.6 *Mechanical Testing*

Mechanical testing was performed on the 3D printed PLA/CdSSe samples printed in a ASTM D638 Type V tensile dogbone specimen (Figure 2.8). The specimens were loaded at a rate of 5 mm/min under displacement control. A minimum of three tensile specimens were average to obtain the data.

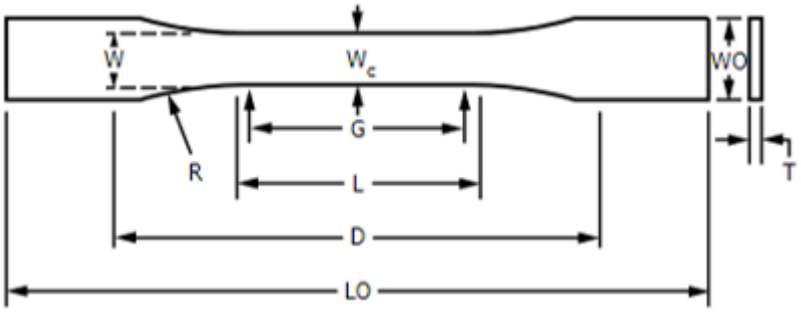

Figure 2.8 Diagram of ASTM D638 Type V Tensile Test Specimen. Dimensions include: Width of narrow section (W), 3.18 mm; Length of narrow section (L), 9.53 mm; Width overall (WO),9.53 mm; Gauge length (G), 7.62 mm; Distance between grips (D), 25.4 mm; Radius of fillet (R), 12.7 mm; and Thickness (T), 4 mm.

CHAPTER III

FORMIC AND CITRIC ACID CAPPED QUANTUM DOTS

3.1 Introduction

The United States reportedly consumed approximately 6% (232 billion kWh) of the county's total electricity use on lighting in 2018.[1] Due to the average lighting efficacy increasing more than 40% since 2001, progress is being made to reduce the energy cost of lighting. This is owing in part to the significant strides being made in light emitting diode (LED) technologies.[14] LEDs can produce the same brightness (~1,500 lumens) as the incandescent bulb, while utilizing a fraction of the energy.[21] Although LEDs are more durable and longer lasting, they are deficient when it comes to light quality, being comprised of either blending multiple phosphors or by a blue-emitting LED coupled with a yellow phosphor. Typically, LEDs have a lower color rendering index (CRI) value (less than 80) compared to sunlight (100). Mixing multiple phosphors can help increase the CRI, however this can become difficult and expensive.[20] A single phosphor design would meet the goals of being simpler to produce, as well as being more energy efficient, since there would not be the issue of the phosphor absorbing light emitted by other particles. For these devices to be commercially viable, the luminescent material must be abundant, inexpensive, chemically and thermally stable, and provide a high CRI.

Quantum dots have been studied extensively over the past thirty years, owing to their size tunable band gaps, narrow photoluminescence, and lasting photostability.[60–62] These properties have led to commercial applications of quantum dots as phosphors for solid-state lighting[40], fluorescent biological probes[36,37], and display technologies.[41] The fabrication of the first reported

monochromatic quantum dot LED in 1994 has led to the advance of white light-emitting devices using quantum dots.[42,43,47,63,64] Quantum dot LEDs have since then received attention in applications for large-area plane light sources and for back-lighting, although many of these devices employ mixing of multiple sizes of quantum dots, causing a loss of energy as a effect of reabsorption of the differing sizes of quantum dots.[44,65,66]

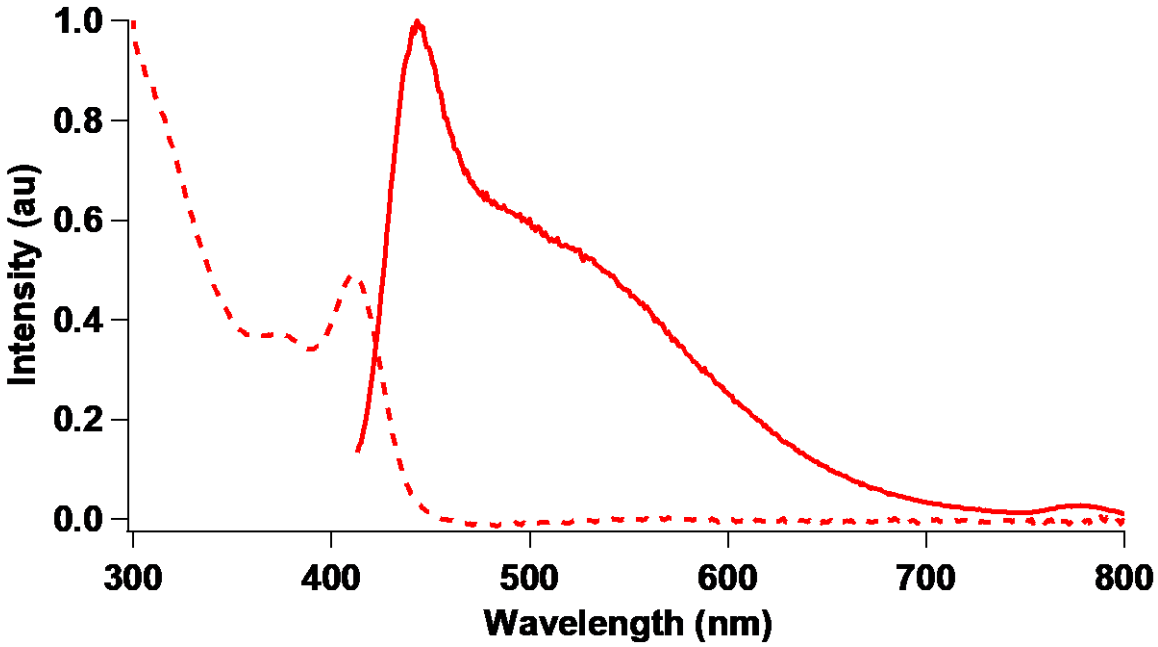

Figure 3.1 Absorbance (dashed) and emission (solid) of ultrasmall CdSe quantum dots.

The discovery of ultrasmall CdSe quantum dots offered a single-component white-light emitter, exhibiting a broad emission that spans from 420 nm to 710 nm (Figure 3.1).[45] These quantum dots have diameters less than 2 nm, with 70% of the atoms on the surface. The high surface area-to-volume ratio of the particles gives rise to emissive surface trap states, characterized by three unique emission peaks that comprise the broad emission.[46,67] Since the

discovery of the ultrasmall white-light emitting CdSe quantum dots, much work has been done on understanding the interface between the ligands and the surface of the quantum dots, especially with how it relates to light emissive applications.[68–70] To utilize the white light-emission, these ultrasmall CdSe quantum dots have been implemented into electroluminescent devices and as frequency downconverters.[48,56] Although the electroluminescent devices emit pure white light, with Commission Internationale de L'Eclairage 1931 (CIE) coordinates of (0.35, 0.31) and a high color rendering index of 93, the as-synthesized fluorescence quantum yield of these CdSe quantum dots only averages 6%, which limits the luminous efficiency to only 1 lm/W.[48] Historically, to improve the fluorescence efficiency of CdSe quantum dots a method of shelling the particles with a wide band gap material, such as ZnS or CdS was employed.[49,71] This method can increase the quantum yield of conventional nanocrystals to near unity[50,72,73], however, for the ultrasmall CdSe quantum dots, the shell passivates the surface trap sites and eliminates the broad emission. Rosson et al. found that a simple post-synthesis treatment of the ultrasmall CdSe quantum dots with formic acid increases the quantum yield to an average of approximately 30%.[54] The increase in brightness is a result of a partial ligand exchange with the phosphonic acid, as well as the passivation of an additional nonradiative surface trap sites by formic acid. While all three peaks of the broad emission increase with the formic acid treatment, the first emission peak is enhanced to a greater degree than the other two peaks, causing a cooling effect on the white light, with a shift of the CIE coordinates from (0.31, 0.33) to (0.24, 0.24). Although these particles are brighter, they are unstable, due to dissociation of the formic acid from the surface of the quantum dot, leaving bare Cd to become oxidized. A different approach must be taken to brighten the quantum yield without eliminating trap states, as

well as maintaining the stability to allow for solution processability without a degradation of the optical output.

First, the formic acid treated CdSe (CdSe-FA) quantum dot's optical spectra are observed to compare to the synthesis of Rosson, *et al*, as laid out in Chapter 2. The ultrasmall CdSe quantum dots are also treated with citric acid to enhance the fluorescence intensity, while maintaining the broad white light emission. Absorption and emission spectra are recorded, as well a stability test for both the CdSe-FA and CdSe-CA quantum dots. The band gap absorption and position of the first emission peak of the CdSe quantum dots was monitored before and after citric acid treatment to determine the effect on band gap versus pinned emission.

3.2 Results and Discussion

3.2.1 Quantum Yield Effects

The first experiments done in this study to improve the quantum yield of ultrasmall CdSe white-light-emitting quantum dots were with formic acid treatments as described in Chapter 2. A representative absorption and emission spectra of the CdSe-FA quantum dots is shown in Figure 3.2A. The ultrasmall CdSe quantum dots before treatment had an average quantum yield of 6.5% and CIE coordinates of (0.30, 0.34). After the quantum dots had been treated with formic acid, the average quantum yield increased to 21.2 ± 10.2% (n=29) and the CIE coordinates shifted to (0.26, 0.30). The quantum yield and CIE coordinate calculations can be found in Appendix A and B, respectively.

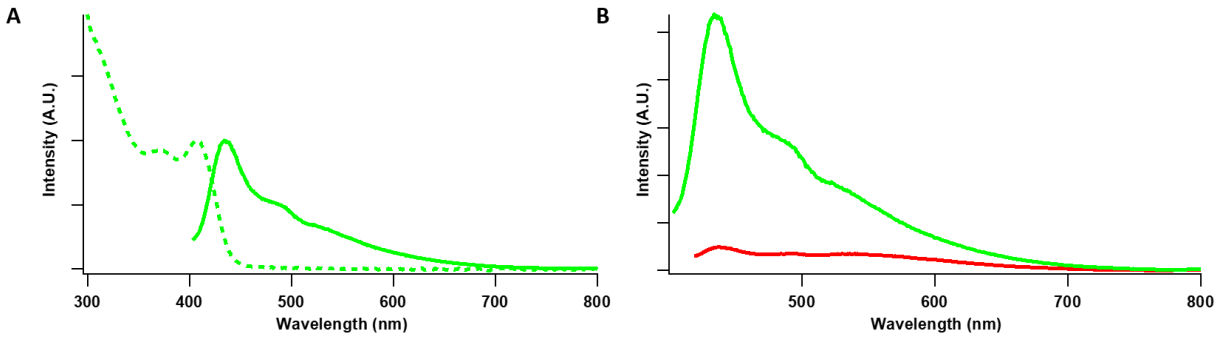

Figure 3.2 A) Absorption (dashed) and emission (solid) spectra for ultrasmall CdSe quantum dots treated with formic acid (CdSe-FA). B) Comparison emission spectra between CdSe quantum dots (red) and formic acid treated CdSe quantum dots (green).

It was reported by Rosson, *et al.* that the increase in quantum yield is from two processes. The first of which is due to the partial ligand exchange with the native phosphonic acid ligand. Since the phosphonic acid is more strongly bound to the surface of the quantum dot than what a carboxylic acid would be bound, it takes heat and an excess of the free ligand to be exchanged. This is the reason that formic acid is added to the CdSe quantum dot solution in a 30,000 molecular excess. It is believed that only a partial ligand exchange occurs due to the difference in solubility of the phosphonic acid versus the formic acid. If the surface of the quantum dot was completely covered by formic acid, the solubility in toluene would be greatly reduced. As the quantum dots are still soluble in toluene, this is not the case. The second process that is responsible for the increase in fluorescence intensity is that the formic acid can passivate a previously non-radiative trap site on the surface of the CdSe quantum dot. If a complete exchange of surface ligands had occurred, the new surface ligand would have to interact with all three of the processes that produce white light. Since the formic acid is found to more greatly affect the first emission peak of the broad white light, by both blue-shifting and increasing the

intensity, it does not appear to affect all three emission peaks. This is observed with the CIE coordinates being "bluer" after the formic acid treatment (Figure 3.3C).

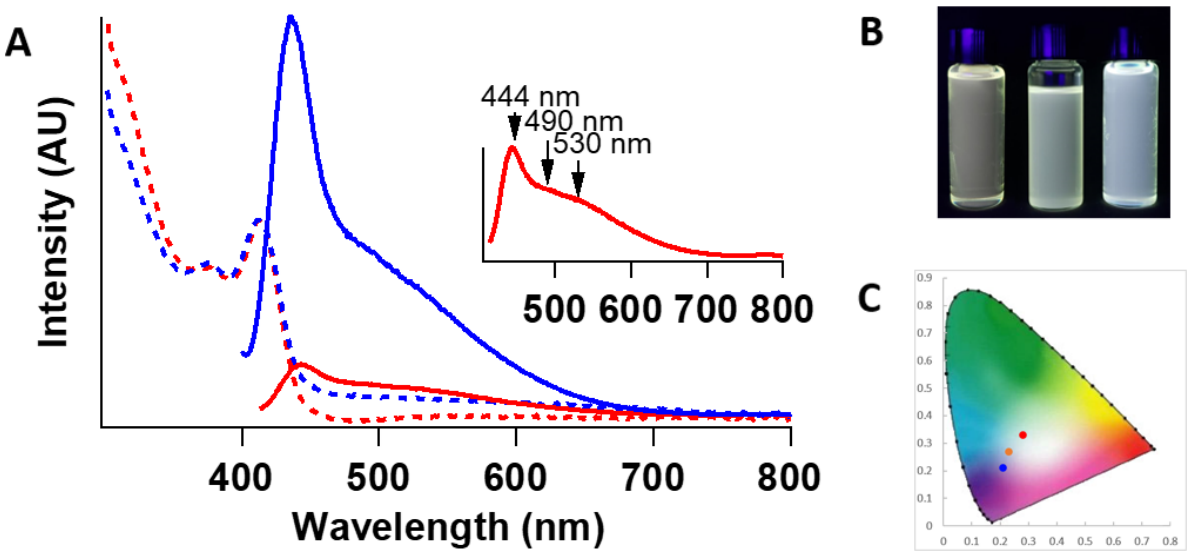

Figure 3.3 A) Absorbance (dashed) and emission (solid) spectra of ultrasmall CdSe quantum dots (red) and citric acid treated ultrasmall CdSe quantum dots (blue) (Ex: 400nm, slit width 2.0 mm). The inset is the photoluminescence spectra of the ultrasmall CdSe quantum dots to show the three emission features. B) Vials containing white-light ultrasmall CdSe quantum dot solutions before (left) and after formic acid (middle) and citric acid (right) treatment under black light excitation. C) CIE chromaticity coordinates of ultrasmall CdSe quantum dots (0.30, 0.32) (red), formic acid treated ultrasmall CdSe (0.23, 0.28) (orange) and citric acid treated ultrasmall CdSe quantum dots (0.21, 0.22) (blue).

Next the ultrasmall CdSe quantum dots were treated with citric acid. The untreated CdSe quantum dots displayed an absorbance peak at 411 nm, corresponding to particles with a calculated size of 1.65 nm in diameter (Figure 3.3A).[55] After purification, these quantum dots have an average quantum yield of 5.7%. The broad white emission is observed to have peaks at 444, 490, and 530 nm. After the citric acid treatment, the absorbance of the CdSe quantum dots

slightly blueshifts. On the other hand, a significant difference is seen in the intensity of the emission spectra for CdSe-CA quantum dots, which have an average quantum yield of 33.4±14.0% (n=87), with a max value of 61.3%, the highest reported quantum yield for a single emitting white light quantum dot to date. Transmission electron microscopy (TEM) of the untreated ultrasmall CdSe quantum dots shows good monodispersity. After the treatment with citric acid, the TEM shows aggregates of approximately 20 nm in diameter. When analyzed with scanning transmission electron microscopy (STEM), it was found that these aggregates are not larger quantum dots, but a cluster of the ultrasmall quantum dots.

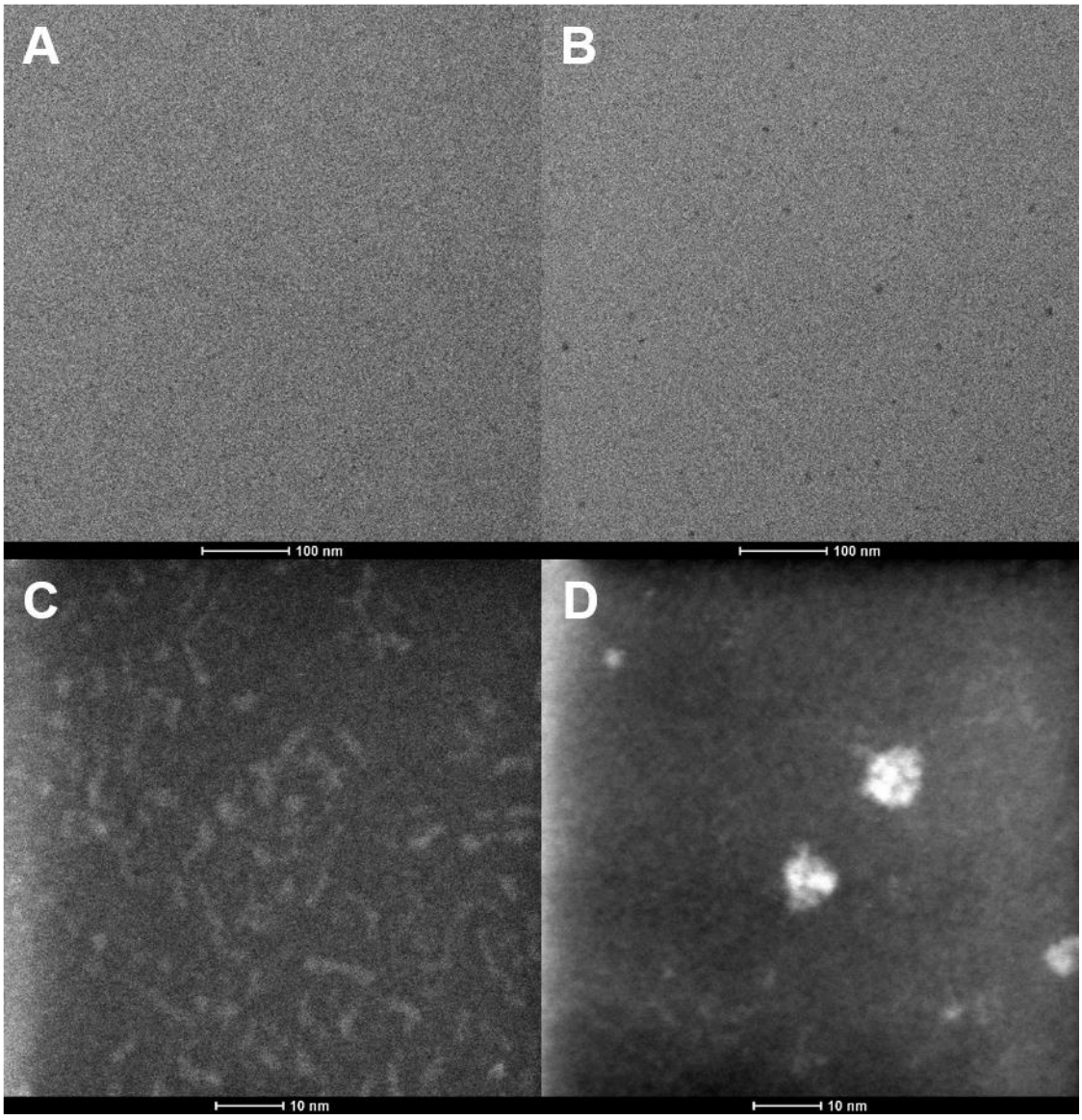

Figure 3.4 TEM images (A and B) and STEM images of ultrasmall CdSe and CdSe-CA quantum dots.

In addition to an enhancement of the quantum yield, the Stokes shift between the band edge absorption peak and the first emission feature is considerably reduced. The new Stokes shift is on the order of a few nanometers, like classically observed band-edge recombination. Figure

3.5 summarizes possible pathways of electron and hole recombination that give rise to the three unique emission peaks. These three emission peaks arise from pinned emission associated with a trap state at the phosphonic acid ligand (pathway 1), surface selenium states (pathway 2), and deep trap states (pathway 3). The first emission peak at 440 nm is pinned (pre-treatment) at this wavelength due to a trap sate associated with the phosphonic acid ligand on the surface of the quantum dot.[51,74] The second emission peak at 488 nm is believed to be a result of a surface state at Se atom sites, which is supported by the observation of the peak's insensitivity to ligand exchanges.[46,74] The broad emission around 550 nm, is a result of classical deep trap emission.[75] After the citric acid treatment, the energy state from the phosphonic acid ligand is no longer available, so some emission reverts to band gap recombination, resulting in the smaller observed Stokes shift.

Figure 3.5 B compares how the absorption and emission changes with decreasing nanocrystal diameter for both conventional ultrasmall and citric acid treated CdSe. Dukes, et al. determined that the first emission peak of white-light CdSe quantum dots is pinned at a distinct wavelength, caused by the phosphonic acid ligand inducing a size independent trap state that is at a lower energy than that of the conduction band.[74] As the diameter of the untreated ultrasmall CdSe is decreased, the first emission peak blue shifts until the diameter of the quantum dot reaches ~ 1.7 nm. Below this size, the position of the first emission peak remains constant or pinned regardless of the quantum dot diameter. The citric acid treated dots, however, exhibit quantum confinement behavior as seen with the Brus model, where, as the size of the quantum dot is decreased, the band gap energy increases. Here, it was found that the highest energy emission remains size dependent for diameters much smaller than 1.7 nm. The recovery of the band gap emission is possibly a result of the partial ligand exchange with the phosphonic acid.

As the phosphonic acid is removed, the pinned surface state is no longer available, and the electron relaxes from the conduction band to the valence band. As with the formic acid treated CdSe, evidence that only a partial ligand exchange occurs with the citric acid instead of a complete ligand exchange is the continued solubility in toluene.

Although the CdSe-CA quantum dots revert to bandgap emission, the three emission peaks are maintained after the citric acid treatment, and similar to the formic acid treated particles, the first peak increased more in intensity relative to that of the other two peaks. This corresponds to an overall change in the average CIE coordinates from (0.30, 0.36) to (0.26, 0.32) (Figure 3.3 C). Interestingly, the intensity for the deep trap emission increases as well. The increase in deep trap emission could be a result of increased lattice strain, the creation of point defects in the crystal lattice caused by the ligand exchange, or the process is no longer in competition with the pinned emission trap state allowing more charge carriers to relax through the third process (Figure 3.5 A, step 6).[46]

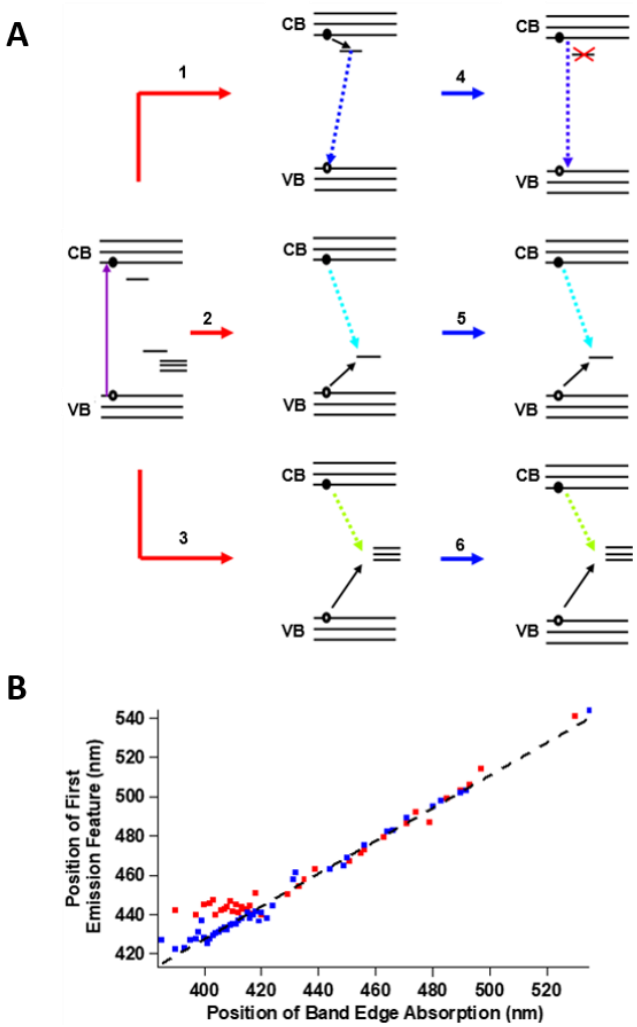

Figure 3.5 A) Possible emission mechanism in ultrasmall CdSe quantum dots. Electrons (filled circles) are excited to the conduction band (CB) by the absorption of light, leaving a positively charged hole (empty circles) in the valence band (VB). Three possible pathways for emission (red arrows) are available through pinned emission from the phosphonic acid ligand (1), a surface state at the selenium atom (2), and deep trap emission (3). After CA treatment (blue arrows), the pinned emission is no longer apparent and is now replaced by that of band gap emission (4). Selenium surface state (5) and the deep trap emission (6) are still present. (B) Position of the first emission feature is plotted against the position of the band-edge absorption for CdSe quantum dots (red) and CdSe−CA quantum dots (blue). Dashed line represents the trend of quantum confinement.

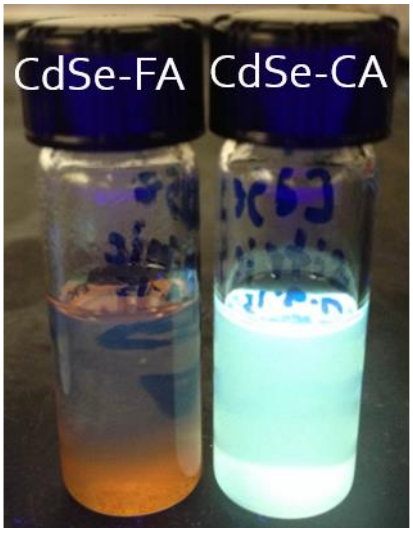

Figure 3.6 Comparison of CdSe-FA and CdSe-CA quantum dots after 25 days. The fluorescence of the CdSe-FA quantum dots has completely quenched, whereas the CdSe-CA quantum dots have a quantum yield of 29.9%.

While the formic acid treated CdSe quantum dots previously had the highest fluorescence QY for a single emitting white light quantum dot, they exhibited significant instability in the solution over time, with a substantial decrease in the fluorescence intensity (Figure 3.6). The efficiency loss is likely due to an equilibrium effect between surface bound and free formic acid. As the formic acid becomes unbound from the surface of the quantum dot, sites for oxidation can emerge. For comparison, the optical properties of a citric acid treated ultrasmall CdSe solution was observed for stability over time. Directly after the post-synthesis treatment, the QY was measured to be 36%. Over the course of 21 days with the sample exposed to air, the QY only degraded to 31% (Figure 3.7). The improved stability as compared to formic acid could be the result of the multidentate binding capability of citric acid, which has three carboxylic acid groups.

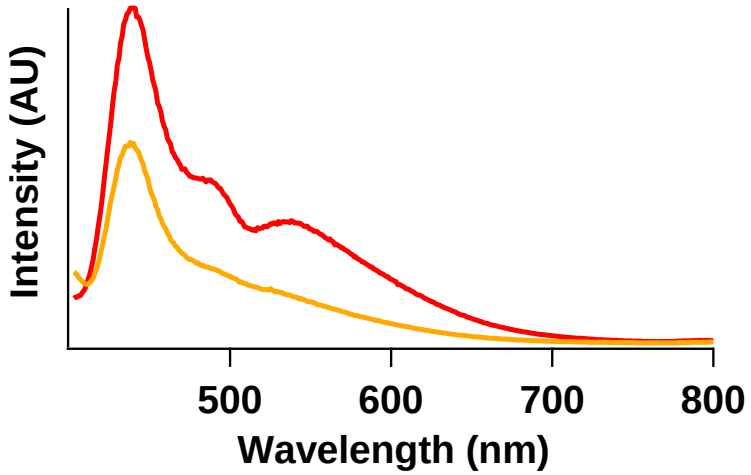

Figure 3.7 CdSe-CA quantum dots PL spectra immediately after synthesis (red) and after 21 days (orange).

3.2.2 Spectroscopy Analysis

In the previous experiments, analysis techniques, such as absorption spectroscopy, photoluminescence spectroscopy, and transmission electron microscopy were used to monitor the changes in the size of the quantum dots and the optical characteristics after the ligand treatments. To be able to analyze the ligands and how they are bound to the surface of the quantum dots, other techniques need to be employed, such as infrared (IR) spectroscopy and nuclear magnetic resonance (NMR) spectroscopy.

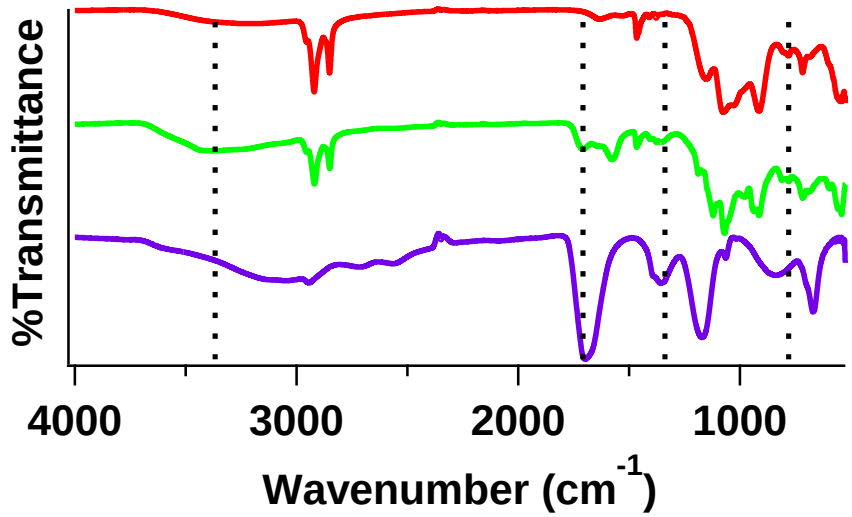

Figure 3.8 IR spectra for CdSe quantum dots (red), CdSe-FA quantum dots (blue), and formic acid. The dashed lines indicate the ν O-H (3367 cm^{-1}), ν C=O (1708 cm^{-1}), ν C-O (1339 cm^{-1}), and the ν P-C (750 cm^{-1}).

The IR spectra for CdSe quantum dots (Figures 3.8 and 3.9) has vibrations characteristic of the stretching and bending modes of the ligands used in the synthesis (Table 3.1). These peaks are slightly shifted compared to the free molecules due to being either bound to or in close proximity to the quantum dot surface.[76] After treatment with the formic acid (Figure 3.8) and the citric acid (Figure 3.9) the IR spectra now show peaks characteristic of both the carboxylic acids and the ligands used for the CdSe synthesis. The broad O-H peak in the CdSe-FA spectra is still present, which indicates that there is free formic acid not attached to the surface of the quantum dot. Further it is seen that the O-H peak is no longer visible in the CdSe-CA IR spectrum. This could be due to the way that the citric acid ligand binds to the surface of the quantum dot.

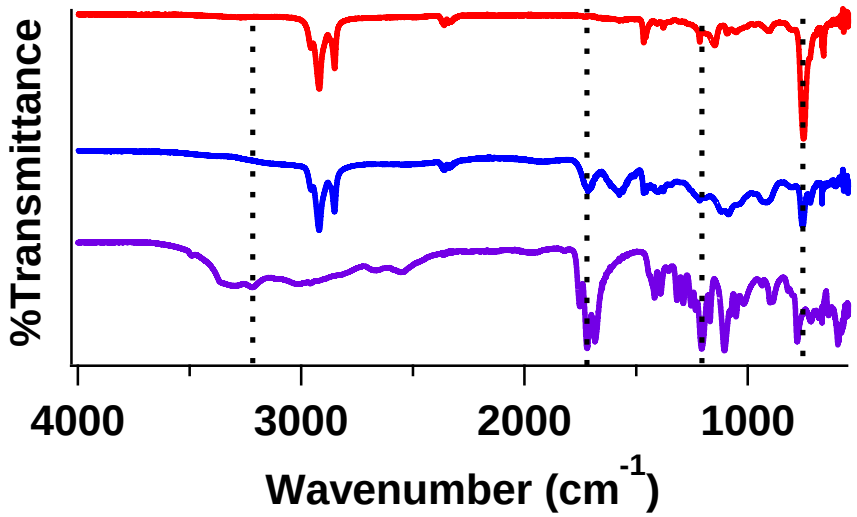

Figure 3.9 IR spectra for CdSe QDs (red), CdSe-CA QDs (blue), and citric acid (purple). The dashed lines indicate the ν O-H (3217 cm^{-1}), ν C=O (1720 cm^{-1}), ν C-O (1220 cm^{-1}), and the ν P-C (750 cm^{-1}).

Table 3.1 Peak assignments for CdSe quantum dots, CdSe-FA quantum dots, formic acid, CdSe-CA quantum dots, and citric acid

	CdSe Quantum Dots	**CdSe-FA Quantum Dots**	**Formic Acid**	**CdSe-CA Quantum Dots**	**Citric Acid**
Wavenumber (cm^{-1})	**Assignment**				
ν O-H		3367	3128		3217
ν_s NH	3320	3236		3380	
ν_s CH_3, ν_{as} CH_3	2960, 2910	2954, 2866		2940, 2860	
ν_{as} CH_2, ν_s CH_2	2920, 2850	2919, 2850		2920, 2850	
ν PO-H	2360				
ν_{as} C=O, ν_s C=O		1705	1698, 1652	1720	1720, 1715
δ NH_2	1580	1631		1580	
ν C-O			1352	1220	1205
ν COH			1170		1104
ν P=O	1150				
ν_s P-OH, ν_{as} P-OH	1090, 1050	1068, 1052		1100, 1090	
ν P-C	750	716		754	

In addition to the IR spectroscopy, ^{1}H NMR spectroscopy was also obtained for the CdSe (Figure 3.10) and CdSe-CA (Figure 3.11) quantum dots. Characteristic peaks for aliphatic protons on the carbon chains of the TOPO, HDA, and DDPA ligands are observed. It is difficult to ascertain which chemical shifts correlate to each ligand since all the ligands contain CH_2 and CH_3 functional groups. After the treatment with the citric acid, a broad peak arises from the CH_2 groups in the citric acid (Figure 3.11 inset). Although this confirms that citric acid is present in the CdSe-CA solution, it is not confirmed that the citric acid is bound to the surface. It is reasonable to believe that the citric acid is bound to the surface owing to the broadness of the peak.[77]

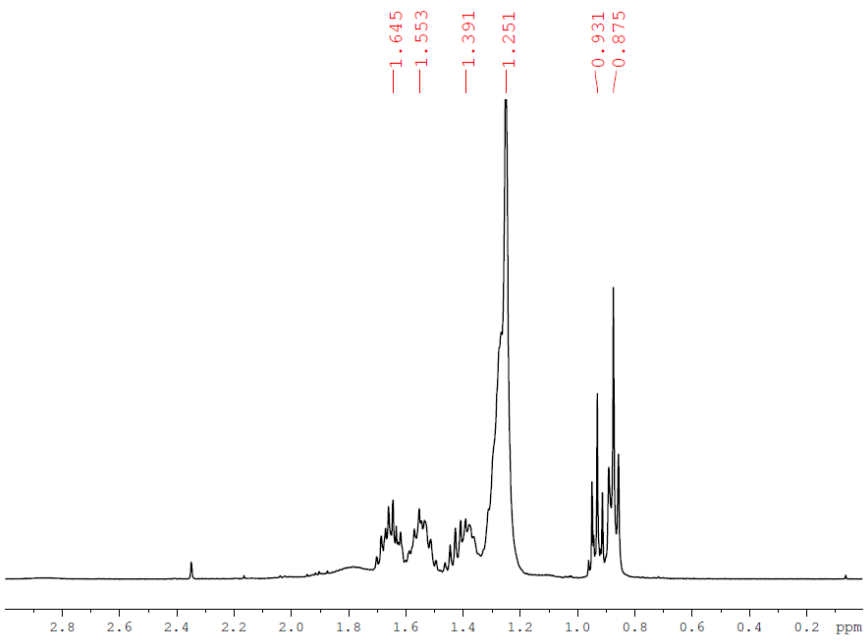

Figure 3.10 Ultrasmall CdSe QDs in $CDCl_3$ ^{1}H NMR. Labeled peaks are from the aliphatic protons on the carbon chains of the TOPO, HDA, and DDPA ligands.

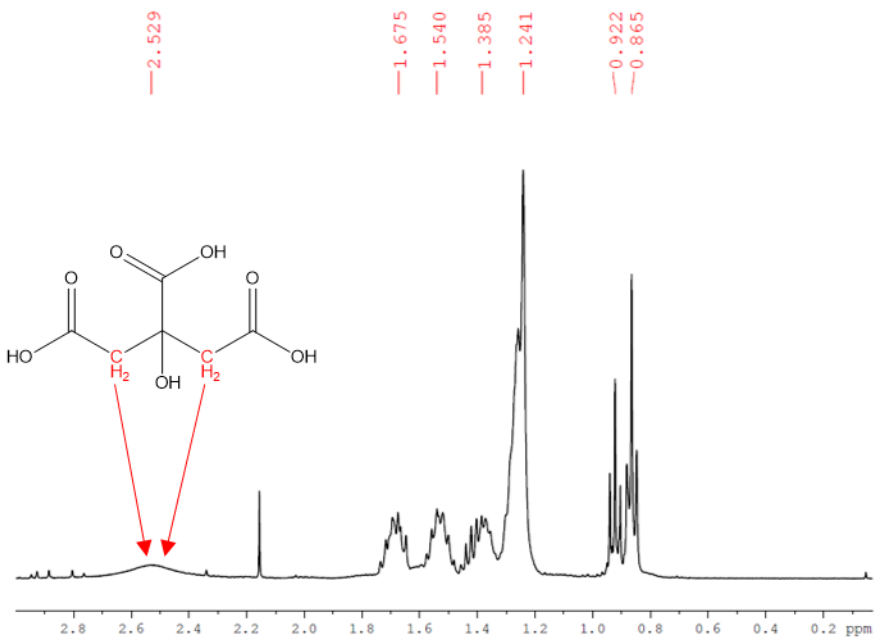

Figure 3.11 Ultrasmall CdSe-CA QDs in $CDCl_3$ ^1H NMR. Labeled peaks are from the aliphatic protons on the carbon chains of the TOPO, HDA, and DDPA and citric acid ligands.

3.2.3 BP-PFCB Films

In the previous studies, formic acid treated CdSe quantum dots have been observed to be unstable, as the formic acid is loosely bound to the surface of the quantum dots. This is seen in the instability and quenching of the fluorescence of the quantum dot solutions after a few weeks' time. This is also detected in the IR spectra with the broad O-H peak of a free formic acid ligand visible in the CdSe-FA solutions. To protect the formic acid treated CdSe quantum dots from ligand dissociation, they were encapsulated in a thermoplastic fluoro-carbon chain biphenylperfluorocyclobutyl (BP-PFCB) polymer from Tetramer Technologies, LLC. This polymer was previously studied by Schreuder, *et al.* and found to retain the absorption and emission spectra of the ultrasmall CdSe quantum dots, by achieving a monodisperse encapsulation. The lack of aggregation of the ultrasmall CdSe quantum dots is traced back to the

structure of the encapsulant. How well the quantum dots mixed with the encapsulant was determined by using the Hildebrand solubility parameter, which can be separated into three Hansen's solubility parameters (HSPs). HSPs relate the hydrogen bonding a=interaction, dipole-dipole, interactions, and the atomic/dispersive interactions. The more similar the HSPs, the more likely the solvent and the solute will mix. Toluene and mesitylene were used as representative values for the CdSe quantum dots and BP-PFCB, respectively. The Hildebrand solubility value for toluene is 18.2 and for mesitylene is 18.0, which are similar enough to mix well.

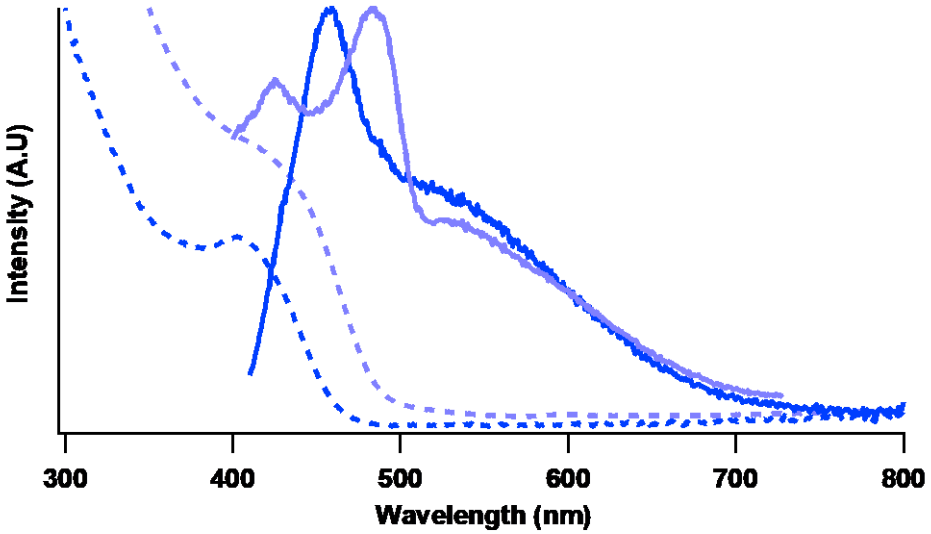

Figure 3.12 Absorbance (dashed) and photoluminescence (solid) of CdSe-FA quantum dots in toluene (blue) and BP-PFCB (light purple).

The absorption and emission spectra of the CdSe-FA quantum dots encapsulated in BP-PFCB at a weight percent of 9% is shown in Figure 3.12. Approximately 1 mL of the composite mixture was used to make the film shown in the inset. A shift and a broadening in the absorption spectra is seen due to an aggregation of the particles after encapsulation. The emission spectrum

for the encapsulated CdSe-FA quantum dots has changed in shape compared to that of the CdSe-FA in solution. The peak at 428 nm has unknown origins, while the first emission peak at 457 nm in the CdSe-FA is due to the pinned emission of the DDPA and the formic acid ligands. The peak at 485 nm in the BP-PFCB/CdSe-FA film is believed to arise from the same mechanism but has red-shifted due to aggregation of the quantum dots.

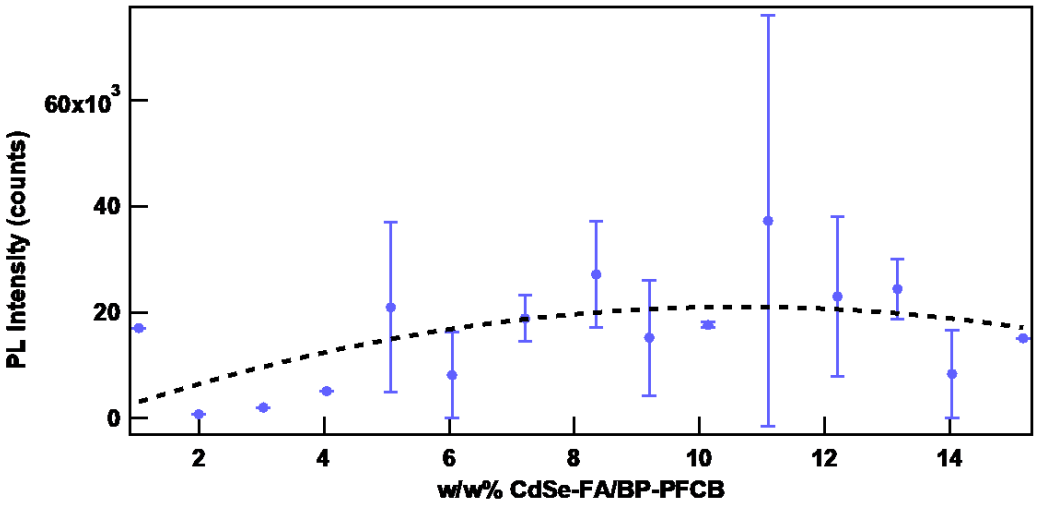

Figure 3.13 Emission intensity of CdSe-FA quantum dots in BP-PFCB vs percent by weight loading.

The effect of the quantum dot loading was studied using BP-PFCB as the encapsulant. Schreuder, *et al.* discovered that increasing the loading of ultrasmall CdSe quantum dots did not change the spectral shape but did have an effect on the emission intensity. Below 5% w/w loading, the intensity was linear, and then sharply increased until 9% w/w. After 9% w/w the increase did not have a significant effect on the intensity, which almost plateaued around 18% w/w.[56] For the CdSe-FA encapsulated in the BP-PFCB, the intensity linearly increased to around

11% w/w, then linearly decreased (Figure 3.13). There is a large amount of error in this data due to only three samples examined at each weight percent. The large amount of error can also be due to the thickness of the films. The emission intensity is also linearly dependent on the sample thickness. The volume of composite mixture used to make the films was 0.3mL, which did not make very thick films. White-light fluorescence images were obtained to show any aggregation occurring within the BP-PFCB/CdSe-FA films. It can be seen in the micrographs in Figure 3.14 that there is an increase in aggregation between the 10.07% and the 15.17% w/w loading, which leads to the decrease in emission intensity.

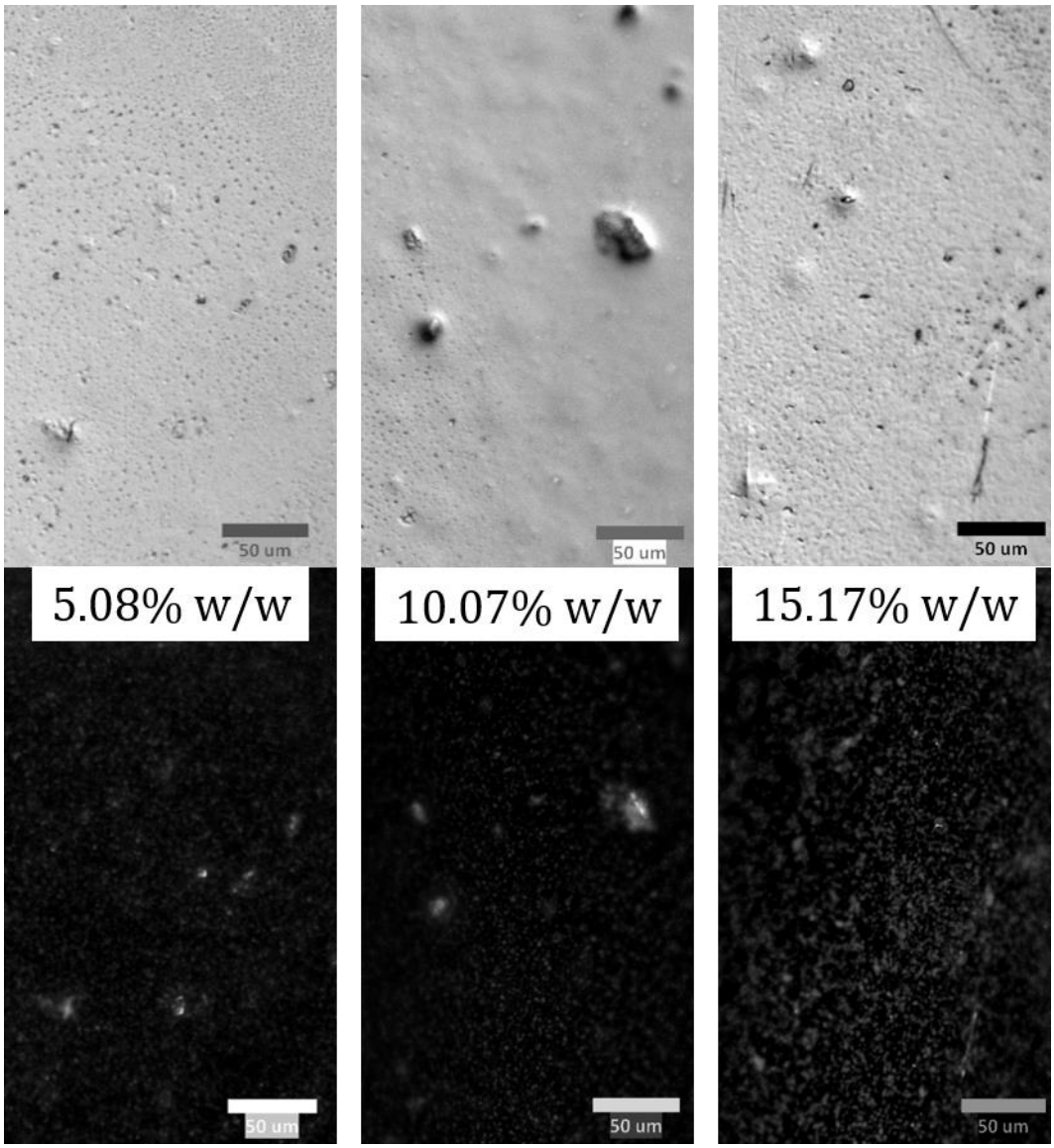

Figure 3.14 Representative bright field differential interference contrast (top) and white-light fluorescence micrographs of encapsulated CdSe-FA quantum dots at 5.08%, 10.07%, and 15.17% w/w loading in BP-PFCB. All images were acquired with an exposure time of 5 ms. The scale bars represent 50 μm on all the images.

3.3 Conclusions

Ultrasmall white-light CdSe quantum dots were treated with formic acid and citric acid. Both ligands increased the fluorescence intensity of the white-light emission, most prevalently in

the first emission peak, which presented with a cooler white-light now being observed. The as-synthesized ultrasmall CdSe quantum dots have an average quantum yield of 6% and CIE coordinates of (0.30, 0.34). With the formic acid treatment, the average quantum yield of the CdSe quantum dots increases to 21% and the CIE coordinates shift to (0.26, 0.30). The citric acid treated CdSe quantum dots have the highest reported quantum yield for a single component white-light emitter at 61%, with an average of 33%. The CIE coordinates of the CdSe-CA quantum dots are now (0.24, 0.22), a cool white-light emission. The increase in the quantum yield of the citric acid treated CdSe quantum dots is believed to be due to the partial ligand exchange from DDPA ligands to citric acid ligands. As the process for the first emission peak in the as-synthesized ultrasmall CdSe is from the "pinning" effect of the phosphonic acid ligands, when fewer phosphonic acid ligands are bound to the surface of the quantum dot, this process is no longer available. The relaxation of the electron now reverts to band gap emission. Along with the higher enhancement in the fluorescence intensity with citric acid compared to formic acid, the citric acid treated CdSe quantum dots show an increase in stability in solution. After 25 days, the fluorescence of the formic acid treated CdSe quantum dots has completely quenched. The citric acid treated CdSe quantum only showed a decrease in quantum yield from 36% to 31% in this time.

To corroborate that the ligand treatments were successful, IR and NMR spectroscopy were performed. The IR spectra for both the formic acid and citric acid treated CdSe quantum dots had peaks characteristic of the ligands used in the CdSe synthesis as well as peaks for the carboxylic acids. The IR spectra of the formic acid treated CdSe quantum dots, still had a broad O-H peak present, which is indicative of the free ligand being present in the solution. This is in-line with the oxidation of the formic acid treated CdSe quantum dots as the formic acid becomes

unbound from the surface of the quantum dot. The citric acid, which has three carboxylic acid groups that can bind to the surface of the quantum dot, does not appear to show the broad O-H peak, indicating that the ligand can bind to the surface by multiple carboxylic acid groups at once, leading to the higher stability. The NMR spectra of the citric acid treated CdSe quantum dots is difficult to use to identify the binding of the ligand to the surface of the quantum dot due to all of the ligands used in the synthesis having aliphatic hydrogens that have similar chemical shifts.

Since the formic acid treated CdSe quantum dots have a limited stability in solution, an encapsulation method needed to be employed to protect the quantum dots. It was found that in fabricating films from 1% to 15% w/w loading of CdSe-FA in BP-PFCB, the fluorescence intensity had a maximum at 11% w/w loading. In a film at 9% w/w loading, it was observed that the emission was red-shifted compared to the emission of the quantum dots in solution. This is due to the aggregation of the quantum dots in the polymer. This aggregation is evident in fluorescence microscopy micrographs with increasing loading percent.

CHAPTER IV

IN SITU MATERIAL STATE MONITORING USING EMBEDDED CDSE QUANTUM DOTS

4.1 Introduction

The development of new, smart materials that are capable of detecting, communicating and localizing damage is pivotal in the advancement and continued development of future mechanical, civil and aerospace systems and structures. There has been progress in research related to self-healing materials to help restore a material to its original strength after the application of damaging loads. Many self-healing systems lack the ability to communicate the occurrence of degradation within the materials, which prevents the corrective actions that must be taken to reinforce the weakened material. To prevent the degradation of a material, researchers must first be able to easily and quickly identify the material state. This capability could further extend into the manufacturing process for monitoring the material state intrinsically, especially precursors of degradation at the time of manufacturing and in the early life of structural components.

The overall goal of this project was to create a new structural health monitoring system to eliminate the need for powered, physical sensors by implementing ultrasmall CdSe white-light emitting quantum dots to probe and communicate stress in composite materials. The ultrasmall CdSe quantum dots are dispersed throughout polymer samples for damage detection applications. It is thought that changes in the material state can easily be identified by monitoring shifts or quenching in the emission spectra for these samples before and after the application of external loads (Figure 4.1) As external loads are applied to the material, the ligands responsible for the broad emission will be removed from the surface of the quantum dots, causing the change

in the emission spectra. By monitoring this change, an approach for determining the level of external forces acting on a system can be developed. Instead of altering the physical makeup of the material structure, the CdSe quantum dots are dispersed and mixed throughout the matrix of the composite material to minimize any impact on the original material strength properties.

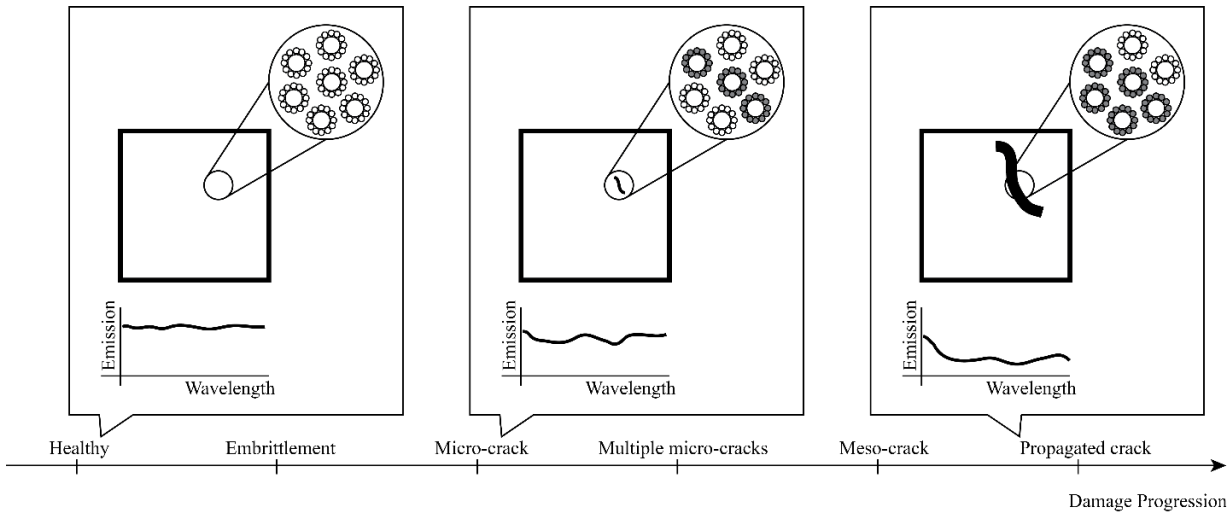

Figure 4.1 Proposed approach for damage detection using CdSe quantum dots.

In this work, epoxy samples containing varying percent weight of CdSe quantum dots are fabricated and experiments are performed to evaluate changes in the emission spectra before and after the application of external loads. By monitoring the transformations in the emission spectra with application of external loads, the use of CdSe quantum dots for communicating the occurrence of external loads is evaluated.

4.2 Results and Discussion

4.2.1 Cylindrical and Thin Disc Epoxy Loading Studies

Initially, ultrasmall CdSe quantum dots were synthesized as reported in Chapter 2 and purified via gel permeation chromatography. The resin and hardener components of the Aptek Labs two-part epoxy are mixed and the CdSe quantum dots in toluene are added to the mixture. After thorough mixing and degassing to remove any air bubbles, the mixture is poured into cylindrical molds and placed in an oven to cure at 80 °C overnight. Figure 4.2 shows the baseline emission spectra for a cylindrical epoxy sample with 1% w/w of quantum dots prior to the application of external loads. Although, the emission spectra of the epoxy samples are found to be less distinct that of the quantum dots in solution, the three emission peaks are still present after encapsulation.[57]

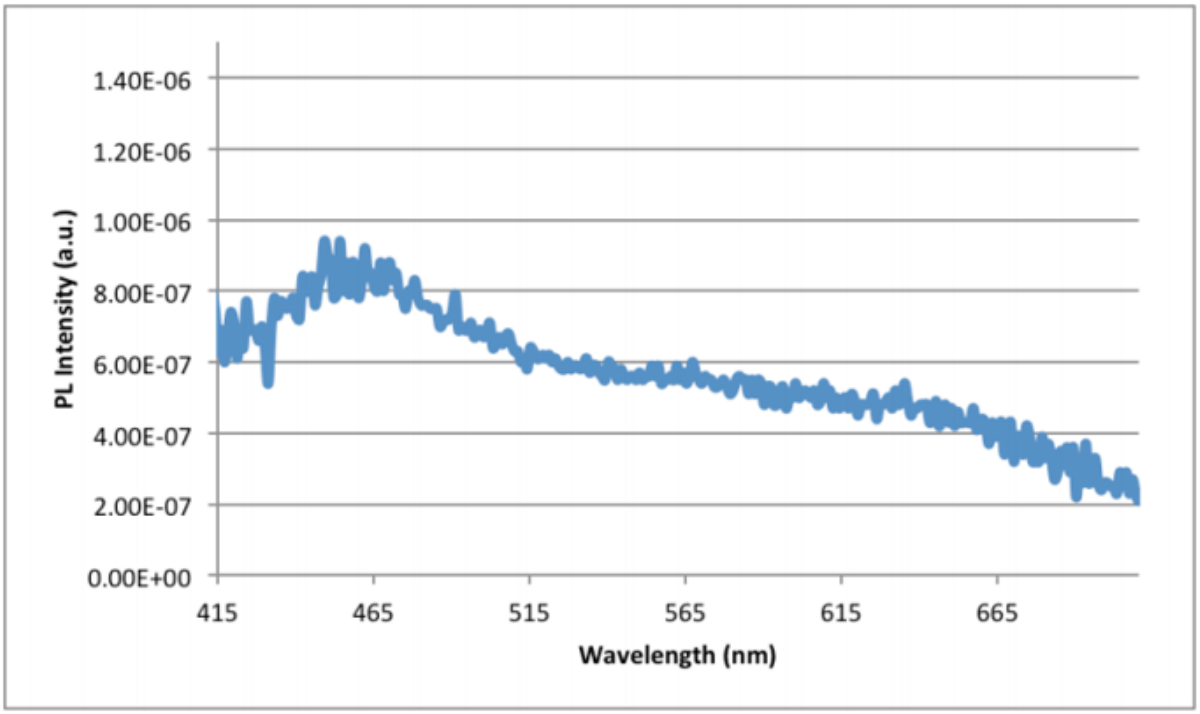

Figure 4.2 1% w/w CdSe and epoxy baseline (unloaded) emission spectra.

The cylindrical epoxy/CdSe samples were loaded in compression using a Tinius-Olsen press to various levels of force (500, 1000, and 1500 lbs). The samples were not constrained in any direction and were allowed to deform under the application of external loads. The emission spectra were for the samples were obtained using a Labsphere SLMS-LED-1050 integrating light sphere system, fiber coupled to a CDS 600 CCD-base spectrophotometer and accompanying software (Figure 4.3).

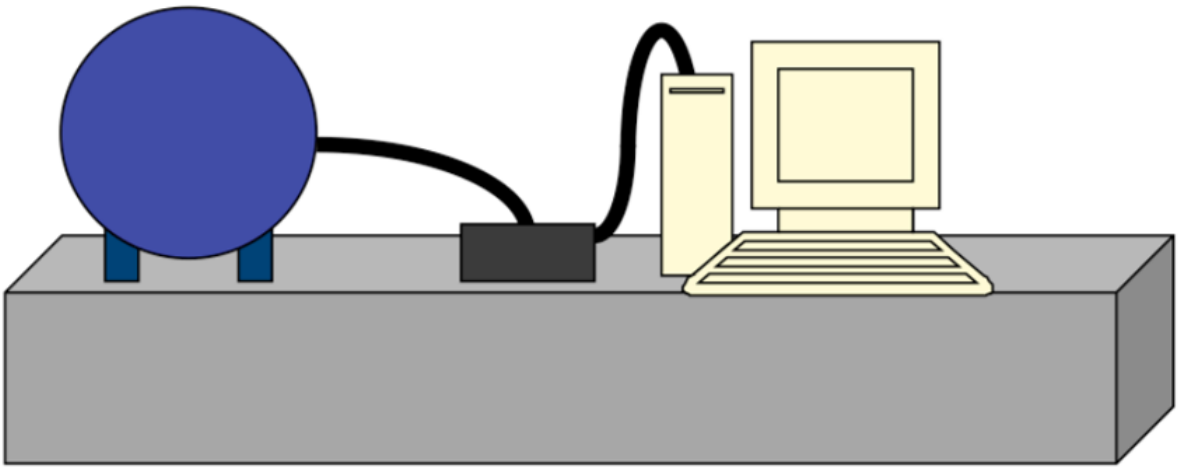

Figure 4.3 Schematic illustration of integrating sphere system.

It was found that the emission spectra did not continuously decrease with increasing external loads as theorized (Figure 4.4).[57] Furthermore, the change in emission spectra does not demonstrate a monotonic trend across the entire spectrum being analyzed. During the experiment, samples were observed to plastically deform when loaded to 1000 and 1500 lbs, and the shape of the sample is altered (Figure 4.5) The sample was observed to decrease in height and increase in cross-sectional area with increasing loads, changing from a pure cylinder to a

barrel-like shape. It is hypothesized that this change in shape and corresponding change in cross-sectional area contributed to the observed response displayed.

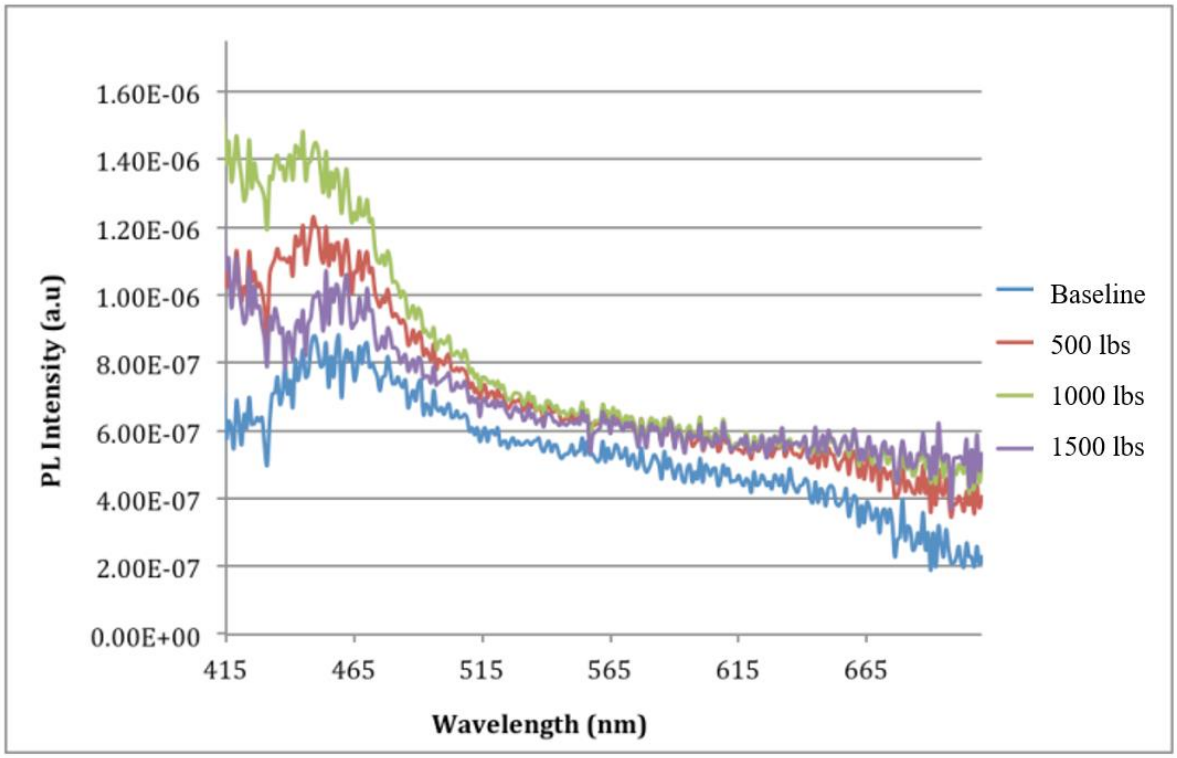

Figure 4.4 Cylindrical sample baseline (unloaded) and loaded emission spectra.

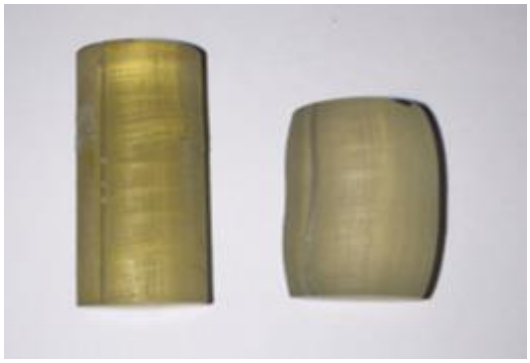

Figure 4.5 Unloaded (left) and loaded (right) epoxy/CdSe sample.

During testing, the samples were supported on a stage inside the light sphere and excited with the laser at approximately the midpoint of the sample height. The stage height was selected based on the unloaded baseline sample and was used for all subsequent measurements. To account for any non-uniformities on the surface of each sample, a total of five measurements were averaged to obtain the sample emission spectra. As the samples were loaded, and their cross-sectional areas increased, it is believed that the laser excitation source was exciting a larger number of CdSe quantum dots, thus causing the overall emission spectra to increase. This holds true as when the samples were loaded to 500 and 100 lbs prior to the noticeable inflection point in the data near 615 nm. The emission spectra for the sample loaded to 1500 lbs is believed to be lower than the other samples because the stage height was not changed during the experiment, and the sample showed a considerable decrease in height when compared to the unloaded sample. As a result, the laser was no longer exciting along the midpoint of the sample, and fewer CdSe quantum dots were excited, causing a lower observed emission spectrum.

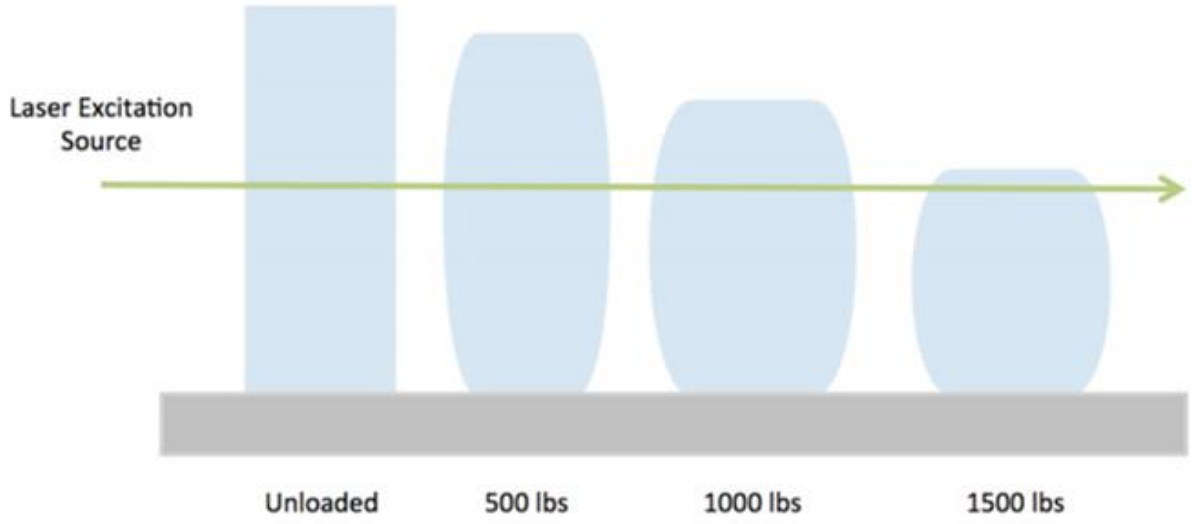

Figure 4.6 Schematic representation of laser excitation of the epoxy/CdSe samples.

Beyond approximately 615 nm, the observed emission spectra changes, and a continuous increase in the emission spectra with the application of external loads is observed. There are two possible explanations for this phenomenon. These are an increase in surface defects on the surface of the quantum dots or an overall increase in light scattering. Since the emission spectra is highly dependent on the surface defects, when external loads are applied to the cylindrical samples, it is possible that the surface of the CdSe quantum dots is alter, and addition surface defects are formed. The formation of these new surface defects would cause an increase in the observed emission spectra. An increase in light scattering could occur due to the formation of micro-cracks throughout the epoxy sample.

To mitigate the problem of the change in sample height during external loading, thin disc samples were fabricated.[58] These sample were loaded on the Tinius-Olsen press at 250 lbs increments, up to a maximum load of 1250 lbs. Once again, the samples were loaded along their axis, and were not constrained in the lateral direction. To minimize the impact that material deformation has been observed to have on the recorded emission spectra, samples were loaded within the elastic range of the epoxy matrix.

Samples were first studied using a fluorescence microscope to obtain a baseline, undamaged image of the epoxy/CdSe material. Baseline emission spectra was then collected using the light sphere. After baseline microscopy and emission data had been recorded, samples were loaded in compression at 250 lb increments, were the above procedure was repeated for each load case.

Results for the thin disc epoxy samples containing 2% w/w CdSe quantum dots tested in compression with a comparison between the baseline (unloaded) emission and recorded emission

spectra at various levels of increasing external load over the spectral range from 410-800 nm. (Figure 4.7) Furthermore, to better visualize the observed decreases in emission spectra for the samples, the collected emission data was also plotted using an "integral" approach (Figure 4.8). Here, the photoluminescence intensities for individual cases were summed over the entire spectral range being studied, normalized with respect to the maximum value for each sample and plotted against the load. These plots represent the relative changes in the observed emission between load cases and help provide a better understanding of how the ultrasmall white-light emitting CdSe quantum dots behave in response to external loadings.

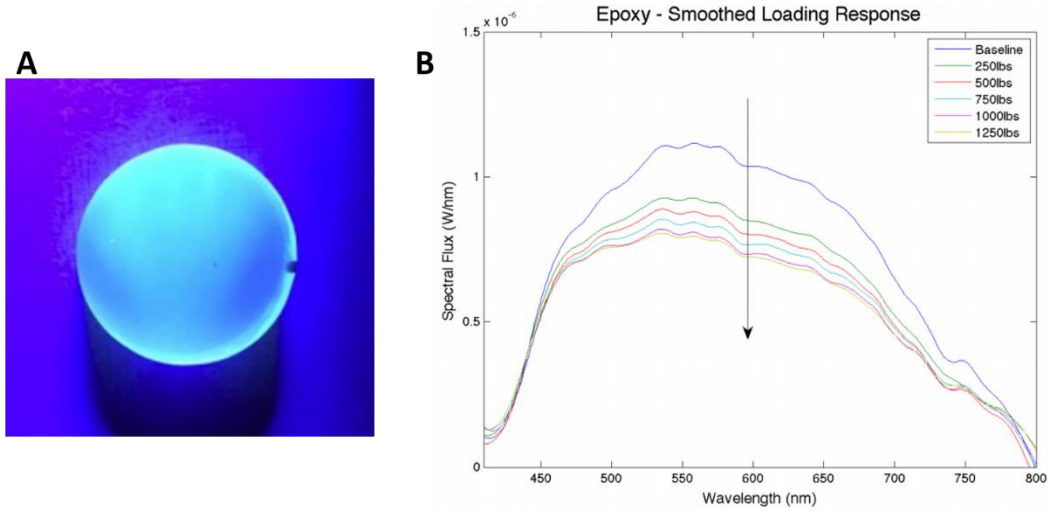

Figure 4.7 A) Thin disc sample under UV excitation. B) Response of epoxy/CdSe samples under increasing compressive loads.

For the thin disc epoxy/CdSe samples loaded in compression, a monotonic decrease in the recorded emission spectra is observed. These results align with the initial hypothesis that the application of external loads causes the removal of surface bound ligands present on CdSe quantum dots, thus leading to a decrease in the observed emission spectra for each sample.

Analyzing the “integral” plot for this emission data (Figure 4.8), it was observed that the decrease in emission was not linear with the application of external load. In fact, the largest decrease in emission (15% relative to the baseline) occurred after the initial load has been applied to the system (baseline to 250 lbs) and the relative change in emission between individual load states tended to decrease at higher loading increments. Once the sample was loaded from 1000 lbs to 1250 lbs, there was almost no change in the observed emission between load cases. It is believed that there will be a maximum load at which the observed emission spectra between load cases will begin to “plateau” and remain unchanged. At this point, CdSe quantum dots will no longer be able to communicate the occurrence of external loads acting on the material beyond this point, as evidenced here at 1000 lbs and 1250 lbs.

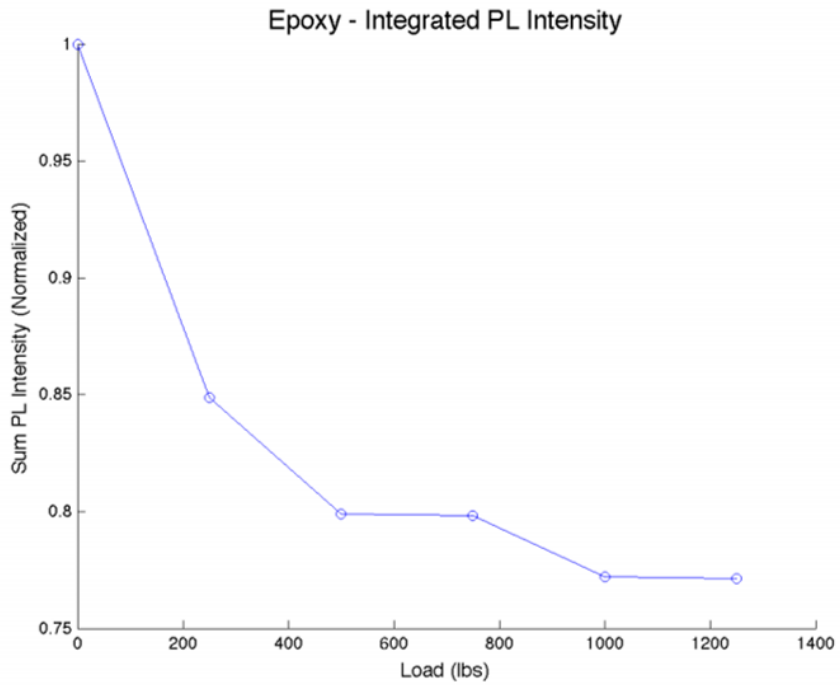

Figure 4.8 “Integral” emission curve for epoxy/CdSe thin disc samples.

4.2.2 Surface Coated Epoxy Loading Studies

Tensile specimens were fabricated by drop casting a thin layer of epoxy containing 1% w/w of CdSe quantum dots onto aluminum and fiberglass tensile samples (Figure 4.9).[58] The same procedure used to fabricate thin disc compressive samples was used to obtain a mixture of epoxy and CdSe quantum dots with the desired % weight of quantum dots.

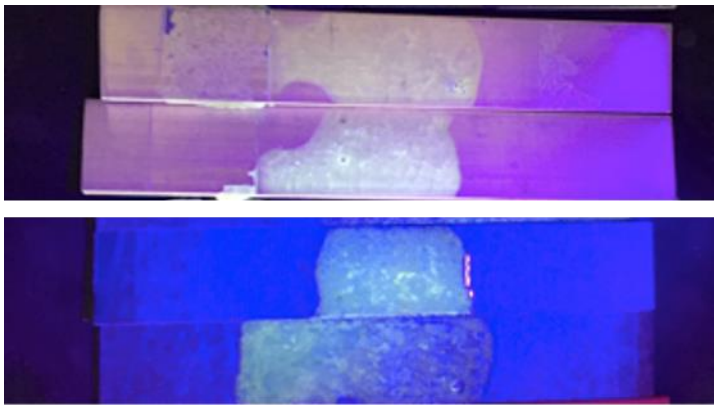

Figure 4.9 Epoxy/CdSe surface coated aluminum (top) and fiberglass tensile samples under UV excitation.

The tensile samples were loaded in uniaxial tension using an MTS 810 tensile testing machine at increasing levels of load, up to a maximum load of 1000 lbs. Samples were loaded in tension at a rate of 5 lbs/sec and the load was allowed to stabilize for 60 seconds (within 5 lbs of the specified loading) at each step before the emission data was recorded. During testing, samples were again only loaded in the elastic range. Unlike the compressive testing, the emission data for the tensile samples were recorded ‘in situ” under the application of external loads without the use of the integrating sphere setup, in an attempt to better observe the response of CdSe quantum dots.

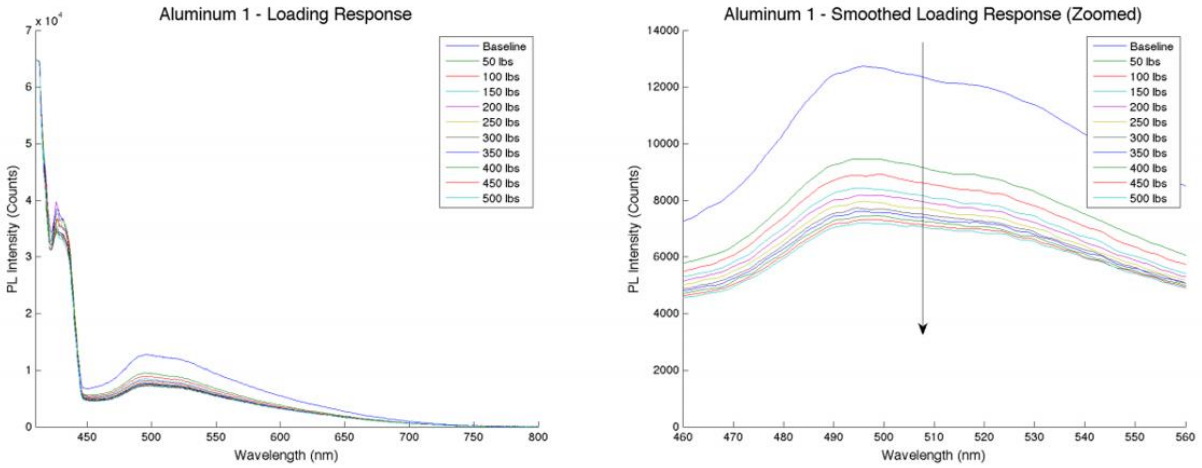

Figure 4.10 Response of epoxy/CdSe surface coated aluminum samples under increasing tensile loads. The full spectrum (left) and a focus on the wavelengths 460 to 560 nm(right).

Similar to the thin disc samples loaded in compression, epoxy/CdSe surface coated aluminum samples loaded in tension displayed a monotonic decrease in emission for all samples tested (Figure 4.10). These results again initially appear to support the hypothesis that the application of external loads results in the removal of surface ligands present on CdSe quantum dots, ultimately quenching the emission. Comparing the "integral" emission plots for all samples, the overall behavior of the epoxy/CdSe aluminum surface coating can be compared. Similar to the results obtained for the thin disc samples loaded in compression, the largest decrease in the recorded emission data again occurred at the first loading increment (baseline to 50 lbs). Here the overall emission relative to baseline was decreased by 18% for the first load increment. For subsequent loading cases, the observed decrease in emission spectra showed a nearly linear trend

with increasing external loads for all samples, unlike the behavior observed for samples loaded in compression. Though the recorded emission did not plateau in these experiments, it is believed that the surface coating will also have a maximum load sensitivity, and ultimately reach a point at which the application of additional load will not cause a continued decrease in emission.

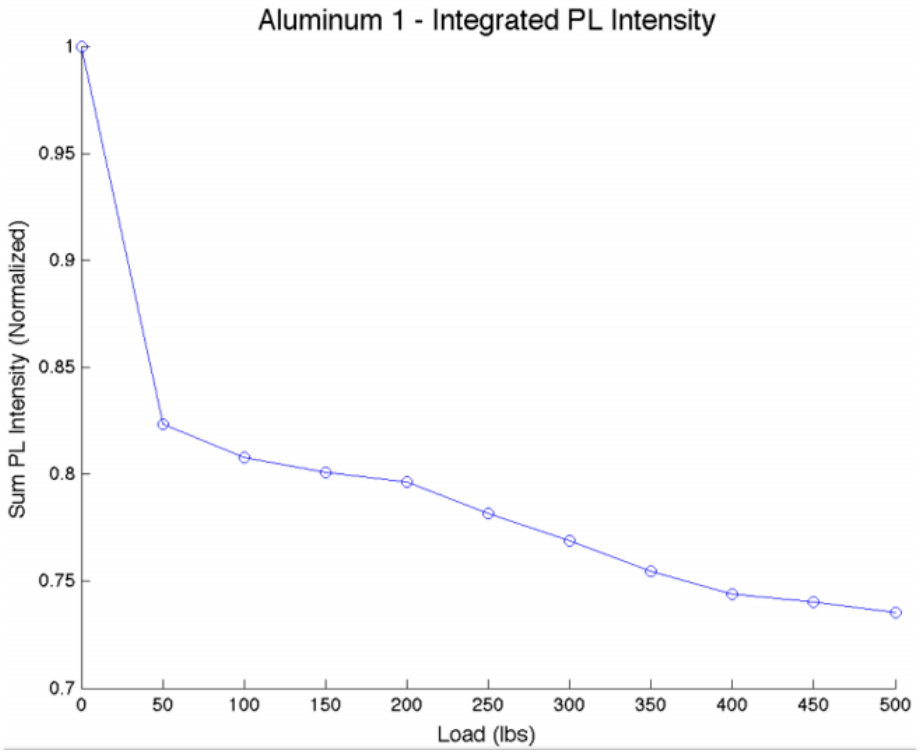

Figure 4.11 "Integral" emission curve of an epoxy/CdSe surface coated aluminum sample.

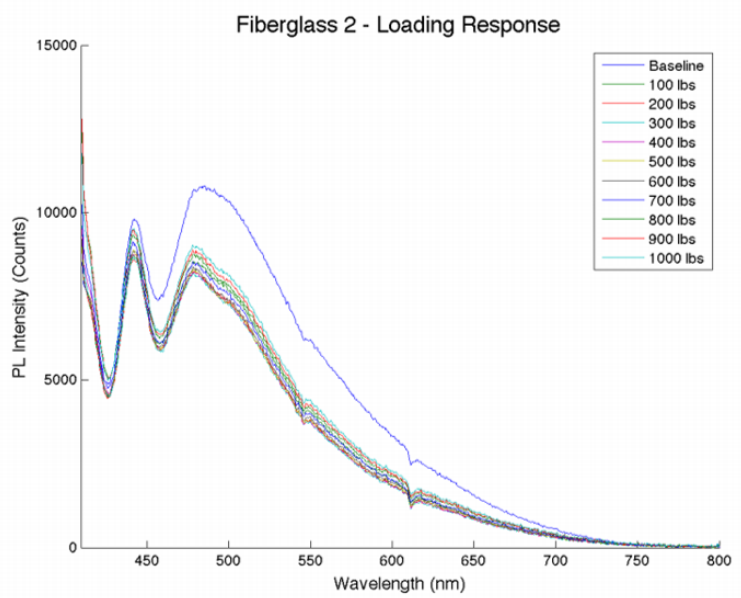

Figure 4.12 Response of epoxy/CdSe surface coated fiberglass samples under increasing tensile loads.

The results for the fiberglass sample coated with epoxy/CdSe did not follow the observed trends for either surface coated aluminum tensile samples or the thin disc epoxy/CdSe samples. Rather, the emission spectra for surface coated fiberglass samples tended to decrease initially and subsequently increase in response to the application of external loads, deviating from the initial idea presented earlier. The biphasic trend can be observed with the "integral" emission plot for the samples tested (Figure 4.13). Though the overall emission trend deviated slightly from sample to sample, the largest change in emission for each surface coated fiberglass sample occurred after the application of the initial load (baseline to 100 lbs), similar to the results obtained for both thin disc compressive and aluminum tensile test samples. For this initial load step, the emission decreased by 26% relative to the baseline, which is relatively similar in magnitude to the initial decrease in emission observed in the other tests performed in this study. At around 300-400 lbs, though, is where the biphasic behavior of the epoxy/CdSe coated

fiberglass samples begins to become apparent, as the recorded emission spectra starts to increase with the application of larger external loads. The mechanism behind this observed behavior is uncertain, but it is believed to be caused by the composite nature of the fiberglass material. It is believed that the epoxy/CdSe surface coating was able to soak into the bulk of the fiberglass, and fill some of the microscopic voids present between individual fibers during the cure process. When samples were loaded, distinct cracking and popping noises were audible from the fiberglass samples at loads above 200-250 lbs, where individual fibers were being broken. Due to the presence of epoxy/CdSe below the surface of the fiberglass, it is thought that the breaking of individual fiber exposed more CdSe quantum dots at loads above 300-400 lbs and ultimately resulted in the increase in emission observed for the samples beyond these loads.

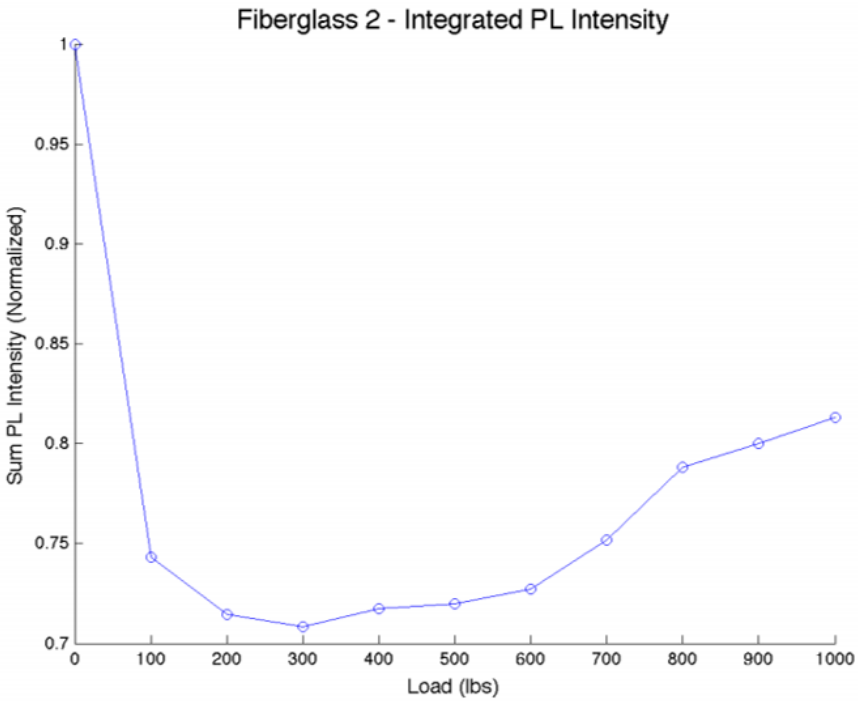

Figure 4.13 "Integral" emission curve of epoxy/CdSe surface coated fiberglass samples.

A final set of experiments were performed to evaluate the temporal response of the epoxy/CdSe surface coated samples. For these experiments, aluminum and fiberglass samples were loaded to 500 lbs, at which the load was held constant, and the emission was recorded at five-minute intervals. A total of four measurements were made over a time period of 15 minutes (0 min, 5 min, 10 min, and 15 min), representative of the total time required to perform the tensile experiments used to collect the data discussed above. During these experiments, the laser excitation source was left on throughout the duration of the experiment. The temporal results for both epoxy/CdSe surface coated aluminum and fiberglass samples are shown in Figures 4.14 and 4.15. As can be seen from the "integral" curves for both samples, the overall emission tends to decrease over time under a constant load. After 15 minutes of exposure, the emission had decreased by 9% and 16% relative to the baseline for the aluminum and fiberglass samples, respectively. This decrease in emission indicates that the CdSe quantum dots are being photobleached in the presence of the laser excitation source. Though the overall decrease in emission due to photobleaching is smaller when compared to the observed decreases in emission relative to the baseline for loaded samples (i.e. 25-70% and 25-30% for aluminum and fiberglass respectively), the photobleaching effects of CdSe quantum dots in the presence of a laser excitation source will be crucial in further understanding the exact response of CdSe in response to the application of external loads.

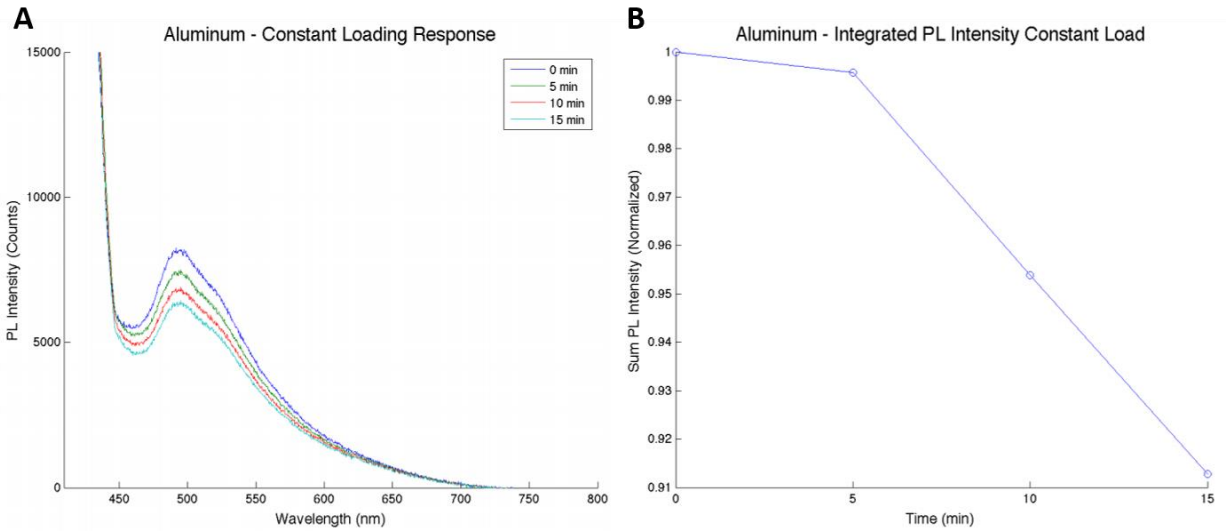

Figure 4.14 A) Temporal response of epoxy/CdSe surface coating on aluminum samples under constant load. B) "Integral" emission curve for temporal response of aluminum samples.

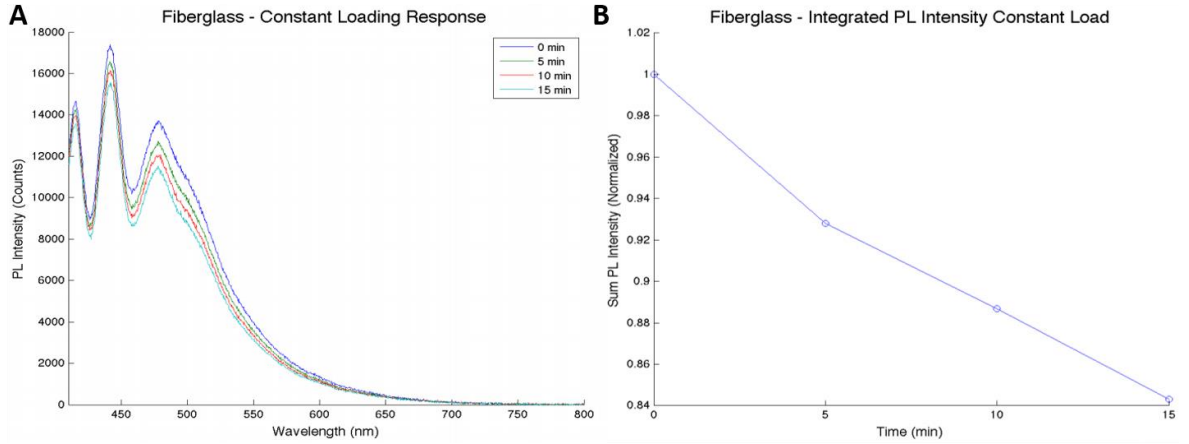

Figure 4.15 A) Temporal response of epoxy/CdSe surface coating on fiberglass samples under constant load. B) "Integral" emission curve for temporal response of fiberglass samples.

4.3 Conclusions

In this work, the effectiveness of ultrasmall white-light emitting CdSe quantum dots for damage detection applications was evaluated. Results for the response of CdSe quantum dots tested in both compression and tension are presented here and suggest the potential use of CdSe quantum dots for a variety of load sensing applications. By monitoring distinct quenching in the emission spectra for composite epoxy samples and surface coated aluminum and fiberglass tensile samples containing CdSe quantum dots, the application of external loads to the sample were able to be detected and monitored. It is believed that this decrease in emission observed for increasing levels of external load is due to the removal of surface ligands present on CdSe quantum dots. In all samples evaluated, both in compression and tension, the largest decrease in emission was observed at the first load increment. Beyond the first load case, though, samples had varied responses to the application of external loads. For surface coated fiberglass samples, a biphasic response was observed where the emission tended to decrease with the application of external loads until a load of 300-400 lbs was reached where the emission began to increase. At this point, it is thought that the deformation and breaking of individual fibers, and composite nature of the fiberglass material, resulted in the exposure of additional CdSe quantum dots, causing an increase in the observed emission at these higher loads. Finally, the temporal response of CdSe quantum dots was evaluated to observe the effects of photobleaching on the recorded emission spectra. Over a period of 15 minutes, the emission spectra for epoxy/CdSe surface coated aluminum and fiberglass samples was observed to decrease in a nearly linear manner. In order to minimize the effects of photobleaching on the recorded emission spectra for loaded samples, the laser excitation source could be turned off between load cases in future testing and only allowed to illuminate the sample when emission data is being recorded. In all, the use of

CdSe quantum dots presents a promising alternative to detecting and communicating the occurrence of external loads acting on a material by monitoring distinct decreases in the unique emission spectra given off by ultrasmall white-light emitting CdSe quantum dots.

CHAPTER V

INCORPORATION OF CDSSE QUANTUM DOTS FOR 3D PRINTING AND ADDITIVE MANUFACTURING APPLICATIONS

5.1 Introduction

With the ability to minimize material waste while simultaneously shorten production times, many industry experts have dubbed additive manufacturing and 3D printing related technologies as the fourth industrial revolution – Industry 4.0 – due to its highly disruptive nature in the manufacturing sector. In order to accelerate product development and minimize manufacturing and production costs, additive manufacturing is being used to 3D print a myriad of parts and components for a wide range of products with complex shapes in applications including aircrafts, automobiles, and biomedical implants.[78,79] Using a layer-by-layer approach, additive manufacturing technologies are typically classified according to the method of deposition and range of compatible materials.[79–81] Material extrusion, powder bed fusion, binder jetting, sheet lamination and vat polymerization are various examples of additive manufacturing approaches currently being used.[81] By utilizing compatible materials including polymers, plastics, metals, ceramics, organic materials and even living cells, a range of products have been fabricated for airplanes and automobiles,[82] manufacturing tooling,[83] electronics,[84] medical devices,[85] and prosthetics.[86] Though each approach has its own set of advantages and drawbacks, fused deposition modeling (FDM), a form of material extrusion, has emerged as one of the most prominent and popular forms of additive manufacturing techniques. The relative affordability of FDM systems, combined with the ease of materials processing and ability to rapidly manufacture functional structures and components, has helped drive the continued demand for FDM related

systems and technologies.[87] Similar to other processes where parts and components are 'built up' in a layer-by-layer fashion, FDM utilizes a thermoplastic feedstock to produce the desired part or structure. Here, a polymer-based filament is fed through a nozzle after being heated above its melting temperature and the subsequent molten plastic is deposited onto a build plate. With each layer of material deposited, the printer's build plate is sequentially lowered as the nozzle travels in a predetermined path following the part geometry to manufacture the final structure.

Through materials process and design considerations, the development of new polymer-based materials compatible with material extrusion-based systems has been a recent area of focus in the advancement of FDM technologies. Namely, there has been increasing interest in the development of 'functionalized' materials for additive manufacturing applications. In order to accomplish this goal, researchers have explored the use of various additives and polymer design/modification to enable 3D-printed materials and structures with a wide range of unique material behaviors and responses. One particular area of research that is gaining tremendous interest is the incorporation of nanomaterials within additive manufacturing processes. On the length scale of approximately 1–100 nm, the incorporation of nanomaterials within 3D printing processes can enable a number of new and customizable material behaviors including enhanced material strength properties[88], increased chemical durability[89], and advanced optical responses[90], among many others. Through the proper selection of the nanomaterial system and host matrix, it is possible to create an assortment of functionalized nanocomposite systems and materials compatible with additive manufacturing and FDM type processes and applications.

To date, researchers have demonstrated the ability to incorporate a range of organic[91] and inorganic nanomaterial systems including graphene[92,93], metallic nanoparticles[94,95], and carbon nanotubes[96], among many others, within the additive manufacturing process. Traditionally, these

nanofunctionalized systems are obtained through melt- or solution-mixing processes and extruded to obtain filament compatible with traditional 3D printing systems.

The goal of this project was to develop a functional material compatible with 3D printing applications for the continued advancement and adoption of additive manufacturing technologies. Here the ability to incorporate cadmium sulfur selenide graded alloy quantum dots (CdSSe) directly within a polylactic acid (PLA) host matrix to obtain nanofunctionalized, fluorescent filament compatible with stock 3D printing systems. Many tests and material characterizations are performed to reveal the overall effects that functionalization has on the properties of the embedded quantum dots and polymer host matrix as well as the mechanisms that control these effects. To demonstrate the ability to additively manufacture components exhibiting new material behaviors, light pipes and fluorescent devices are printed using an FDM approach by harnessing the optical response of embedded CdSSe graded alloy quantum dots within the 3D printing process. The development of quantum dot-functionalized 3D printer filament represents a unique opportunity for the advancement and design of new materials compatible with additive manufacturing processes and applications.

5.2 Results and Discussion

5.2.1 Thin Film Characterization

CdSSe graded alloy quantum dots were synthesis as reported in Chapter 2. Through TEM measurements, these quantum dots had a diameter of 5.7 ± 1.0 nm (Figure 5.1 C).[59] These quantum dots displayed an average quantum yield of 54% with a band-edge absorbance peak near 569 nm and a maximum photoluminescence emission intensity at 593 nm in solution (Figure 5.2). Polylactic acid, which is a thermoplastic polymer, was selected as the host matrix to produce functionalized filament due to its ease of material processing, minimal absorbance and emission across the visible spectra, mutual solubility with the quantum dots in solution, and overall compatibility with material extrusion and fused deposition modeling type 3D-printing systems.[97]

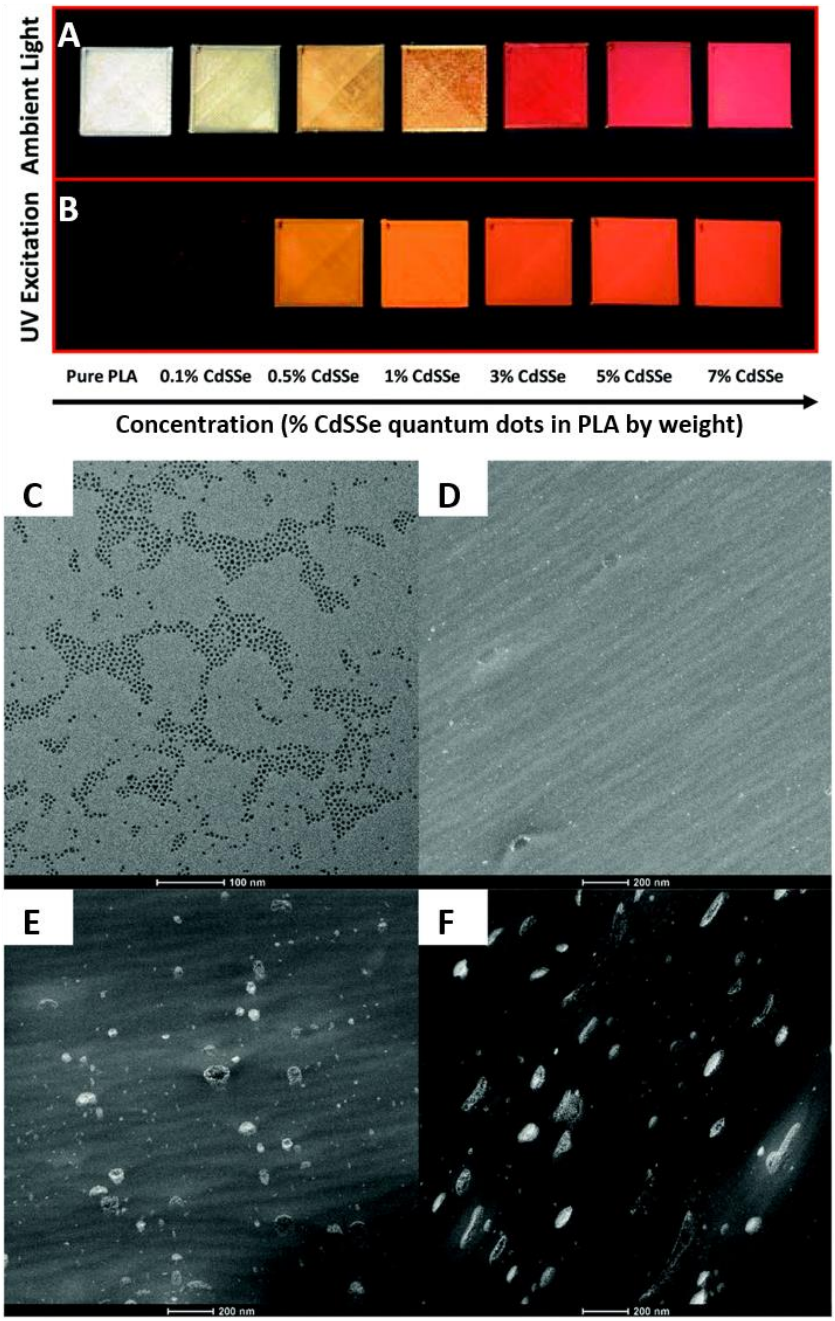

Figure 5.1 3D-printed pure PLA and PLA/CdSSe quantum dot films at varying concentrations of CdSSe quantum dots in PLA by weight under A) ambient light and B) UV excitation (picture was taken using a UV filter). Corresponding TEM image of C) CdSSe quantum dots drop cast from solution (approximately 5.7 ± 1.0 nm in diameter, scale bar 100 nm), high angle annular dark field (HAADF) STEM images of D) PLA/CdSSe quantum dot 3D-printed film (0.5% CdSSe QD in PLA by weight, scale bar 200 nm), (e) PLA/CdSSe QD 3D-printed film (3% CdSSe QD in PLA by weight, scale bar 200 nm), (f) PLA/CdSSe 3D-printed film (7% CdSSe QD in PLA by weight, scale bar 200 nm). Aggregation between individual quantum dots can be seen at increasing concentrations of CdSSe QDs in PLA.

Thin film samples, with a thickness of 0.5 mm, were fabricated to study the optical properties and characteristics of 3D-printed PLA/CdSSe quantum dots by varying the concentration by weight of the quantum dots in the PLA. When incorporated within the PLA, the absorbance behavior of CdSe quantum dots remained relatively unchanged, as both the overall spectra and absorbance peak location for 3D-printed films were consistent with CdSSe quantum dots in solution following materials processing and printing (Figure 5.2 A and B). Consistent with Beer-Lambert's Law for quantum dots in solution, 3D-printed PLA/CdSSe quantum dot films also displayed a linear relationship between absorbance intensity (Figure 2 C).

The photoluminescence emission properties of 3D-printed PLA/CdSSe quantum dot thin films were also evaluated. Though the overall monochromatic behavior of the CdSSe quantum dots in solution was maintained following printing, a significant red shift in the wavelength of maximum photoluminescence intensity was observed for increasing concentrations of CdSSe quantum dots in PLA (Figure 2 D and E). For the highest concentration studied (7% CdSSe in PLA by weight), the wavelength of maximum photoluminescence intensity was red-shifted by 32 nm relative to CdSSe quantum dots in solution. This spectral red-shift is attributed to a combination of two factors: quantum dot aggregation in the 3D-printed PLA/CdSSe films, and the presence of multiple sizes of quantum dots in the as-synthesized graded alloy CdSSe quantum dot solution enabling energy transfer from small to larger sized quantum dots in aggregated form.[98,99]

In order to quantify the degree to which quantum dot aggregation influenced the observed optical response, HAADF STEM images were obtained 3D-printed PLA/CdSSe quantum dot films. A direct relationship between aggregation and the recorded spectral shift is expected.[98] At low concentrations (0.5% CdSSe quantum dots in PLA by weight), minimal aggregation was

observed, and CdSSe quantum dots were well dispersed throughout the 3D-printed film (Figure 5.1 D). Relative to CdSSe quantum dots in solution, the wavelength for maximum photoluminescence emission was red-shifted by 4 nm for the 0.5% pLA/CdSSe quantum dot 3D-printed sample (Figure 5.2 E) At higher concentrations of CdSSe quantum dots in PLA (3% and 7% CdSSe quantum dots in PLA by weight), though, distinct aggregation between individual quantum dots within the 3D-printed films was confirmed (Figure 5.1 E and F). In these samples, embedded CdSSe quantum dots existed mainly in larger, aggregated clusters ranging in size from 49 ± 24 nm to 70 ± 54 nm, where the location of max photoluminescence intensity red-shifted 26 nm and 32 nm for 3% and 7% CdSSe quantum dots in PLA by weight, respectively.

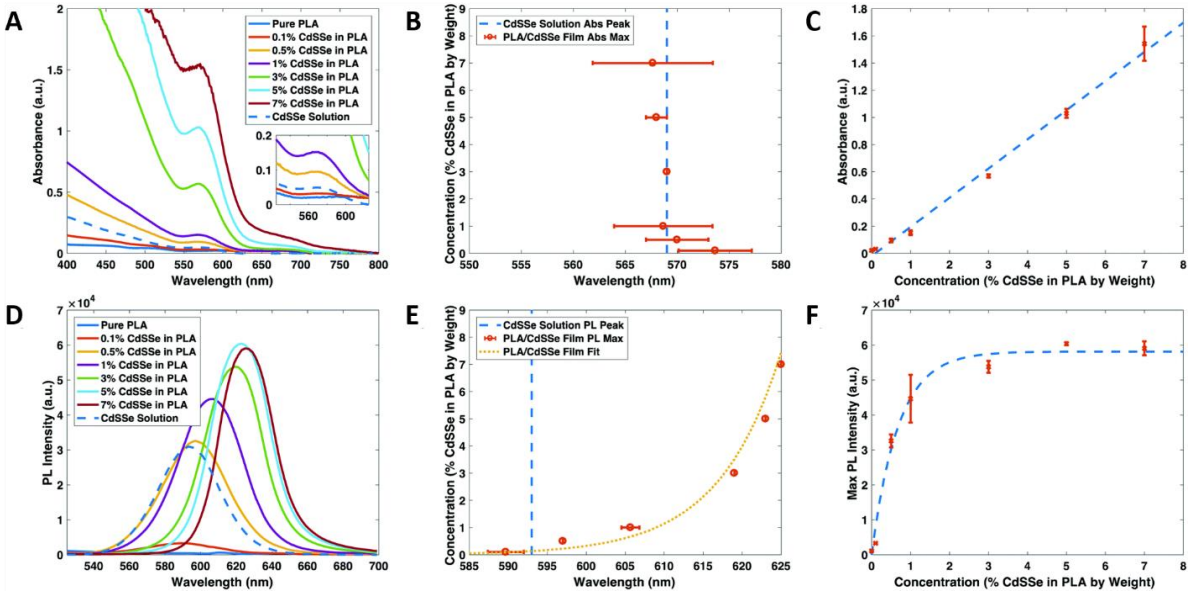

Figure 5.2 A) Average absorbance spectra of 3D-printed PLA/CdSSe quantum dot films at varying concentrations of CdSSe quantum dots in PLA by weight and CdSSe quantum dots in solution. B) Location of absorbance peak for 3D-printed PLA/CdSSe quantum dot films at varying concentrations of CdSSe quantum dots in PLA by weight. C) Relationship between absorbance intensity (measured at absorbance peak for CdSSe QDs in solution, 569 nm) and concentration of CdSSe QDs in PLA by weight. (d) Average photoluminescence spectra of 3D-printed PLA/CdSSe QD films at varying concentrations of CdSSe QDs in PLA by weight and CdSSe QDs in solution. (e) Location of maximum photoluminescence for 3D-printed PLA/CdSSe QD films at varying concentrations of CdSSe QDs in PLA by weight. (f) Relationship between maximum photoluminescence intensity and concentration of CdSSe QDs in PLA by weight.

With increasing concentrations of embedded quantum dots and the resultant aggregation in 3D-printed PLA/CdSSe quantum dot films, energy transfer between the multiple size population in as-synthesized CdSSe quantum dots is expected to drive the observed spectral red-shift (Figure 5.2 D and E). This energy transfer, and corresponding reabsorption, is displayed by a narrowing of the full width at half maximum of the photoluminescence emission spectra for increasing concentrations of CdSSe quantum dots in PLA. Here, the lower wavelength emission associated with smaller quantum dots in the nanofunctionalized composite decreases, as its

emission is reabsorbed by surrounding, larger CdSSe quantum dots, and the overall spectral response begins to be dominated by the higher wavelength component of the quantum dot emission (Figure 5.3). the spectral red-shift observed for 3D-printed PLA/CdSSe quantum dot films is expected to continue to plateau with increasing concentrations of quantum dots, as indicated by the trends obtained for the samples studied in this manuscript.

Similar to the observed spectral red-shift, the overall photoluminescence intensity of 3D-printed PLA/CdSSe quantum dot films was also found to the be concentration dependent. The photoluminescence intensity is found to plateau after the concentration of quantum dots in the PLA film reaches 3% by weight. These results are similar to those seen with ultrasmall CdSe quantum dots encapsulated in polymer films, where the photoluminescence intensity reached a maximum value with increasing concentration of quantum dots.[56] These trends can be attributed to the aggregation in the 3D-printed films, and a corresponding reduction in quantum efficiency of the aggregated quantum dots occurs due to their close proximity and energy transfer.

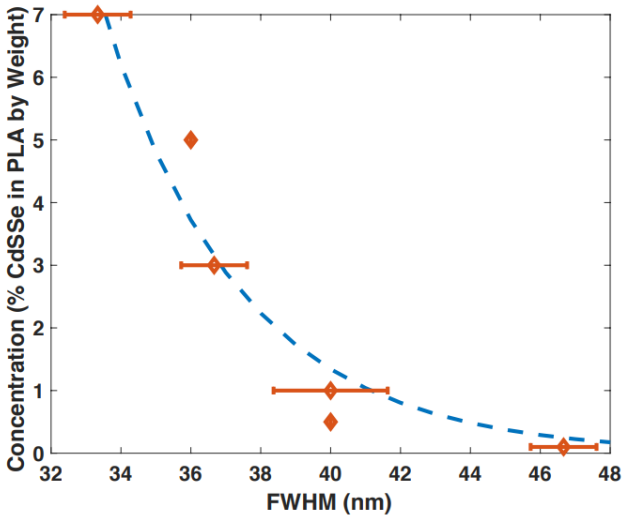

Figure 5.3 Full width half maximum analysis of photoluminescence spectra for PLA/CdSSe quantum dot 3D-printed films at varying concentration of CdSSe quantum dot in PLA by weight.

Beyond absorbance and emission characteristics, fluorescence lifetime measurements of CdSSe quantum dots in solution and 3D-printed PLA/CdSSe quantum dot films were also evaluated. In the time-resolved photoluminescence (TRPL) measurements, CdSSe quantum dots in solution were performed on diluted solutions with optical densities below 0.1 at the lowest-energy absorption transition. These and the PLA/CdSSe films were excited at lower power (~30 mW/cm^2) using a 405 nm pulsed source (100 ps pulse duration) with a repetition rate of 1 MHz. Photoluminescence from the films was filtered with an appropriate long-pass filter and directed onto a single-photon avalanche photodiode (SPAD, Micro Photon Devices, PF-050-0TC). A time correlated single photon-counting unit (TCSPC, PicoHarp 300) was used to generate a histogram of photon arrival times. Lifetimes were determined by fitting the histogram of arrival times to a tri-exponential function:

$$I_{PL}(t) = \Sigma_i = A_i exp(-t/\tau_i) \quad (1)$$

The average lifetime, τ_{avg} was calculated using the fit components as follows:

$$\tau_{avg} = \sum_i^n \frac{A_i \tau_i}{\sum_i^n A_i} \quad (2)$$

Decay curves were fit with the following equation, where A_i and τ_i are the decay amplitudes and lifetimes, respectively:

$$I(t) \sum_{i=3}^{n} A_i e^{-\left(\frac{t}{\tau_i}\right)} \quad (3)$$

The PLA/CdSSe quantum dot films were found to have shorter lifetimes than that of the CdSSe quantum dots in solution (Figure 5.4 and Table 5.1). Again, this behavior can be attributed to the increase in aggregation and energy transfer between the multiple size populations present in the PLA/CdSSe quantum dot 3D-printed samples.

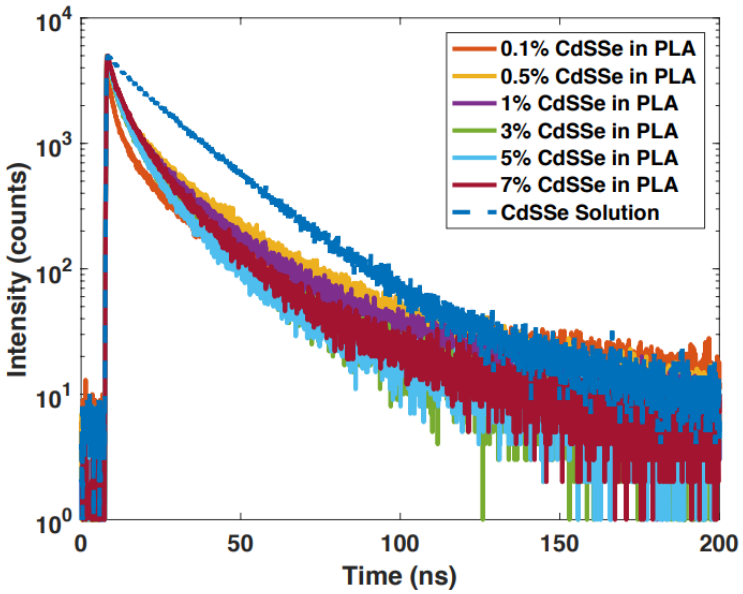

Figure 5.4 Lifetime analysis of 3D-printed PLA/CdSSe quantum dot films and CdSSe quantum dots in solution.

Table 5.1 Lifetime analysis of 3D-printed PLA/CdSSe quantum dot films and CdSSe quantum dots in solution.

Parameter	**CdSSe solution**	**0.1%**	**0.5%**	**1.0%**	**3.0%**	**5.0%**	**7.0%**
A_1 (counts)	210.7	377.8	642.6	517.1	326.7	248.8	252.0
τ_1 (ns)	46.811	33.541	31.656	30.920	30.392	32.506	34.977
A_2 (counts)	4183.3	1308.9	1801.1	1861.9	1980.2	2002.8	2152.4
τ_2 (ns)	19.112	7.905	10.499	10.490	9.265	9.579	11.117
A_3 (counts)	560.9	2675.2	2426.6	2625.4	2696.4	2790.5	2607.1
τ_3 (ns)	4.3954	1.247	1.869	2.009	2.251	2.459	3.006

5.2.2 Thermal Property Characterization of Quantum Dots in Polylactic Acid

Due to heating and functionalizing the nanocomposite material during processing, the thermal properties must be evaluated. The thermal stability of the PLA/CdSSe quantum dot nanocomposite systems was studied using thermogravimetric analysis. Residual weight versus temperature for 3D-printed pure PLA and PLA/CdSSe quantum dot samples are shown in Figure 5.5. All samples, regardless of CdSSe quantum dot loading percent, displayed a single weight loss step beginning near 250 °C, followed by complete material loss occurring above 350 °C. With material extrusion/filament fabrication and 3D-print operation temperatures of 180 °C and 215 °C, respectively, thermogravimetric analysis confirms the thermal stability of PLA/CdSSe quantum dot nanocomposites in the operating temperature range, and that minimal material degradation or loss occurs during both filament fabrication and 3D-printing processes.

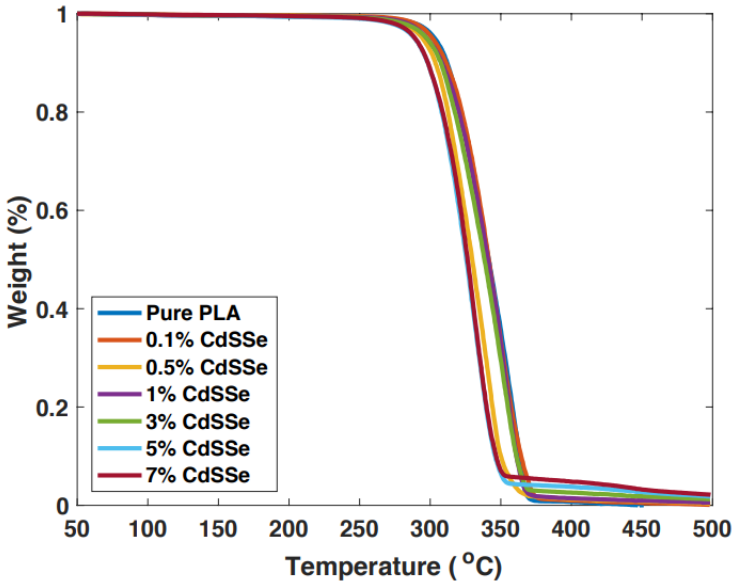

Figure 5.5 Thermogravimetric analysis response of 3D-printed pure PLA and PLA/CdSSe quantum dot films at various concentrations of CdSSe in PLA by weight (0.1%, 0.5%, 1%, 3%, 5%, and 7%). All films studied showed good thermal stability in the range of temperatures used for materials processing and 3D-printing.

The thermal response of 3D-printed PLA/CdSSe quantum dot nanocomposites was also studied using differential scanning calorimetry to better understand the behavior of the polymer chain network and overall impact that filament functionalization has relative to the unmodified PLA host matrix. Representative differential scanning calorimetry scans for 3D-printed pure PLA an PLA/CdSSe quantum dot samples are shown in Figure 5.6 A. Average values for glass transition temperature (T_g), crystallization temperature (T_c), and melting temperature (T_m) are plotted in Figure 5.6 B and further detailed in Table 5.2. With increasing loading percentages of CdSSe quantum dots in PLA, glass transition, crystallization, and melting temperatures were observed to decrease relative to the unmodified pure PLA following materials processing and 3D-print. This decrease in the recorded thermal transitions is found to be more significant at higher loading percentages of CdSSe quantum dots in PLA.

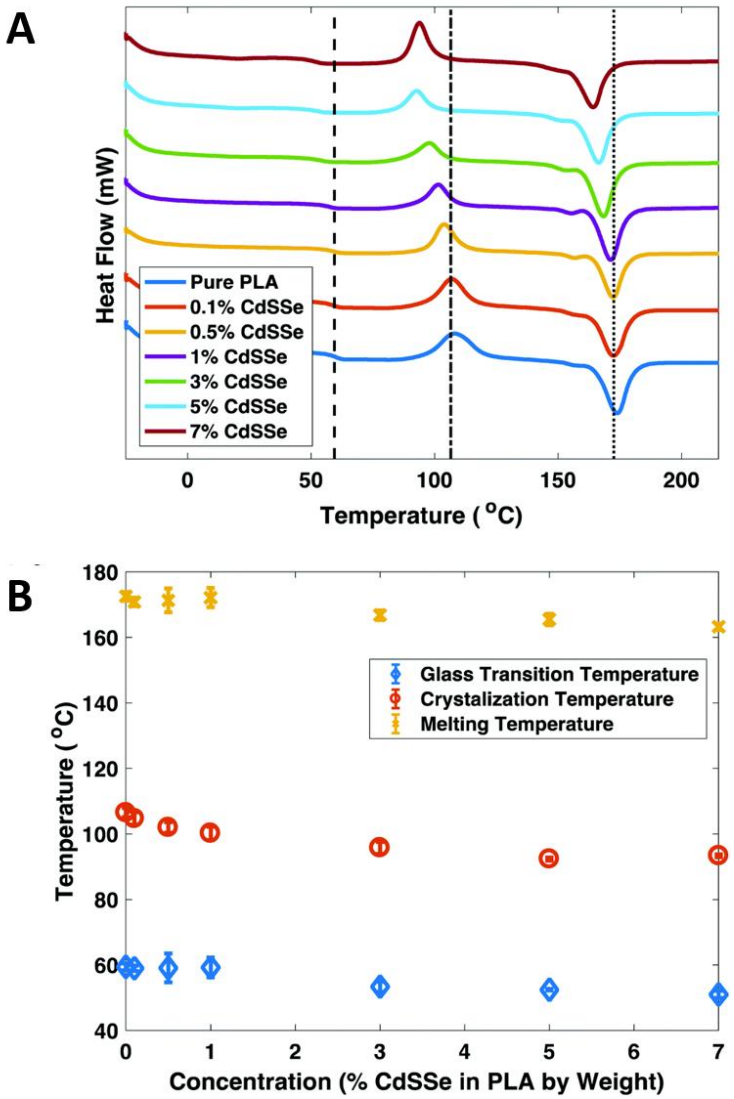

Figure 5.6 A) Representative differential scanning calorimetry curves for 3D-printed pure PLA and PLA/CdSSe quantum dot samples at various concentrations of CdSSe quantum dots in PLA by weight. Dashed lines are guides for the eye and represent average values of pure PLA glass transition temperature, crystallization temperature and melting temperature, from left to right respectively. B) Average glass transition temperature, crystallization temperature and melting temperature for 3D-printed pure PLA and PLA/CdSSe quantum dots at various concentrations of CdSSe quantum dots in PLA by weight.

Table 5.2 Differential scanning calorimetry results for pure PLA and PLA/CdSSe quantum dot samples.

	Glass Transition Temperature (°C)	Crystallization Temperature (°C)	Melting Temperature (°C)
Pure PLA	59.4 ± 1.0	106.5 ± 1.4	172.5 ± 1.3
0.1% PLA/CdSSe	59.0 ± 0.8	104.7 ± 1.9	170.8 ± 1.3
0.5% PLA/CdSSe	59.1 ± 4.4	101.9 ± 1.6	171.3 ± 3.7
1% PLA/CdSSe	59.2 ± 3.0	100.2 ± 2.1	172. 1 ±2.9
3% PLA/CdSSe	53.4 ± 1.5	95.7 ± 1.9	166.8 ± 1.5
5% PLA/CdSSe	52.4 ± 0.3	92.4 ± 0.4	165.5 ± 1.7
7% PLA/CdSSe	51.0 ± 1.1	93.3 ± 0.4	163.2 ± 1.0

These changes in thermal transition can be attributed to a combination of two underlying mechanisms. The first is interactions between the PLA host matrix and natively bound surface ligands present on CdSSe quantum dots. The second mechanism is the aggregation between CdSSe quantum dots in the final 3D-printed structure. Surface ligand-polymer chain interactions are known to have significant impact on the overall behavior of polymer-based nanocomposite systems. For attractive interactions, thermal transitions, specifically glass transition temperature, are typically observed to increase when compared to the unmodified host matrix even at relatively high concentrations of embedded nanomaterials.[100] This behavior is due in part to embedded nanoparticles chemically interacting with and binding to the surrounding polymer host matrix, restricting polymer motion owing to an increased energy barrier for intermolecular chain movement.[101] In the case of 3D-printed PLA/CdSSe quantum dot nanocomposites, the opposite trend is observed. This behavior is attributed to poor interactions between the pure PLA chain network and oleic acid surface ligands present on the embedded CdSSe quantum dots. Fatty acids, such as oleic acid, consisting of a long hydrocarbon chain and terminal carboxyl group, have been previously reported to act as a plasticizing agent when incorporated within a pure PLA host matrix.[102] Plasticizing agents are known to lower glass transition temperature, as well as crystallization and melting temperatures, by effectively allowing for improved polymer chain

mobility and alignment.[103] It is expected that the methyl-rich surface of the oleic acid-modified CdSSe quantum dots interacts weakly through Van der Waals forces with the PLA polymer chain network. As such, it is believed that the lack of strong intermolecular interactions between oleic acid and PLA results in the formation of additional free surfaces and free spaces near embedded quantum dots, as PLA is unable to adequately wet the surface of oleic acid-capped CdSSe quantum dots.

In addition to the impact of native surface ligands, the size and concentration of embedded nanomaterials, including the presence of aggregates, has also been found to affect the overall thermal response of polymer-based nanocomposite systems.[104–106] As previously discussed, CdSSe quantum dots were observed to form aggregates in micelle-like structures at increasing concentration of quantum dots in PLA (Figure 5.1). With weak chemical interactions between the surrounding polymer matrix, aggregated quantum dots can be thought of as acting as void spaces in the 3D-printed PLA/CdSSe quantum dot nanocomposite systems. The presence of voids at nanoparticle-polymer interfaces have been found to reduce the glass transition behavior of polymer-based nanocomposite systems due to the resultant increased polymer mobility near the regions surrounding embedded nanomaterials. [101] Thermal transitions of 3D-printed PLA/CdSSe quantum dot nanocomposites are expected to decrease with increasing aggregate size due to the formation of larger polymer chain discontinuities and the resultant formation of interphase regions near quantum dot surfaces resulting from weak polymer-nanoparticle interactions, consistent with the trends obtained in this study.[107]

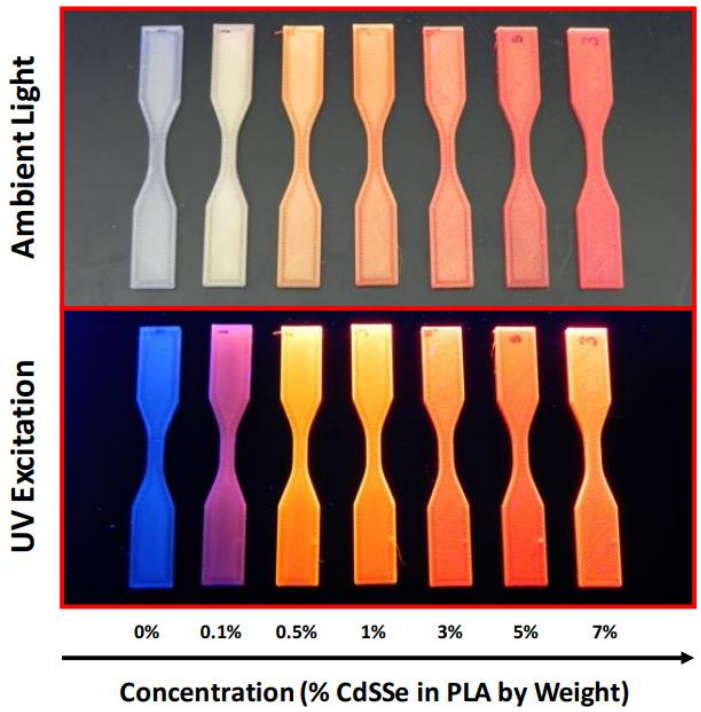

Figure 5.7 3D-printed ASTM D638 Type V tensile dogbone specimen with varying of concentration of CdSSe in PLA by weight under ambient light (top) and UV excitation (bottom). Blue coloration on pure PLA sample (0% CdSSe in PLA by weight) is due to reflection of UV excitation source on the 3D-printed sample.

5.2.3 Mechanical Property Analysis of Quantum Dots Embedded in Polylactic Acid Dogbones

The tensile load responses of 3D-printed pure PLA and PLA/CdSSe quantum samples were studied to evaluate the impact of filament functionalization on the mechanical properties of as-printed PLA/CdSSe quantum dot nanocomposites. The presence of CdSSe quantum dots in 3D-printed dogbone samples is visible under both ambient light, where samples maintained the orange coloration of CdSSe quantum dots in solution, and UV excitation, where the fluorescent behavior of the embedded quantum dots was preserved following materials processing and 3D-printing (Figure 5.7). Representative stress versus strain curves for 3D-printed pure PLA and PLA/CdSSe quantum dot dogbone specimens loaded in tension are shown in Figure 5.8 A. A summary of relevant mechanical testing results, including average ultimate tensile strength,

average strain at break, as well as average elastic modulus and toughness for all samples evaluated is presented in Figure 5.8 and further detailed in Table 5.3.

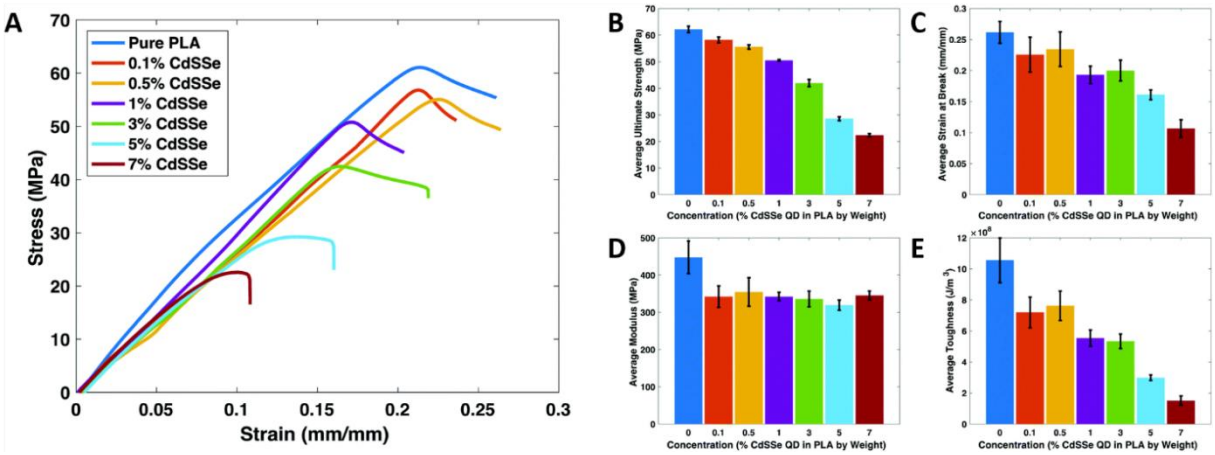

Figure 5.8 Tensile load response of 3D-printed pure PLA and PLA/CdSSe quantum dot dogbone specimens. A) Representative stress vs. strain curves for varying concentrations of CdSSe quantum dots in PLA by weight. B) Average ultimate strength for varying concentrations of CdSSe quantum dots in PLA by weight. C) Average strain at break for varying concentrations of CdSSe quantum dots in PLA by weight. D) Average modulus for varying concentrations of CdSSe quantum dots in PLA by weight. E) Average toughness for varying concentrations of CdSSe quantum dots in PLA by weight. Similar to the results obtained for differential scanning calorimetry testing, the mechanical load response of 3D-printed PLA/CdSSe quantum dot specimens was found to be dependent on the overall concentration of embedded quantum dots. For the tensile dogbone specimens, ultimate strength, strain, modulus and toughness were all observed to decrease relative to pure PLA following the inclusion of CdSSe quantum dots within the 3D-printed structures. The largest decrease in material strength properties were, on average, observed for the highest concentrations of embedded quantum dots. In fact, ultimate strength and fracture toughness for PLA/CdSSe quantum dot samples containing 7.0% quantum dots by weight were found to decrease by 63% and 85%, respectively, relative to the unmodified pure PLA matrix. These changes in material strength properties are attributed to a combination of weak polymer-surface ligand interactions and quantum dot aggregation present in the final 3D-printed structures.

Table 5.3 Mechanical properties of 3D-printed pure PLA and PLA/CdSSe quantum dot tensile test specimens.

	Average Ultimate Tensile Strength (MPa)	Average Strain at Break (mm/mm)	Average Tensile Modulus (MPa)	Average Toughness ($x10^8$ J/m^3)
Pure PLA	62 ± 1.0	0.26 ± 0.02	447 ± 43	11 ± 1.4
0.1% PLA/CdSSe	58 ± 1.0	0.23 ± 0.03	342 ±29	7.2 ± 0.99
0.5% PLA/CdSSe	55 ± 0.81	0.23 ± 0.03	354 ± 38	7.6 ± 0.95
1% PLA/CdSSe	50 ± 0.26	0.19 ± 0.01	342 ± 11	5.5 ± 0.52
3% PLA/CdSSe	42 ± 1.0	0.20 ± 0.02	336 ± 21	5.3 ± 0.47
5% PLA/CdSSe	29 ± 0.71	0.16 ± 0.01	319 ± 14	3.0 ± 0.19
7% PLA/CdSSe	22 ± 0.60	0.11 ± 0.01	345 ± 12	1.5 ± 0.30

Upon initial inspection of the recorded thermal and mechanical testing results, the embedded quantum dots appear at first to be acting as a plasticizing agent. For polymer based systems, and PLA in particular, the addition of plasticizers has been shown to decrease both the ultimate tensile strength and tensile modulus, consistent with the results obtained for 3D-printed PLA/CdSSe quantum dots samples.[108,109] By promoting intermolecular chain movement, plasticizers are also well known to cause increased deformation for thermoplastic materials. In the case of the 3D-printed PLA/CdSSe quantum dot nanocomposite system, elongation at break was observed to decrease, resulting in a more brittle material response with increasing concentrations of embedded quantum dots; this is the opposite effect of what is typically observed for plasticized polymer systems.

At low concentrations of embedded quantum dots (0.1% and 0.5% PLA/CdSSe), no statistical difference in the recorded strain response was observed relative to the unmodified pure PLA host matrix, as samples had overlapping standard deviations. These samples also displayed

the smallest changes in recorded ultimate strength and toughness, as the low concentrations of embedded quantum dots have limited impact on the polymer chain network. The formation of aggregates in polymer-based nanocomposite structures, however, has been shown to significantly influence the underlying polymer structure and resulting thermal and mechanical behaviors. The presence of aggregates in a polymer matrix, such as those observed in 3D-printed PLA/CdSSe quantum dot structures at higher concentrations of embedded quantum dots, can act as sites for crack initiation and propagation that ultimately lead to the premature and brittle failure of nanocomposite systems.[101] The combined contribution of aggregation and the overall lack of interaction between oleic acid-capped CdSSe quantum dot nanocomposites to carry mechanical load. The resultant outcome is a decreased ultimate tensile strength and strain at failure, where aggregated quantum dots ultimately form representative void spacings within the PLA host matrix.

The impact of quantum dot functionalization on the recorded modulus and toughness of PLA/CdSSe quantum dot samples should also be noted. Modulus is commonly defined as the ability of a material to deform elastically under the application of external load, and it offers a means to measure corresponding stiffness of the material. Modulus for PLA/CdSSe quantum dot samples was recorded directly during tensile testing as the slope of the linear component of the stress-strain curve (Figure 5.8 A). Following the addition of CdSSe quantum dots to the PLA host matrix, a decrease in the recorded modulus was observed. Unlike other thermal and mechanical testing results, the modulus did not appear to be dependent upon the overall loading of the embedded quantum dots. Instead, a single drop in modulus of approximately 25% relative to unmodified pure PLA was observed. These results are in line with previously reported polymer-nanocomposite systems, where increased polymer chain mobility due to the presence of

embedded nanomaterials resulted in a decreased modulus due to the lack of intermolecular interactions present at the surface of the embedded quantum dots.[110,111]

Toughness was calculated as the integral under the stress-strain curve, which correlates to the ability of a material to absorb energy when loaded. Typically, ductile materials are thought of being "tougher" as they are able to absorb energy over longer periods of time due to increased elongation before failure. With increasing concentration of CdSSe quantum dots in PLA, a significant decrease in material toughness was observed. Consistent with the reduced ultimate strength and strain at failure, material toughness decreases in accordance with the overall loading of embedded quantum dots. This reduction in capacity to absorb energy results from quantum dot aggregation and a corresponding inability to carry load due to the poor intermolecular interactions between the CdSSe quantum dots and the surrounding PLA matrix.[110]

5.2.4 3D-Printed Quantum Dot Light Devices

In order to demonstrate a significant potential application for 3D-printed PLA/CdSSe quantum nanocomposite systems, hollow U-shaped optical light pipes were fabricated (Figure 5.9 A and B).[112] Light pipes are components and devices that are used to transport or redirect light from a source to a desired location.[113] Proof-of-concept light pipes were 3D-printed using an inner shell of PLA/CdSSe quantum dot functionalized material (0.5% and 3.0% CdSSe quantum PLA/CdSSe loading by weight), surrounded by a white PLA exterior to aid with internal reflection of the quantum dot emission. Although the light pipe does not currently operate using total internal reflection, it is believed to transport light through a combination of reflection and scattering. When excited with an external emission source, a red shift in the wavelength of maximum photoluminescence emission relative to quantum dots in solution was observed for the light pipe devices examined, similar to trends observed for PLA/CdSSe

quantum dot thin film samples discussed previously (Figure 5.9 C). Opposite from the trends displayed for 3D-printed PLA/CdSSe quantum dot thin films, though, the photoluminescence emission intensity for the optical light pipe was observed to decrease with increasing concentration of embedded quantum dots (as the weight percent loading increased from 0.5% to 3%). This behavior is due to the attenuation of quantum dot emission owing to the increased number of quantum dots absorbing light in the 3% PLA/CdSSe quantum dot light pipe as compared to the 0.5% PLA/CdSSe quantum dot light pipe.[114] Additionally, as the thickness of the PLA/CdSSe quantum dot inner layer was reduced, the recorded photoluminescence emission intensity was observed to decrease (Figure 5.9 D). This trend is attributed to the decrease in absorption cross-section and corresponding reduction in the overall number of quantum dots along the excitation path. By tuning the size, concentration and type of embedded quantum dots, as well as the thickness of the inner quantum dot-functionalized layer, a customized optical light pipe with tunable emission wavelength and intensity can be obtained by 3D-printing. Additionally, as a second example of a representative application for 3D-printed light device, a Vanderbilt logo was printed using PLA/CdSSe quantum dot filament encased within a white PLA surround (Figure 5.9 E and F). This device represents the capability of 3D-printing to fabricate bulk-scale fluorescent displays and devices using multiple materials.

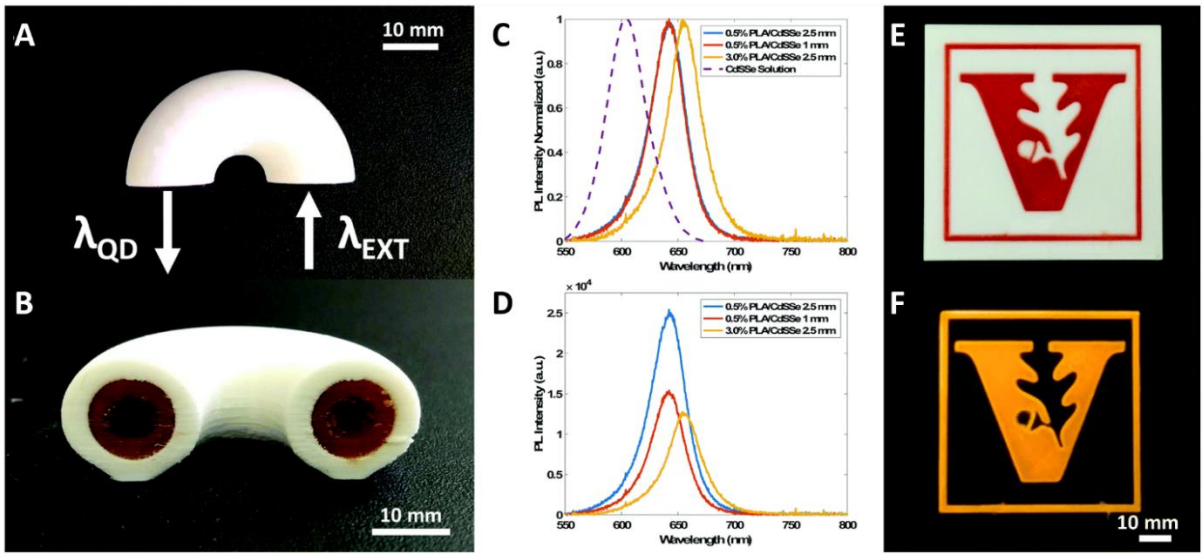

Figure 5.9 3D-printed optical light pipe. A) Top view. B) Profile view, thickness of interior PLA/CdSSe quantum dot layers tested was 1 mm and 2.5 mm, respectively. C) Normalized PL spectra for CdSSe quantum dot solution and 3D-printed PLA/CdSSe quantum dot optical light pipes. D) PL spectra for 3D-printed PLA/CdSSe quantum dot optical light pipes. E) 3D-printed fluorescent device under ambient light. F) 3D-printed fluorescent device under UV excitation (picture was taken using a UV filter).

5.3 Conclusions

In this work, the ability to develop functionalized nanocomposite materials compatible with 3D-print applications through the incorporation of CdSSe quantum dots within a PLA host matrix was successfully demonstrated. Focusing on materials processing considerations, CdSSe quantum dots and PLA are mixed, dried, and extruded to obtain filament compatible with stock fused deposition modeling (FDM) type 3D printers. The optical, thermal, and mechanical responses of 3D-printed CdSSe quantum dot structures were studied to evaluate the impact that filament functionalization has relative to the unmodified PLA host matrix. While the overall absorbance behavior of CdSSe quantum dots was maintain following printing, slight changes in the photoluminescent behavior was observed for 3D-printed CdSSe quantum dot structures. Most noticeable was the red-shift in maximum photoluminescence emission intensity for increasing

weight percent loading of embedded CdSSe quantum dots. The spectral shift is attributed to a combination of aggregated quantum dots within the 3D-printed structures and corresponding reabsorption resulting from multiple size populations within embedded quantum dots. The thermal and mechanical behaviors of 3D-printed PLA/CdSSe quantum dot test specimens were also found to be dependent on the overall loading of embedded quantum dots. In this case, reductions in thermal transitions and material strength properties are attributed to the presence of aggregated quantum dots and the overall lack of interaction between the natively bound oleic acid surface ligands present on CdSSe quantum dots and the surrounding PLA host matrix. By tuning the surface composition of the quantum dot to promote favorable interactions with the polymer host matrix, future research will focus on the development of 3D-printed nanocomposite systems with enhanced optical and mechanical strength properties. The ability to incorporate quantum dots and other nanomaterial within 3D-printing and additive manufacturing processes represents a unique opportunity for the design and development of new materials and structures with advanced, multifunctional behaviors and properties for a variety of applications and uses.

CHAPTER VI

CONCLUSIONS AND FUTURE OUTLOOK

6.1 Overall Conclusions

The broad, white-light emission from the ultrasmall CdSe quantum dots is dependent on the surface ligands. This is apparent with the post-synthesis treatments of formic acid and citric acid, where the quantum yield of the CdSe quantum dots is significantly increased. The overall broad emission is found to increase in the entire spectra, but the first emission peak has the greatest enhancement. This causes the white-light to cool, resulting in more “blue” CIE coordinates. The increase in the quantum yield for the citric acid treated CdSe quantum dots is believed to be due to the pinned emission reverting to band gap emission, a more efficient process. The citric acid treated dots are also more stable than those treated t=with formic acid, possibly due to the multiple binding site of the citric acid molecule. Owing to the lower stability in solution, the formic acid treated CdSe quantum dots were encapsulated in BP-PFCB, and the optimal loading weight percent was determined.

Ultrasmall CdSe quantum dots were used for damage detection in epoxy samples, from cylinders to thin discs to surface coated aluminum and fiberglass tensile samples. By monitoring distinct quenching in the emission spectra for these composite samples, the application of external loads to the sample were able to be detected and monitored. The decrease in emission observed for increasing levels of external load is due to the removal of surface ligands present on CdSe quantum dots. In all samples evaluated, both in compression and tension, the largest

decrease in emission was observed at the first load increment. Beyond the first load case, though, samples had varied responses to the application of external loads. Due to the composite nature of the fiberglass tensile sample, a biphasic response was observed, where after a certain external load was reached, the individual fibers broke and additional CdSe quantum dots were expose to the excitation source, resulting in an increase in emission intensity. In, all the use of CdSe quantum dots presents a promising alternative to detecting and communicating the occurrence of external loads acting on a material by monitoring distinct changes in the emission spectra.

Developing functionalized nanocomposite materials compatible with 3D-printing applications through the incorporation of CdSSe quantum dots within a PLA host matrix was successfully demonstrated. While the overall absorbance behavior of CdSSe quantum dots was maintain following printing, slight changes in the photoluminescent behavior was observed for 3D-printed CdSSe quantum dot structures. Most noticeable was the red-shift in maximum photoluminescence emission intensity for increasing weight percent loading of embedded CdSSe quantum dots, which is attributed to a combination of aggregated quantum dots within the structures and corresponding reabsorption resulting from multiple size populations within embedded quantum dots. The thermal and mechanical behaviors of 3D-printed PLA/CdSSe quantum dot test specimens were also found to be dependent on the overall loading of embedded quantum dots, with reductions in thermal transitions and material strength properties due to the presence of aggregated quantum dots and the overall lack of interaction between the natively bound oleic acid surface ligands present on CdSSe quantum dots and the surrounding PLA host matrix.

6.2 Future Directions

Studies into determining the binding mechanism of citric acid to the surface of ultrasmall CdSe quantum dots should be pursued. It may be that using various multidentate molecules could lead to new information about why the quantum yield and the stability is increased after the post-synthesis treatment. New analysis techniques could also be utilized to help determine how the citric acid is bound to the surface of the quantum dots. Such techniques include ^{113}Cd NMR, magic-angle spinning (MAS), and X-ray photoelectron spectroscopy (XPS). ^{113}Cd NMR and MAS would present information on the coordination patterns of the cadmium atoms.[115116] XPS would provide a method to characterize the stoichiometry and surface properties of the quantum dots before and after ligand exchange.[117] Once the binding mechanism is understood, other methods of increasing the quantum yield can be evaluated.

Efficiency and stability improvements in the ultrasmall CdSe quantum dot allow for the fabrication of enhanced photoluminescent and electroluminescent devices. It was predicted that to compensate for any other deficiencies in the device, a quantum yield of the ultrasmall CdSe quantum dots needed to be at least 40%, which has now been accomplished. Since the discovery of EL devices using untreated ultrasmall CdSe, more efficient hole- and electron-transport layers have been studied. What is being called the "fourth generation" of QD-LEDs, consist of hybrid organic and inorganic charge transfer layers, where the n-type layer is a metal oxide, such as solution processed metal oxide nanoparticles. These monochromatic devices have reported efficiencies over 10%.[65]

Thermal and mechanical advances in the quantum dot functionalized PLA should be considered. Due to the lack of interaction between the oleic acid ligand on the surface of the quantum dot and the PLA host matrix causing decreases in the thermal and mechanical

properties of the structure have been observed. Modifications to the ligand shell, such as with the citric acid post-synthesis treatment could be assessed, using shorter ligands or ligands with a polar terminal group. In addition to modifying the surface ligands on the graded-alloy CdSSe quantum dots, various sizes of quantum dots can be utilized to produce multi-colored structures. Using blue and green emitting ZnS quantum dots would satisfy this as well as having the added benefit of being non-toxic to the environment.

APPENDIX A

QUANTUM YIELD CALCULATIONS

With the significant focus on the unique optical characteristics and tunability of quantum dots, the fluorescence efficiency is very important. When the quantum dot absorbs a photon of light, an energetically excited state is formed. Depending on the nature of the quantum dot and its surroundings, the outcome of the excited state is varied, with the end result being a loss of energy and a return to the ground state. The photoluminescence quantum yield (QY) measurement is an experimental technique where one can calculate the brightness of fluorescent samples. The value is a measure of how many photons the sample emits in relation to how many photons it has absorbed:

$$QY = \frac{\#\ photons\ emitted}{\#\ photons\ absorbed} \times 100\% \qquad \text{(A.1)}$$

Quantum yields of quantum dots dispersed in toluene were obtained using the single-point method.[118] Using this method, quantum yield is calculated using the integrated emission intensities from a single sample and a reference dye at the same concentrations. The reference dye that is used is an organic dye of known quantum yield. The value of quantum yield is then determined according to:

$$QY = Q_R \frac{I}{I_R} \frac{OD_R}{OD} \frac{n^2}{{n_R}^2} \qquad \text{(A.2)}$$

Where the subscript R denotes values for the reference dye, I is the integrated fluorescence intensity, OD is the optical density or absorbance of the sample at the excitation wavelength, and *n* is the refractive index of the solvent. Optical densities of the quantum dots and the reference dyes were kept between 0.09 and 0.11 in a glass cuvette with a path length of 1 cm. Organic dyes

with optical absorption and fluorescence spectra that overlap with those of the quantum dot samples. For the ultrasmall CdSe quantum dots, Coumarin 152A in ethanol (Q = 0.08)[119] was used, and for the graded-alloy CdSSe quantum dots, Rhodamine 6G in ethanol (Q = 0.94)[120] was used.

APPENDIX B

CIE COORDINATES AND CALCULATIONS

To determine how pure white the white-light emission of the ultrasmall CdSe quantum dots is, the Commission Internationale de L'Eclairage (CIE) 1931 chromaticity coordinates can be calculated. Pure white is defined by having coordinates of 0.333, 0.333.[121] To calculate the 1931 chromaticity coordinates the following procedure is used. First, an emission spectrum is collected from 400 to 800 nm. Second, the wavelength intensity values are multiplied by each of the x, y, and z color matching functions provided (Figure B.1 and Equations B.1 – B.3) to obtain $\bar{x}$, $\bar{y}$, and $\bar{z}$ value for each wavelength.

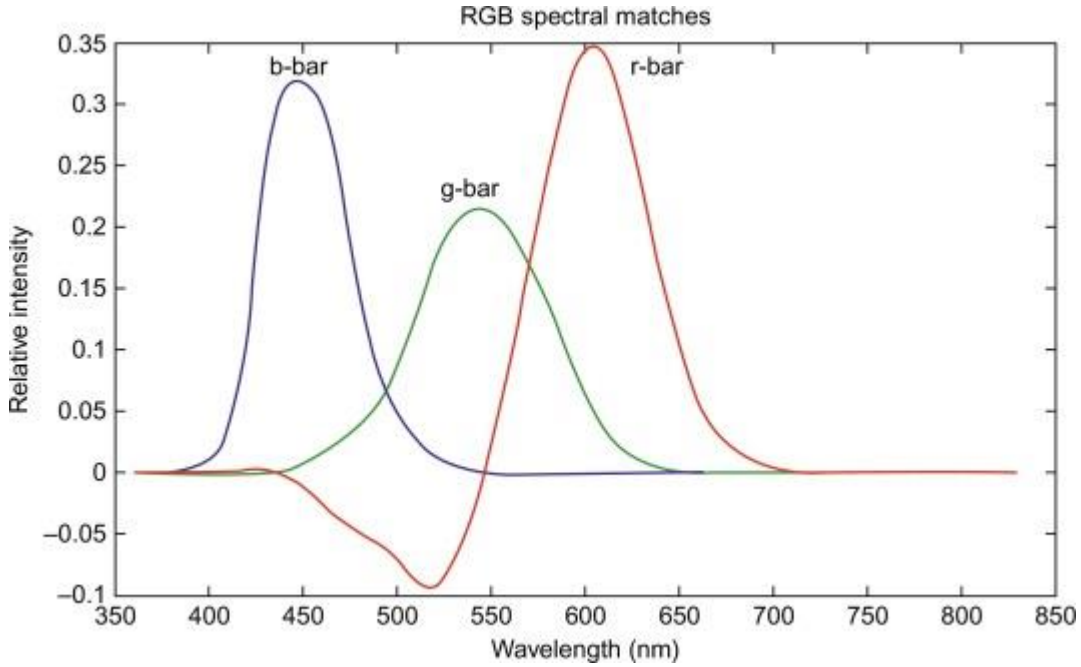

Figure B.1 Red, green, and blue color matching functions.

$$\bar{x} = 2.7688r + 1.7517g + 1.1301b \qquad \text{(B.1)}$$

$$\bar{y} = 1.0000r + 4.5906g + 0.0601b` \quad \text{(B.2)}$$

$$\bar{z} = 0.0000r + 0.0565g + 5.5942b \quad \text{(B.3)}$$

Next, the values for $\bar{x}$, $\bar{y}$, and $\bar{z}$ are summed to obtain $\bar{X}$, $\bar{Y}$, and $\bar{Z}$. These are normalized to the tri-stimulus values using the following equations to obtain Xstim, Ystim, and and Zstim.

$$Xstim = \frac{\bar{X}}{(\bar{X}+\bar{Y}+\bar{Z})} \quad \text{(B.4)}$$

$$Ystim = \frac{\bar{Y}}{(\bar{X}+\bar{Y}+\bar{Z})} \quad \text{(B.5)}$$

$$Zstim = \frac{\bar{Z}}{(\bar{X}+\bar{Y}+\bar{Z})} \quad \text{(B.6)}$$

The 1960 color coordinates u and v can be obtained via the following equations:

$$u = \frac{4 * Xstim}{(Xstim+15 * Ystim+3 * Zstim)} \quad \text{(B.7)}$$

$$v = \frac{6 * Ystim}{(Xstim+15 * Ystim+3 * Zstim)} \quad \text{(B.8)}$$

The 1931 color coordinates x and y can be obtained via the following equations:

$$x = \frac{3*u}{(2*u-8*v+4)} \quad \text{(B.9)}$$

$$y = \frac{2*v}{(2*u-8*v+4)} \quad \text{(B.10)}$$

REFERENCES

(1) U.S. Energy Information Administration. *Annual Energy Outlook 2019 with Projections to 2050*; 2019; Vol. 44.

(2) Ragheb, M. Solar Thermal Power and Energy Storage Historical Perspective, 2011.

(3) Shafiee, S.; Topal, E. When Will Fossil Fuel Reserves Be Diminished? *Energy Policy* **2009**.

(4) Stein, E. W. A Comprehensive Multi-Criteria Model to Rank Electric Energy Production Technologies. *Renewable and Sustainable Energy Reviews*, 2013.

(5) Parfit, M. Future Power: Where Will the World Get Its Next Energy Fix? *National Geographic Magazine*. 2019,.

(6) U.S. Energy Information Adminstration. *Electric Power Monthly with Data for June 2019*; 2019.

(7) Blunden, J.; Arndt, D. S. State of the Climate in 2018. *Bull. Amer. Meteor. Soc.* **2019**, *100*, Si-S305.

(8) US EPA. Repeal of the Clean Power Plan; Emission Guidelines for Greenhouse Gas Emissions From Existing Electric Utility Generating Units; Revisions to Emission Guidelines Implementing Regulations. *Fed. Regist.* **2019**, *84*, 32520–32584.

(9) IEA. World Energy Outlook 2018: Electricity. **2018**, 1–645.

(10) Williams, B. *A History of Light and Lighting*; 2.3.; 2005.

(11) Brox, J. *Brilliant: The Evolution of Artificial Light*; Houghton Mifflin Harcourt, 2010.

(12) Fouquet, R.; Pearson, P. J. G. The Long Run Demand for Lighting: Elastics and Rebound Effects in Different Phases of Economic Development. *BC3 Work. Pap. Ser.* **2011**, *06*.

(13) Matulka, R.; Wood, D. History of the Light Bulb https://www.energy.gov/articles/history-light-bulb.

(14) Buccitelli, N.; Elliott, C.; Schober, S.; Yamada, M. *2015 U . S . Lighting Market Characterization*; 2017.

(15) United States, Congress, H. *Energy Independence and Security Act*; 2007.

(16) Phillips, J. M.; Burrows, P. E. Basic Research Needs for Solid-State Lighting. *US Dep. Energy* **2006**.

(17) International Energy Agency. *World Energy Outlook*; 2006.

(18) 修二·中村; Pearton, S.; Fasol, G. *The Blue Laser Diode: The Complete Story*; 2nd ed.; Springer Science & Business Media, 2000.

(19) U.S. Department of Energy. *Energy Savings Potential of Solid-State Lighting in General Illumination Applications*; 2003.

(20) Alivisatos, A. P.; Cummings, P.; Yoreo, J. De; Fishthorn, K. *Nanoscience Research for Energy Needs*; 2004.

(21) Jacoby, M. Tuning Phosphors for Better White Light. *C&EN Glob. Enterp.* **2018**, *96*, 28–32.

(22) *2018 Solid-State Lighting R&D Opportunities*; 2018.

(23) Stockman, A.; Macleod, D. I. A.; Johnson, N. E. *Spectral Sensitivities of the Human Cones*; 1993; Vol. 10.

(24) Sharpe, L. T.; Stockman, A.; Jagla, W.; Jagle, H. A Luminous Efficiency Function, V*(1), for Daylight Adaptation. *J. Vis.* **2005**, *5*, 948–968.

(25) Erdem, T.; Demir, H. V. Color Science and Photometry for Lighting with LEDs and Semiconductor Nanocrystals. *SPRINGER BRIEFS Appl. Sci. Technol.* **2019**.

(26) Liu, R.-S. *Phosphors, Up Conversion Nano Particles, Quantum Dots and Their Application*; 2016.

(27) Brus, L. E. Electron–Electron and Electron-Hole Interactions in Small Semiconductor Crystallites: The Size Dependence of the Lowest Excited Electronic State. *J. Chem. Phys.* **1984**, *80*, 4403.

(28) Smith, A. M.; Nie, S. Semiconductor Nanocrystals: Structure, Properties, and Band Gap Engineering. **2010**.

(29) Klimov, V. I. *Semiconductor and Metal Nanocrystals: Synthesis and Optical Properties*; Marcel Dekker, Inc.: New York, 2004.

(30) Kippeny, T.; Swafford, L. a.; Rosenthal, S. J. Semiconductor Nanocrystals: A Powerful Visual Aid for Introducing the Particle in a Box. *J. Chem. Educ.* **2002**, *79*, 1094.

(31) Murray, C. B.; Norris, D. j.; Bawendi, M. Synthesis and Characterization of Nearly Monodisperse CdE (E= S, Se, Te) Semiconductor Nanocrystallites. *J. Am. Chem. Soc.* **1993**, *115*, 8706–8715.

(32) Neeleshwar, S.; Chen, C. L.; Tsai, C. B.; Chen, Y. Y.; Chen, C. C.; Shyu, S. G.; Seehra, M. S. Size-Dependent Properties of CdSe Quantum Dots.

(33) Kagan, C. R.; Murray, C. B.; Nirmal, M.; Bawendi, M. G. *Electronic Energy Transfer in CdSe Quantum Dot Solids*; 1996.

(34) Ekimov, A. I.; Hache, F.; Schanne-Klein, M. C.; Ricard, D.; Flytzanis, C. Absorption and Intensity-Dependent Photoluminescence Measurements on CdSe Quantum Dots: Assignment of the First Electronic Transitions. *J. Opt. Soc. Am. B* **1993**, *10*, 100–107.

(35) Soloviev, V. N.; Eichhofer, A.; Fenske, D.; Banin, U. Molecular Limit of a Bulk Semiconductor of the "Band Gap" in CdSe Cluster Molecules. *J. Am. Chem. Soc.* **2000**, *122*, 2673–2674.

(36) Medintz, I. L.; Uyeda, H. T.; Goldman, E. R.; Mattoussi, H. Quantum Dot Bioconjugates for Imaging, Labelling and Sensing. *Nat. Mater.* **2005**, *4*, 435–446.

(37) Kovtun, O.; Tomlinson, I. D.; Bailey, D. M.; Thal, L. B.; Ross, E. J.; Harris, L.; Frankland, M. P.; Ferguson, R. S.; Glaser, Z.; Greer, J.; *et al.* Single Quantum Dot Tracking Illuminates Neuroscience at the Nanoscale. *Chem. Phys. Lett.* **2018**, *706*, 741–752.

(38) Guo, Y.; Shi, S.; Hagen, G.; Zank, B.; Arango, A. Core-Shell Colloidal Quantum Dots for Photovoltaics with Improved Open Circuit Voltage. *APS March Meet. 2019, Abstr. id.F33.003* **2019**.

(39) Niezgoda, J. S.; Yap, E.; Keene, J. D.; McBride, J. R.; Rosenthal, S. J. Plasmonic CuxInyS2 Quantum Dots Make Better Photovoltaics than Their Nonplasmonic Counterparts. *Nano Lett.* **2014**, *14*, 3262–3269.

(40) Mangum, B. D.; Landes, T. S.; Theobald, B. R.; Kurtin, J. N. Exploring the Bounds of Narrow-Band Quantum Dot Downconverted LEDs. *Photonics Res.* **2017**, *5*, A13–A22.

(41) Supran, G. J.; Shirasaki, Y.; Song, K. W.; Caruge, J.-M.; Kazlas, P. T.; Coe-Sullivan, S.; Andrew, T. L.; Bawendi, M. G.; Bulović, V. QLEDs for Displays and Solid-State Lighting. *MRS Bull.* **2013**, *38*, 703–711.

(42) Colvin, V. L.; Schlamp, M. C.; Alivisatos, A. P. Light-Emitting Diodes Made from Cadmium Selenide Nanocrystals and a Semiconducting Polymer. *Nature* **1994**, *370*, 354–357.

(43) Hames, B. C.; Mora-Seró, I.; Sánchez, R. S. Device Performance and Light Characteristics Stability of Quantum-Dot-Based White-Light-Emitting Diodes. *Nano Res.* **2018**, *11*, 1575–1588.

(44) Li, Y. Q.; Rizzo, A.; Cingolani, R.; Gigli, G. Bright White-Light-Emitting Device from Ternary Nanocrystal Composites. *Adv. Mater.* **2006**, *18*, 2545–2548.

(45) Bowers, M. J.; McBride, J. R.; Rosenthal, S. J. White-Light Emission from Magic-Sized Cadmium Selenide Nanocrystals. *J. Am. Chem. Soc.* **2005**, *127*, 15378–15379.

(46) Bowers, M. J.; McBride, J. R.; Garrett, M. D.; Sammons, J. A.; Dukes, A. D.; Schreuder, M. A.; Watt, T. L.; Lupini, A. R.; Pennycook, S. J.; Rosenthal, S. J. Structure and Ultrafast Dynamics of White-Light-Emitting CdSe Nanocrystals. *J. Am. Chem. Soc.* **2009**, *131*, 5730–5731.

(47) Schreuder, M. A.; Xiao, K.; Ivanov, I. N.; Weiss, S. M.; Rosenthal, S. J. White Light-Emitting Diodes Based on Ultrasmall CdSe Nanocrystal Electroluminescence. *Nano Lett.* **2010**, *10*, 573–576.

(48) Gosnell, J. D.; Schreuder, M. A.; Rosenthal, S. J.; Weiss, S. M. Efficiency Improvements of White-Light CdSe Nanocrystal-Based LEDs. In *Seventh International Conference on Solid State Lighting*; SPIE, 2007; Vol. 6669, p. 66690R.

(49) Li, J. J.; Wang, Y. A.; Guo, W.; Keay, J. C.; Mishima, T. D.; Johnson, M. B.; Peng, X. Large-Scale Synthesis of Nearly Monodisperse CdSe/CdS Core/Shell Nanocrystals Using Air-Stable Reagents via Successive Ion Layer Adsorption and Reaction. *J. Am. Chem. Soc.* **2003**, *125*, 12567–12575.

(50) Mcbride, J.; Treadway, J.; Feldman, L. C.; Pennycook, S. J.; Rosenthal, S. J. Structural Basis for near Unity Quantum Yield Core/Shell Nanostructures. *Nano Lett.* **2006**, *6*, 1496–1501.

(51) Schreuder, M. A.; Mcbride, J. R.; Dukes III, A. D.; Sammons, J. A.; Rosenthal, S. J. Control of Surface State Emission via Phosphonic Acid Modulation in Ultrasmall CdSe Nanocrystals. *J. Phys. Chem. C* **2009**, *113*, 8169–8176.

(52) Shen, Y.; Gee, M. Y.; Tan, R.; Pellechia, P. J.; Greytak, A. B. Purification of Quantum Dots by Gel Permeation Chromatography and the Effect of Excess Ligands on Shell Growth and Ligand Exchange. *Chem. Mater.* **2013**, *25*, 2838–2848.

(53) Keene, J. D.; McBride, J. R.; Orfield, N. J.; Rosenthal, S. J. Elimination of Hole-Surface Overlap in Graded CdSxSe1- x Nanocrystals Revealed by Ultrafast Fluorescence Upconversion Spectroscopy. *ACS Nano* **2014**, *8*, 10665–10673.

(54) Rosson, T. E.; Claiborne, S. M.; Mcbride, J. R.; Stratton, B. S.; Rosenthal, S. J. Bright White Light Emission from Ultrasmall Cadmium Selenide Nanocrystals. *J. Am. Chem. Soc.* **2012**, *134*, 8006–8009.

(55) Vanwie, T.; Wysocki, E.; Mcbride, J. R.; Rosenthal, S. J. Bright Cool White Emission from Ultrasmall CdSe Quantum Dots. **2019**.

(56) Schreuder, M. A.; Gosnell, J. D.; Smith, N. J.; Warnement, M. R.; Weiss, S. M.; Rosenthal, S. J. Encapsulated White-Light CdSe Nanocrystals as Nanophosphors for Solid-State Lighting. *J. Mater. Chem.* **2008**, *18*, 970.

(57) Brubaker, C. D.; Frecker, T. M.; Njoroge, I.; Smudde, C.; Shane, D.; Meyer, J. J.; Rosenthal, S. J.; Sanchez, F.; Jennings, G. K.; Adams, D. E. Detecting and Communicating Material Damage Using Embedded CdSe Nanocrystals. In *CAMX 2015* -

Composites and Advanced Materials Expo; 2015; pp. 611–621.

(58) Brubaker, C. D. C. D.; Frecker, T. M. T. M.; Njoroge, I.; Shane, D. O. D. O.; Smudde, C. M. C. M.; Rosenthal, S. J. S. J.; Jennings, G. K. K.; Adams, D. E. D. E. In-Situ Material State Monitoring Using Embedded CdSe Quantum Dots. *SPIE Proc.* **2016**, *9803*, 980316.

(59) Brubaker, C. D.; Frecker, T. M.; McBride, J. R.; Reid, K. R.; Jennings, G. K.; Rosenthal, S. J.; Adams, D. E. Incorporation of Fluorescent Quantum Dots for 3D Printing and Additive Manufacturing Applications. *J. Mater. Chem. C* **2018**, *6*.

(60) Dukes, A. D.; McBride, J. R.; Rosenthal, S. J.; Dukes III, A. D.; McBride, J. R.; Rosenthal, S. J. Luminescent Quantum Dots. *ECS Trans.* **2011**, *33*, 3–16.

(61) Frecker, T.; Bailey, D.; Arzeta-Ferrer, X.; McBride, J.; Rosenthal, S. J. S. J. Quantum Dots and Their Application in Lighting, Displays, and Biology. *ECS J. Solid State Sci. Technol.* **2016**, *5*, R3019–R3031.

(62) Pu, Y.; Cai, F.; Wang, D.; Wang, J. X.; Chen, J. F. Colloidal Synthesis of Semiconductor Quantum Dots toward Large-Scale Production: A Review. *Ind. Eng. Chem. Res.* **2018**, *57*, 1790–1802.

(63) Zhang, Y.; Xie, C.; Su, H.; Liu, J.; Pickering, S.; Wang, Y.; Yu, W. W.; Wang, J.; Wang, Y.; Hahm, J.; *et al.* Employing Heavy Metal-Free Colloidal Quantum Dots in Solution-Processed White Light-Emitting Diodes. *Nano Lett.* **2011**, *11*, 329–332.

(64) Shen, P.; Li, X.; Cao, F.; Ding, X.; Yang, X. Highly Efficient, All-Solution-Processed, Flexible White Quantum Dot Light-Emitting Diodes. *J. Mater. Chem. C* **2018**, *6*, 9642–9648.

(65) Yang, Y.; Zheng, Y.; Cao, W.; Titov, A.; Hyvonen, J.; Manders, J. R.; Xue, J.; Holloway, P. H.; Qian, L. High-Efficiency Light-Emitting Devices Based on Quantum Dots with Tailored Nanostructures. *Nat. Photonics* **2015**, *9*, 259–265.

(66) Kim, T.-H.; Cho, K.-S.; Lee, E. K.; Lee, S. J.; Chae, J.; Kim, J. W.; Kim, D. H.; Kwon, J.-Y.; Amaratunga, G.; Lee, S. Y.; *et al.* Full-Colour Quantum Dot Displays Fabricated by Transfer Printing. *Nat. Photonics* **2011**, *5*, 176–182.

(67) Dukes, A. D.; Samson, P. C.; Keene, J. D.; Davis, L. M.; Wikswo, J. P.; Rosenthal, S. J. Single-Nanocrystal Spectroscopy of White-Light-Emitting CdSe Nanocrystals. *J. Phys. Chem. A* **2011**, *115*, 4076–4081.

(68) Kambhampati, P.; Mack, T.; Jethi, L. Understanding and Exploiting the Interface of Semiconductor Nanocrystals for Light Emissive Applications. *ACS Photonics* **2017**, *4*, 412–423.

(69) Newton, J. C.; Ramasamy, K.; Mandal, M.; Joshi, G. K.; Kumbhar, A.; Sardar, R. Low-Temperature Synthesis of Magic-Sized Cdse Nanoclusters: Influence of Ligands on Nanocluster Growth and Photophysical Properties. *J. Phys. Chem. C* **2012**, *116*, 4380–

4389.

(70) Dolai, S.; Dutta, P.; Muhoberac, B. B.; Irving, C. D.; Sardar, R. Mechanistic Study of the Formation of Bright White Light-Emitting Ultrasmall CdSe Nanocrystals: Role of Phosphine Free Selenium Precursors. *Chem. Mater.* **2015**, *27*, 1057–1070.

(71) Hines, M. A.; Guyot-Sionnest, P. Synthesis and Characterization of Strongly Luminescing ZnS-Capped CdSe Nanocrystals. *J. Phys. Chem.* **1996**, *100*, 468–471.

(72) Saha, A.; Chellappan, K. V.; Narayan, K. S.; Ghatak, J.; Datta, R.; Viswanatha, R. Near-Unity Quantum Yield in Semiconducting Nanostructures: Structural Understanding Leading to Energy Efficient Applications. *J. Phys. Chem. Lett.* **2013**, *4*, 3544–3549.

(73) Greytak, A. B.; Allen, P. M.; Liu, W.; Zhao, J.; Young, E. R.; Popović, Z.; Walker, B. J.; Nocera, D. G.; Bawendi, M. G. Alternating Layer Addition Approach to CdSe/CdS Core/Shell Quantum Dots with near-Unity Quantum Yield and High on-Time Fractions. *Chem. Sci.* **2012**, *3*, 2028.

(74) Dukes, A. D.; Schreuder, M. A.; Sammons, J. A.; McBride, J. R.; Smith, N. J.; Rosenthal, S. J. Pinned Emission from Ultrasmall Cadmium Selenide Nanocrystals. *J. Chem. Phys.* **2008**, *129*, 1–4.

(75) Underwood, D. F.; Kippeny, T.; Rosenthal, S. J. Ultrafast Carrier Dynamics in CdSe Nanocrystals Determined by Femtosecond Fluorescence Upconversion Spectroscopy. *J. Phys. Chem. B* **2001**, *105*, 436–443.

(76) Pimpang, P.; Sumang, R.; Choopun, S. Effect of Concentration of Citric Acid on Size and Optical Properties of Fluorescence Graphene Quantum Dots Prepared by Tuning Carbonization Degree. *Chiang Mai J. Sci.* **2018**, *45*, 2005–2014.

(77) Gomes, R.; Hassinen, A.; Szczygiel, A.; Zhao, Q.; Vantomme, A.; Martins, J. C.; Hens, Z. Binding of Phosphonic Acids to CdSe Quantum Dots: A Solution NMR Study. *J. Phys. Chem. Lett.* **2011**, *2*, 145–152.

(78) Ning, F.; Cong, W.; Qiu, J.; Wei, J.; Wang, S. Additive Manufacturing of Carbon Fiber Reinforced Thermoplastic Composites Using Fused Deposition Modeling. *Compos. Part B Eng.* **2015**, *80*, 369–378.

(79) Wong, K. V.; Hernandez, A. A Review of Additive Manufacturing. *ISRN Mech. Eng.* **2012**, *2012*, 1–10.

(80) Kruth, J. P. Material Incress Manufacturing by Rapid Prototyping Techniques. *CIRP Ann. - Manuf. Technol.* **1991**, *40*, 603–614.

(81) Calignano, F.; Manfredi, D.; Ambrosio, E. P.; Biamino, S.; Lombardi, M.; Atzeni, E.; Salmi, A.; Minetola, P.; Iuliano, L.; Fino, P. Overview on Additive Manufacturing Technologies. *Proc. IEEE* **2017**, *105*, 593–612.

(82) Horn, T. J.; Harrysson, O. L. A. Overview of Current Additive Manufacturing Technologies and Selected Applications. *Sci. Prog.* **2012**, *95*, 255–282.

(83) Berman, B. 3-D Printing: The New Industrial Revolution 1. A Multi-Faceted Technology: 3-D Printing. *Bus. Horiz.* **2012**, *55*, 155–162.

(84) Leigh, S. J.; Bradley, R. J.; Purssell, C. P.; Billson, D. R.; Hutchins, D. A. A Simple, Low-Cost Conductive Composite Material for 3D Printing of Electronic Sensors. *PLoS One* **2012**, *7*, e49365.

(85) Xun Khoo, Z.; Ee Mei Teoh, J.; Liu, Y.; Kai Chua, C.; Yang, S.; An, J.; Fai Leong, K.; Yee Yeong, W. Virtual and Physical Prototyping 3D Printing of Smart Materials: A Review on Recent Progresses in 4D Printing. **2015**, *103*, 103–122.

(86) Khaled, S. A.; Burley, J. C.; Alexander, M. R.; Roberts, C. J. Desktop 3D Printing of Controlled Release Pharmaceutical Bilayer Tablets. *Int. J. Pharm.* **2014**, *461*, 105–111.

(87) Dudek, P. FDM 3D Printing Technology in Manufacturing Composite Elements. *Arch. Metall. Mater.* **2013**, *58*, 1415–1418.

(88) Lebaron, P. C.; Wang, Z.; Pinnavaia, T. J. Polymer-Layered Silicate Nanocomposites: An Overview. *Appl. Clay Sci.* **1999**, *15*, 11–29.

(89) Kasemann, R.; Schmidt, H. Coating for Mechanical and Chemical Protection Based on Organic-Inorganic Sol-Gel Nanocomposites. *New J. Chem.* **1994**, *18*, 1117–1123.

(90) Beecroft, L. L.; Ober, C. K. Nanocomposite Materials for Optical Applications. *Chem. Mater.* **1997**, *9*.

(91) Weng, Z.; Wang, J.; Senthil, T.; Wu, L. Mechanical and Thermal Properties of ABS/Montmorillonite Nanocomposites for Fused Deposition Modeling 3D Printing. *Mater. Des.* **2016**, *102*, 276–283.

(92) Zhang, D.; Chi, B.; Li, B.; Gao, Z.; Du, Y.; Guo, J.; Wei, J. Fabrication of Highly Conductive Graphene Flexible Circuits by 3D Printing. *Synth. Met.* **2016**, *217*, 79–86.

(93) Zhang, Q.; Zhang, F.; Medarametla, S. P.; Li, H.; Zhou, C.; Lin, D. 3D Printing of Graphene Aerogels. *Small* **2016**, *12*, 1702–1708.

(94) Brubaker, C. D.; Davies, M. A.; McBride, J. R.; Rosenthal, S. J.; Jennings, G. K.; Adams, D. E. Nondestructive Evaluation and Detection of Defects in 3D Printed Materials Using the Optical Properties of Gold Nanoparticles. *ACS Appl. Nano Mater.* **2018**, *1*, 1377–1384.

(95) Skorski, M. R.; Esenther, J. M.; Ahmed, Z.; Miller, A. E.; Hartings, M. R. The Chemical, Mechanical, and Physical Properties of 3D Printed Materials Composed of TiO2-ABS Nanocomposites. *Sci. Technol. Adv. Mater.* **2016**, *17*, 89–97.

(96) Kennedy, Z. C.; Christ, J. F.; Evans, K. A.; Arey, B. W.; Sweet, L. E.; Warner, M. G.; Erikson, R. L.; Barrett, C. A. 3D-Printed Poly(Vinylidene Fluoride)/Carbon Nanotube Composites as a Tunable, Low-Cost Chemical Vapour Sensing Platform. *Nanoscale* **2017**, *9*, 5458–5466.

(97) Brubaker, C. D.; Davies, M. A.; McBride, J. R.; Rosenthal, S. J.; Kane Jennings, G.; Adams, D. E. Nondestructive Evaluation and Detection of Defects in 3D Printed Materials Using the Optical Properties of Gold Nanoparticles. *ACS Appl. Nano Mater.* **2018**.

(98) Danek, M.; Jensen, K. F.; Murray, C. B.; Bawendi, M. G. Synthesis of Luminescent Thin-Film CdSe / ZnSe Quantum Dot Composites Using CdSe Quantum Dots Passivated with an Overlayer of ZnSe. *Chem. Mater.* **1996**, *8*, 173–180.

(99) Harrison, M. A.; Ng, A.; Hmelo, A. B.; Rosenthal, S. J. CdSSe Nanocrystals with Induced Chemical Composition Gradients. *Isr. J. Chem.* **2012**, *52*, 1063–1072.

(100) Rittigstein, P.; Torkelson, J. M. Polymer-Nanoparticle Interfacial Interactions in Polymer Nanocomposites: Confinement Effects on Glass Transition Temperature and Suppression of Physical Aging. *J. Polym. Sci. Part B Polym. Phys.* **2006**, *44*, 2935–2943.

(101) Ash, B. J.; Siegel, R. W.; Schadler, L. S. Glass-Transition Temperature Behavior of Alumina/PMMA Nanocomposites. *J. Polym. Sci. Part B Polym. Phys.* **2004**, *42*, 4371–4383.

(102) Belgacem, M.; Gandini, A. *Monomers, Polymers and Composites from Renewable Resources*; 1st ed.; Elsevier Science: Amsterdam, 2008.

(103) Martin, O.; Avérous, L. Poly(Lactic Acid): Plasticization and Properties of Biodegradable Multiphase Systems. *Polymer (Guildf).* **2001**, *42*, 6209–6219.

(104) Qiao, R.; Deng, H.; Putz, K. W.; Brinson, L. C. Effect of Particle Agglomeration and Interphase on the Glass Transition Temperature of Polymer Nanocomposites. *J. Polym. Sci. Part B Polym. Phys.* **2011**, *49*, 740–748.

(105) Ramanathan, T.; Liu, H.; Brinson, L. C. Functionalized SWNT/Polymer Nanocomposites for Dramatic Property Improvement. *J. Polym. Sci. Part B Polym. Phys.* **2005**, *43*, 2269–2279.

(106) Hamming, L. M.; Qiao, R.; Messersmith, P. B.; Catherine Brinson, L. Effects of Dispersion and Interfacial Modification on the Macroscale Properties of TiO2 Polymer-Matrix Nanocomposites. *Compos. Sci. Technol.* **2009**, *69*, 1880–1886.

(107) Bansal, A.; Yang, H.; Li, C.; Cho, K.; Benicewicz, B. C.; Kumar, S. K.; Schadler, L. S. Quantitative Equivalence between Polymer Nanocomposites and Thin Polymer Films. *Nat. Mater.* **2005**, *4*, 693–698.

(108) Baiardo, M.; Frisoni, G.; Scandola, M.; Rimelen, M.; Lips, D.; Ruffieux, K.; Wintermantel, E. Thermal and Mechanical Properties of Plasticized Poly(L-Lactic Acid).

J. Appl. Polym. Sci. **2003**, *90*, 1731–1738.

(109) Pillin, I.; Montrelay, N.; Grohens, Y. Thermo-Mechanical Characterization of Plasticized PLA: Is the Miscibility the Only Significant Factor? *Polymer (Guildf).* **2006**, *47*, 4676–4682.

(110) Xu, W.; Raychowdhury, S.; Jiang, D. D.; Retsos, H.; Giannelis, E. P. Dramatic Improvements in Toughness in Poly(Lactide-Co-Glycolide) Nanocomposites. *Small* **2008**, *4*, 662–669.

(111) Lee, J. Y.; Su, K. E.; Chan, E. P.; Zhang, Q.; Emrick, T.; Crosby, A. J. Impact of Surface-Modified Nanoparticles on Glass Transition Temperature and Elastic Modulus of Polymer Thin Films. *Macromolecules* **2007**, *40*, 7755–7757.

(112) Boyle, B. M.; French, T. A.; Pearson, R. M.; McCarthy, B. G.; Miyake, G. M. Structural Color for Additive Manufacturing: 3D-Printed Photonic Crystals from Block Copolymers. *ACS Nano* **2017**, *11*, 3052–3058.

(113) Van Derlofske, J. F. Computer Modeling of LED Light Pipe Systems for Uniform Display Illumination. In *Solid State Lighting and Displays*; SPIE, 2001; Vol. 4445, pp. 119–129.

(114) Surez, I.; Gordillo, H.; Abargues, R.; Albert, S.; Martínez-Pastor, J. Photoluminescence Waveguiding in CdSe and CdTe QDs-PMMA Nanocomposite Films. *Nanotechnology* **2011**, *22*, 435202.

(115) Xu, J.; Wang, J.; Mitchell, M.; Mukherjee, P.; Jeffries-El, M.; Petrich, J. W.; Lin, Z. Organic-Inorganic Nanocomposites via Directly Grafting Conjugated Polymers onto Quantum Dots.

(116) Mennitt, P. G.; Shatlock, M. P.; Bartuska, V. J.; Maciel, G. E. 113Cd NMR Studies of Solid Cadmium(II) Complexes. *J. Phys. Chem.* **1981**, *85*, 2087–2091.

(117) Atewologun, A.; Ge, W.; Stiff-Roberts, A. D. Characterization of Colloidal Quantum Dot Ligand Exchange by X-Ray Photoelectron Spectroscopy.

(118) Michael W Allen, T. F. S. M. W. I. U. S. a. Measurement of Fluorescence Quantum Yields. **2010**, 1–4.

(119) Nad, S.; Kumbhakar, M.; Pal, H. Photophysical Properties of Coumarin-152 and Coumarin-481 Dyes: Unusual Behavior in Nonpolar and in Higher Polarity Solvents. **2003**.

(120) Fischer, M.; Georges, J. Fluorescence Quantum Yield of Rhodamine 6G in Ethanol as a Function of Concentration Using Thermal Lens Spectrometry. *Chem. Phys. Lett.* **1996**, *260*, 115–118.

(121) Fairman, H. S.; Brill, M. H.; Hemmendinger, H. How the CIE 1931 Color-Matching Functions Were Derived from Wright-Guild Data. *Color Res. Appl.* **1997**, *22*, 11–23.